

Department of Physics and Astronomy

Ruprecht-Karls-Universität Heidelberg

Master's thesis

in Physics

submitted by

David Gerick

born in Köln

September 2014



**Studies of the non-ionizing radiation hardness and  
temperature dependence of Silicon  
Photomultipliers for the LHCb Tracker Upgrade**

This Master's thesis has been carried out by David Gerick

at the

Physikalisches Institut

under the supervision of

Prof. Dr. Stephanie Hansmann-Menzemer

## **Abstract:**

This thesis presents a study of the temperature dependence and changes due to radiation effects of the performance of Hamamatsu S12571 Silicon Photomultipliers (SiPMs). A setup to control the operation temperature of the photon detectors is designed and is used for the characterization of the detectors mainly by means of dark current and dark count rate. The results from the temperature dependence are in agreement with the stated values from the production company. Both dark current and dark count rate decrease by approximately a factor of 2 for a temperature decrease of  $10^\circ\text{C}$ .

The effects of non-ionizing radiation damage on the SiPMs are studied with two different neutron sources, namely an AmBe source and the TRIGA Mark II reactor in Mainz and a proton beam facility. The neutron sources have been calibrated with reference measurements, exploiting two complimentary techniques. For general comparison, the flux is normalized to the displacement damage of 1 MeV neutrons,  $n_{\text{eq}}$ . The delivered dose of the two neutron sources ranges from  $9.8 \times 10^{10} n_{\text{eq}} \text{ cm}^{-2}$  in the AmBe source to  $1.9 \times 10^{12} n_{\text{eq}} \text{ cm}^{-2}$  in the reactor in Mainz. Therefore, it is exceeding the expected lifetime dose in the LHCb experiment by 50%. One SiPM has been irradiated using a 100 MeV proton beam, with a delivered dose of  $1.75 \times 10^{12} n_{\text{eq}} \text{ cm}^{-2}$ .

The dark current at a given temperature is found to increase linearly with the delivered dose. After radiation, with a dose of  $1.5 \times 10^{11} n_{\text{eq}} \text{ cm}^{-2}$ , the dark count rate at  $-30^\circ\text{C}$  exceeds 40 MHz. Studies of thermal annealing have shown, that it is an effective way to reduce radiation damages in the SiPMs.

## **Kurzfassung:**

In der vorliegenden Arbeit wird die Temperaturabhängigkeit und die strahlungsverschuldeten Veränderungen im Betriebsverhalten von Silizium Photodetektoren untersucht. Zur Temperatursteuerung und zur charakteristischen Vermessung der Detektoren, an Hand von hauptsächlich Dunkelstrom und Dunkelzählrate, wurde ein Messaufbau entwickelt. Die Messungen zur Temperaturabhängigkeit stimmen mit den Werten der Produktionsfirma überein. Bei einer Temperaturreduzierung um  $10^\circ\text{C}$  reduzieren sich der Dunkelstrom und die Dunkelzählrate jeweils um etwa einen Faktor 2.

Mit dem TRIGA Mark II Reaktor in Mainz, einer AmBe Quelle und einem Protonenstrahl wurden die Effekte von Strahlung gemessen. Die Quellen wurden zuvor in Referenzmessungen mit Hilfe zweier komplementärer Techniken kalibriert. Zum Vergleich mit anderen Ergebnissen wird der Fluss auf den verursachten Strahlenschaden von 1 MeV Neutronen,  $n_{\text{eq}}$ , in Silizium normalisiert. Die dabei maximal erreichte Strahlendosis beträgt  $9.8 \times 10^{10} n_{\text{eq}} \text{ cm}^{-2}$  für die AmBe Quelle und  $1.9 \times 10^{12} n_{\text{eq}} \text{ cm}^{-2}$  im Reaktor in Mainz, und ist damit um etwa 50% höher als für die erwartete Lebenszeit der Detektoren im LHCb Experiment. Die 100 MeV-Protonen-Bestrahlung erreicht eine Dosis von  $1.75 \times 10^{12} n_{\text{eq}} \text{ cm}^{-2}$ . Der Dunkelstrom steigt linear mit der erhaltenen Dosis über den gesamten untersuchten Bereich. Die Dunkelzählrate erhöht sich nur bis zu einer Dosis von  $1.5 \times 10^{11} n_{\text{eq}} \text{ cm}^{-2}$  linear und überschreitet bei der maximalen Dosis 40 MHz bei  $-30^\circ\text{C}$ . Das thermische Ausbacken der Detektoren hat sich als sinnvolle Methode zur Reduzierung der Strahlenschäden erwiesen.

# CONTENTS

---

<b>1</b>	<b>Introduction</b>	<b>1</b>
<b>2</b>	<b>The LHCb experiment</b>	<b>3</b>
2.1	Physics at the LHCb experiment . . . . .	3
2.1.1	Physical motivation for the detector upgrade . . . . .	7
2.2	The LHCb detector . . . . .	9
2.3	The Scintillating Fibre Tracker . . . . .	13
<b>3</b>	<b>Silicon Photomultipliers</b>	<b>18</b>
3.1	Introduction into semiconductivity . . . . .	19
3.1.1	Intrinsic semiconductors (type I) . . . . .	22
3.1.2	Doped semiconductors (type II) . . . . .	22
3.1.3	p-n-junction . . . . .	24
3.2	The working principle of SiPMs . . . . .	25
3.3	Parameters of SiPM characterization . . . . .	27
3.3.1	Hamamatsu S12571-050C . . . . .	32
3.4	Radiation damages . . . . .	33
<b>4</b>	<b>SiPM characterization setup</b>	<b>35</b>
4.1	Structures of the setup . . . . .	35
4.2	Electric circuit and devices . . . . .	38
4.2.1	LabView program . . . . .	40
<b>5</b>	<b>Neutron Irradiation</b>	<b>41</b>
5.1	Neutron Activation Analysis . . . . .	42
5.1.1	Production rate . . . . .	43
5.1.2	Activation and decay . . . . .	44
5.1.3	Measurement of the activity . . . . .	45
5.1.4	Photopeak efficiency . . . . .	46
5.1.5	Uncertainty evaluation . . . . .	50
5.1.6	Normalization of the neutron spectrum . . . . .	51
5.2	Dose measurements with PIN-diodes . . . . .	51

5.3	Irradiation facilities . . . . .	53
5.3.1	AmBe source . . . . .	53
5.3.2	Mainz TRIGA reactor . . . . .	56
<b>6</b>	<b>Proton Irradiation</b>	<b>60</b>
6.1	Heidelberger Ionenstrahl-Therapiezentrum . . . . .	61
<b>7</b>	<b>Results</b>	<b>63</b>
7.1	Temperature dependence . . . . .	64
7.2	Radiation effects . . . . .	70
7.2.1	Gain & Breakdown Voltage . . . . .	70
7.2.2	Dark count rate . . . . .	71
7.2.3	Dark current . . . . .	73
7.2.4	Annealing . . . . .	76
<b>8</b>	<b>Conclusion</b>	<b>80</b>
<b>A</b>	<b>Appendix</b>	<b>82</b>
A.1	SiPM irradiation . . . . .	82
A.2	Neutron Measurements . . . . .	83
<b>B</b>	<b>Lists</b>	<b>85</b>
B.1	List of Figures . . . . .	85
B.2	List of Tables . . . . .	86
<b>C</b>	<b>Bibliography</b>	<b>88</b>

# INTRODUCTION

---

The world of elementary particles and fundamental interactions is described by an effective quantum field theory, the Standard Model of particle physics (SM). This theory was developed and extended to the current state over the last decades and has so far withstood all probing by experimental physicists. However, open questions, mainly due to observations such as dark matter in astronomy or neutrino oscillation, cannot be explained by the SM and, therefore, are a strong motivation for the search for new physical phenomena.

The Large Hadron Collider (LHC) at CERN<sup>1</sup> provides the environment to test the SM at the highest energy scales currently available and is devoted to the search for new physics. The experiments at the multi-purpose detectors ATLAS and CMS search for the direct observation of yet undetected particles and have succeeded in 2012 in finding a Higgs-like particle. In a different approach, the LHCb experiment looks for the indirect observation of new particles in loop induced processes of B meson decays.

So far, no deviations from the SM are found at the LHC. To improve the tests of the SM, more precise measurements are required. The precision of most of the measurements performed at the LHCb experiment are dominated by the statistical uncertainties. To reduce them, the LHCb experiment is going to be upgraded during the second long shutdown to significantly increase the recorded luminosity by a factor 5 to  $\mathcal{L} = 2 \times 10^{33} \text{ cm}^{-2} \text{ s}^{-1}$ , by decreasing the bunch spacing from 50 ns to 25 ns and further enhancing the beam focus to increase the number of collisions per event. Under the upgrade conditions, the current Outer Tracker for the tracking of the particles trajectory will not be able to perform properly due to the large number of tracks per event and the required increase of the read-out rate. It will be replaced by the Scintillating Fibre (SciFi) Tracker, which uses 2.5 m long scintillating fibres to track the traversing particles. These fibres will be read-out by Silicon Photomultipliers (SiPMs), which provide the needed granularity for a high spatial resolution and a fast response for the required read-out rate.

The focus of this thesis is on the measurement of the performance of these Silicon Photomultipliers and it is structured as followed. A detailed look onto the LHCb detector and the investigated flavor physics is given in Chapter 2. The functionality and working principle of SiPMs are introduced in Chapter 3. Further, the parame-

---

<sup>1</sup>CERN is the abbreviation for the French name *Conseil Européen pour la Recherche Nucléaire*

ters which are used for a quantitative characterization of the detectors are described. On the background of the research and development process for the new detector, SiPMs are investigated in this thesis concerning their radiation hardness and temperature dependence.

For this purpose, a setup to characterize SiPMs at various temperatures is developed and assembled. The setup is designed to automatically control the SiPMs' temperature over the range from 20 °C down to −35 °C, perform measurements for the SiPM characterization and it is described in Chapter 4.

Using this setup, the performance of Silicon Photomultipliers (SiPMs) undergoing neutron and proton irradiation is investigated and quantified. The flux and spectrum of the two neutron sources, which are used for the irradiation of SiPMs, are calibrated in advance. The used irradiation facilities, the two complimentary calibration methods and the resulting neutron fluxes are presented in Chapter 5.

In Chapter 6 the irradiation of a SiPM at a proton accelerator facility is described. The results of the performance tests of irradiated SiPM and the drawn conclusions are presented in Chapter 7.

# THE LHCb EXPERIMENT

---

The Large Hadron Collider (LHC) at CERN, close to Geneva, is a 26.7 km long circular proton-proton<sup>1</sup> collider [28]. Bunches of protons fly with almost the speed of light in opposite directions through this ring and collide at four positions [28]. With a designed center of mass energy  $\sqrt{s} = 14$  TeV at the collision<sup>2</sup>, physicists at the four main experiments

- ALICE (**A** Large Ion Collider **E**xperiment)
- ATLAS (**A** Toroidal LHC Apparatu**S**)
- CMS (**C**ompact Muon Solenoid)
- LHCb (**L**arge **H**adron Collider **b**eauty)

are extending the frontiers of the experimentally examinable energy regions in particle physics. The collider ring is positioned in a depth of approximately 100 m underneath the Swiss-French border.

The proton (and ion) beams inside the accelerator are held in position and steered by super-conducting magnets. A sketch of the collider including a pre-accelerator ring (SPS) and the four major experiments is shown in Figure 2.1.

The LHCb detector is the smallest detector in size of the four major detectors. Also, the layout of the detector differs generally from the three others since it does not cover the total solid angle around the collision point, as shown in Figure 2.5. LHCb is designed as a single-arm forward spectrometer with an angular coverage of 10 mrad to 250-300 mrad, with the beam pipe lying exactly along the detector's central axis. The sub-detectors and their purpose are described below with a focus on the Tracking stations.

## 2.1 Physics at the LHCb experiment

The scientific agenda of the LHCb experiment is to test the effective quantum field theory which describes the interactions of particles, the *Standard Model of Particle*

---

<sup>1</sup>Also operation with heavy ions such as lead (Pb) is performed

<sup>2</sup>As by the end of Run I in 2012, the maximal reached collision energy is  $\sqrt{s} = 8$  TeV

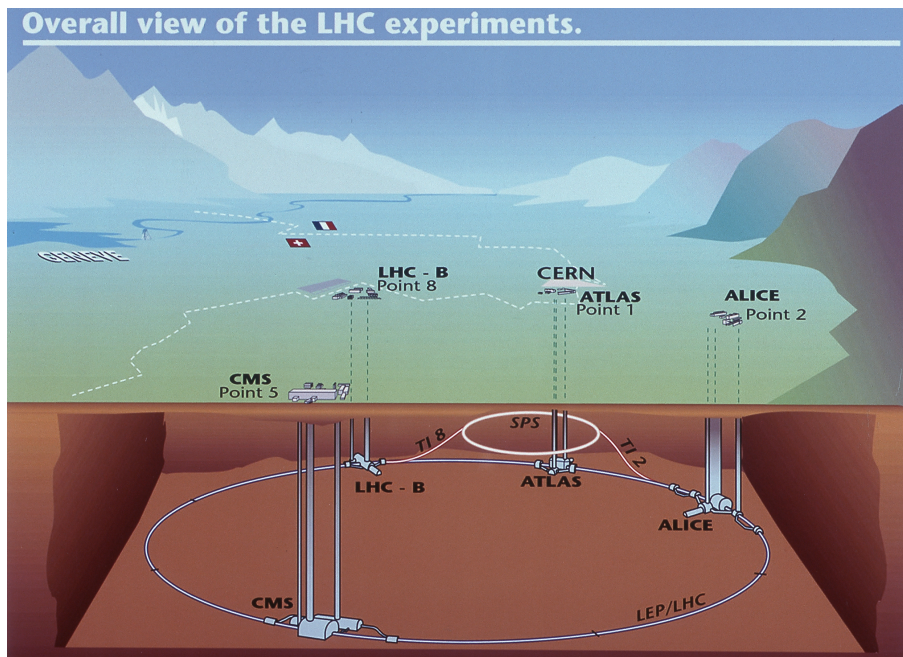


Figure 2.1: Overview of the LHC accelerator ring and the Super Proton Synchrotron (SPS), which pre-accelerates particles for the LHC. The four main detectors and the CERN site are shown [14].

*Physics.* This is achieved by searching for physical phenomena which deviate from the current theory and, therefore, are a hint for new physics beyond this model. A main pillar in the search for new physics is the observation of  $CP$ -symmetry<sup>3</sup> violation ( $CPV$ ) [58]. The  $CP$  violation is a prerequisite for the matter antimatter asymmetry in the universe. However, the currently observed  $CPV$  in the Standard Model is by far not large enough to explain the observed matter antimatter asymmetry. This is a strong motivation for the search of further  $CPV$  processes.

### Standard Model of Particle Physics

The Standard Model (SM) of particle physics is a theory describing fundamental particles and their interactions. It unifies three of the four elementary forces for particle interactions [25, 58].

Namely, the three forces are the electromagnetic force, the weak force and the strong force. An implementation of the fourth force, gravity, has not yet been accomplished within the SM. The electromagnetic and weak interactions are mediated by four force carriers, the spin-1 gauge bosons: photon ( $\gamma$ ), two  $W$ -bosons ( $W^\pm$ ) and the  $Z$ -boson ( $Z^0$ ). The carrier of the strong force are gluons ( $g$ ).

The Standard Model is further comprised of the known twelve spin-1/2 particles, the fermions. Fermions are divided into three generations. Six of these particles

<sup>3</sup>The notation  $CP$  stands for charge ( $C$ ) and parity ( $P$ )

carry color charge of the strong interaction and are called quarks. These quarks are named down (d), up (u), strange (s), charm (c), bottom (b) and top (t)<sup>4</sup>, respectively. Each type of quarks has its flavor quantum number, i.e. b-quarks have bottomness  $B = -1$  or c-quarks have charmness  $C = +1$ .

The other six fermions are leptons, namely the electron ( $e$ ), the muon ( $\mu$ ) and the tau ( $\tau$ ) with their corresponding neutrinos ( $\nu_e, \nu_\mu, \nu_\tau$ ). Each of the twelve particles has its own antiparticle with same mass but reversed charge and reversed quantum numbers.

The SM was developed over most of the second half of the 20th century and has reached a milestone in 2012 in the discovery of a Higgs-like particle by ATLAS [9] and CMS [33]. All these elementary particles are summarized with their masses and spins in Figure 2.2.

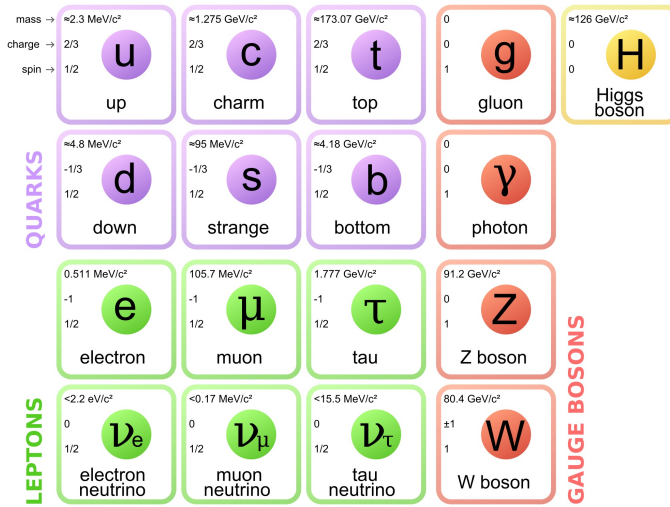


Figure 2.2: The particles known to exist in the Standard Model. The twelve fermions are divided up into the three generations (columns) and into quarks (purple) and leptons (green). The carriers of the interacting forces are the gauge bosons (red). The latest discovery in particle physics is the Higgs boson (yellow) [6]

The quarks introduced in the former paragraph are always found in bound states, the so called hadrons. Two quarks form a meson, three form a baryon and some exotic hadrons with more than three quarks are possible, as for example a tetraquark bound state, which has been observed by LHCb earlier this year [12].

### Search for new physics

The search for new physics beyond the Standard Model at the LHCb is performed using the decay of B- and charm mesons. The meson name indicates its quark

<sup>4</sup>Alternatively the b- and t-quark are referred to as beauty and truth quark

content, i.e. B mesons contain b-quarks. Due to the quark content, each meson has certain flavor quantum numbers, as for example the  $B_s^0$  meson, which contains an anti-b-quark and an s-quark and, therefore, has strangeness  $S = -1$  and bottomness  $B = +1$ .

The neutral decay of a meson with the change of a flavor quantum number is not allowed in 1st order in the SM. This is due to the non-existence of Flavor Changing Neutral Currents (FCNC). The 2nd order decays contain internal loops of virtual particles. The additional coupling constants of these internal loops strongly suppress these decays. Therefore, one refers to *rare decays*, with a branching fraction<sup>5</sup> in the order  $\mathcal{B} = 10^{-6} - 10^{-9}$ . The detection requires a well calibrated detector to reduce the systematical uncertainty and a sufficiently large data sample to reduce the statistical uncertainties.

The reason to select these loop-decays are virtual particles inside the loops. Due to the Uncertainty Principle, particles with off-shell masses are accessible within the short timescale of these loop processes. Their investigation is therefore suitable for the indirect search for new heavy particles. Two examples of loop mediated decays within the SM are shown in Figure 2.4. The rate and the angular distribution of the final state particles of the decay depend on the particles inside the loop process.

In contrary to the approach of this indirect detection, the experiments ATLAS and CMS search for direct observation of new heavy particles by looking at decay particles with a high transverse momentum component. New physics particles with a large mass are less boosted in the lab frame due to the limited total energy at the collision. Thus their decay products are expected to have a large transverse momentum.

The  $b\bar{b}$  quark pair needed to form the desired mesons for the LHCb experiment are mainly produced by the fusion of two gluons<sup>6</sup>. The proton consists of the three valence quarks (two u-quarks and one d-quark) and a sea of spontaneously produced quark pairs and gluons. Gluon fusion can create a joint quark  $q$  only together with its anti-quark  $\bar{q}$ , since flavor quantum numbers are conserved in the strong interaction. Each gluon carries only a portion  $x_i$ , with  $i = 1, 2$  of the total proton's energy. This results in a total available energy  $E$  in the collision of

$$E = x_1 x_2 \sqrt{s} \tag{2.1}$$

If  $x_1$  and  $x_2$  have different values<sup>7</sup>, the final state of the collision is boosted into the direction of the gluon with higher energy. This means, the produced quark pair has a small angle to the beam axis as shown in Figure 2.3. Therefore the detector of the LHCb experiment is shaped in forward direction as mentioned before. The detector is described in detail in the following sections. Before, a physical motivation for an upgrade of the detector is given.

---

<sup>5</sup>The branching fraction is the normalized probability of a decay chain to take place

<sup>6</sup>The cross-section of b-quark pair production at 7 TeV is  $\sigma_{b\bar{b}} = 284 \pm 20 \pm 49 \mu\text{b}$  [10]

<sup>7</sup>The values are very unlikely to have the exact same value due to the broad parton distribution function, which describes the momentum distribution of gluons inside a proton

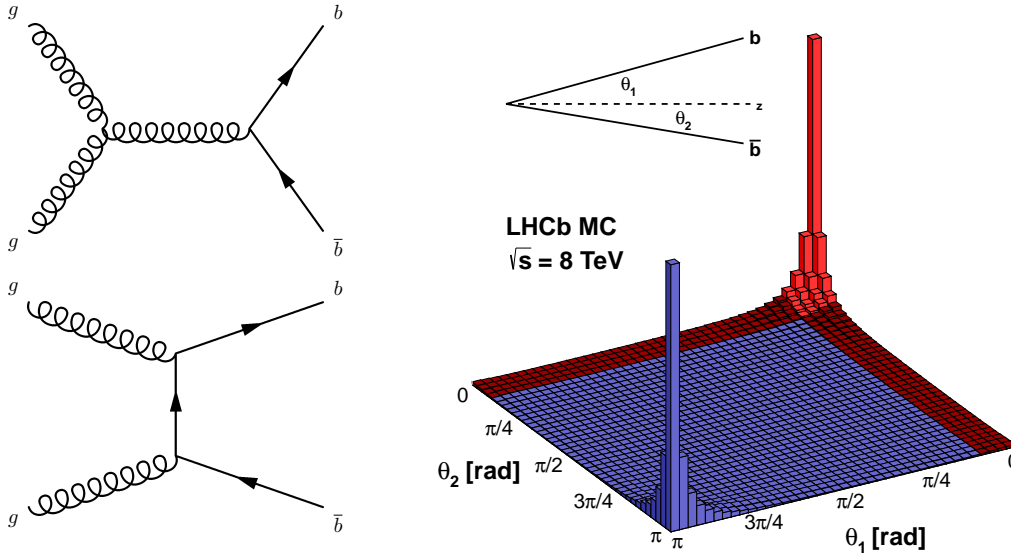


Figure 2.3: Left: Two Feynman diagrams for gluon fusion production of  $b\bar{b}$  quark pairs in the LHCb experiment [4]. Right: The simulated angular distribution of the produced quark pairs for a center of mass energy of 8 TeV. The accumulation of events in the corners is due to the high boost of the final state particles. The angles are given with respect to the beam axis as indicated in the figure. The red colored areas in the figure mark the regions of acceptance of the LHCb detector, whereas the blue region is not covered [52].

### 2.1.1 Physical motivation for the detector upgrade

The primary motivation for an upgrade of the LHCb detector is the increase of signal statistics. Most of the recent results presented by the LHCb collaboration on the search for new physics are limited due to their statistical uncertainties. The search for  $CP$  violation in the decay  $B_s^0 \rightarrow \phi\phi$  and the search for the rare decays  $B_{s/d}^0 \rightarrow \mu^+\mu^-$  are two examples.

#### CP Violation in $B_s^0 \rightarrow \phi\phi$

The decay  $B_s^0 \rightarrow \phi\phi$  is used to measure the  $CP$  violating phase  $\phi_s$ . Other than the phase  $\phi_s$  of the 1st order decay of  $B_s^0 \rightarrow J\Psi\phi$ , the phase in the decay  $B_s^0 \rightarrow \phi\phi$  is expected to be almost zero due to inference effects. Recent results from LHCb were published in [13]:

$$\phi_s = -0.17 \pm 0.15(stat) \pm 0.03(syst) \text{ rad} \quad (2.2)$$

This value is compatible with the SM prediction, which sets an upper limit of  $\phi_s = 0.02$  rad. To further test this prediction, a more precise measurement is needed, which clearly requires a smaller statistical uncertainty. To reach the systematic precision of this measurement, the statistical precision has to increase by a factor five, naively<sup>8</sup> requiring a 25 times larger data sample.

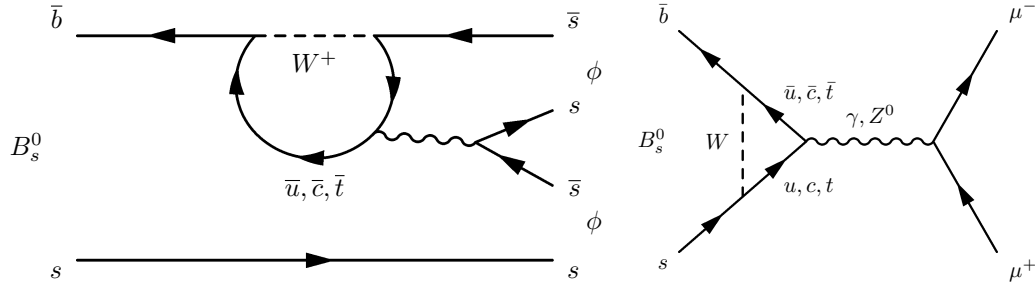


Figure 2.4: The Feynman diagrams for the decay of a  $B_s^0 \rightarrow \phi\phi$  on the left and for the decay  $B_s^0 \rightarrow \mu^+\mu^-$  on the right. The internal loops, which are mentioned in the text are shown, including the particles from the SM, which contribute to the decay [4].

### The rare decay $B_{s/d}^0 \rightarrow \mu^+\mu^-$

The rare decay modes of neutral B-mesons to a di-muon final state are strongly suppressed within the SM and any deviation of its branching fraction from the Standard Model prediction would be a clear hint of new physics [48]. The measurement with current data<sup>9</sup> results in the branching fraction of the  $B_s^0$  decay mode

$$\mathcal{B}(B_s^0 \rightarrow \mu^+\mu^-) = 2.9_{-1.0}^{+1.1}(\text{stat})_{-0.1}^{+0.3}(\text{sys}) \times 10^{-9} \quad (2.3)$$

which is in agreement with the SM predictions of  $3.23 \pm 0.27 \times 10^{-9}$  [29] or  $3.56 \pm 0.18 \times 10^{-9}$  [30]. Further, the measurement sets an upper limit for

$$\mathcal{B}(B_d^0 \rightarrow \mu^+\mu^-) < 7.4 \times 10^{-10} \quad (2.4)$$

at 95% confidence level [11]. The high statistical uncertainty of the first decay mode and the lack of clear evidence of sighting for the latter decay mode require a larger data sample. This is expected to only be possible with an increased data taking rate. But with the current state of operating, data taking beyond an integrated luminosity of  $10 \text{ fb}^{-1}$  is not profitable, as the statistical precision would only increase very slowly [48].

<sup>8</sup>The statistical uncertainty is proportional to the square root of the number of events  $\sigma = \sqrt{N}$

<sup>9</sup>Combined data of Run I with an integrated luminosity of  $3 \text{ fb}^{-1}$

## 2.2 The LHCb detector

The LHCb detector, as it is shown in Figure 2.5, is a single-arm forward spectrometer [16]. It contains different sub-detectors, which measure the energy, the momentum, the velocity and the trajectory of the produced particles. These values are needed for a precise association of the B-meson decay products.

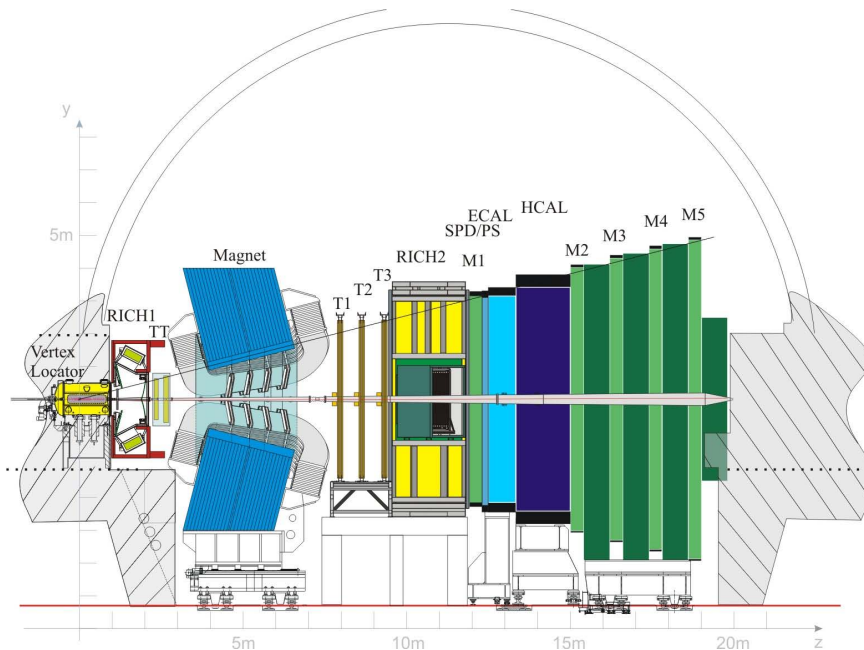


Figure 2.5: Side view of the current LHCb detector. The different sub-detectors are shown, which are introduced in this section. The collision point is on the left side inside the Vertex Locator detector [53]

### Tracking measurement

To reconstruct the momentum of a charged particle, one must reconstruct its flight path through the magnetic field. The first stage of the trajectory measurements is the Vertex Locator [22], positioned closely around the collision point. It consists of silicon strip detectors with a resolution in transverse direction of  $10\ \mu\text{m}$  and in  $z$ -direction<sup>10</sup> of  $40\ \mu\text{m}$  and is designed to reconstruct the primary vertex and the decay vertices [22].

The track reconstruction is performed at four tracking stations, which consists of four detection layers ( $x$ ,  $u$ ,  $v$ ,  $x$ ) each. The two detection layers  $u$  and  $v$  of each station are tilted by  $\pm 5^\circ$  with respect to the  $y$ -direction. The Trigger Tracker (TT)

<sup>10</sup>The right-handed coordinate system adopted has the  $z$  axis along the beam, and the  $y$  axis along the vertical [16].

station is positioned upstream<sup>11</sup> of the magnet and consists of layers of silicon strip detectors with a resolution of 200  $\mu\text{m}$  [16], while the other stations (T1-T3) are positioned down-stream of the magnet. Each station, T1-T3, consist of an Inner Tracker (IT), which is made out of silicon strip detectors, covering the inner region around the beam pipe and the Outer Tracker (OT), which is a gaseous straw tube detector. They form a total of  $3 \times 4$  planes, each of size 5 m  $\times$  6 m, covering the outer regions. It consists of straw tubes with an inner diameter of 4.9 mm, which are filled with a gas mixture. The deposited charge from ionization of passing particles is collected by an anode wire in the central axis of the straw tubes.

In between the TT and the T stations, a magnet with an integrated magnetic field of  $\int Bdl = 4 \text{ T m}$  bends the trajectories of charge particles in the horizontal plane. The particles momentum is determined from the amount of bending [18].

### Particle identification and energy measurements

Particle identification (PID) is performed with the measurements of the two Ring-Imaging Cherenkov (RICH) detectors. Highly energetic charged particles with a velocity greater than the speed of light in the ambient material create Cherenkov light under a characteristic angle [25]

$$\cos(\theta) = \frac{1}{n\beta} \tag{2.5}$$

with the relativistic velocity  $\beta = \frac{v}{c}$  and the index of refraction  $n$  of the used material. As seen in Equation 2.5, the measurement of the angle  $\theta$  of the emitted light can be used to determine the particles velocity. Together with the momentum information from the tracking, the mass of the particles is determined, which is used for particle identification. The two RICH detectors use this feature at different indices of refraction to be sensitive in different momentum ranges to separate pions, protons and kaons [19].

For the separation of photons and electrons, the Scintillating Pad Detector (SPD) in front of the calorimeters uses its insensitivity to photons. The Preshower (PS) detector is similar to the SPD and is positioned just downstream of it behind a 12 mm thick lead sheet. It separates electrons and photons from hadrons, using the fact that hadrons induce only very small showers in the thin lead sheet [42].

The measurement of the particles energy is performed at the downstream part of the detector, where an electromagnetic calorimeter, a hadronic calorimeter and the muon stations are placed. Both calorimeters are “shashlik” sampling calorimeters with absorbing material interleaved with scintillator tiles [17]. In the electromagnetic calorimeter, the absorber is made out of lead, whereas steel absorber are used

---

<sup>11</sup>The definition of orientation within the detector is referred to a stream, with the collision point as its source. Therefore the VeLo is the most upstream detector, while the Muon Stations are sited most downstream.

for the hadronic calorimeter. The absorber decelerates the particles by different processes such as scattering or photo-electric effect, creating particle showers of lighter particles e.g. electrons, photons or pions. These showers are detected by the scintillating material and wavelength shifting fibres (which penetrate the lead/scintillator bulk) in combination with photomultipliers.

The last detectors in the chain are the Muon stations (M1-M5) [21]. They consist of iron absorber material, which, together with the absorber material of the calorimeters, has a total thickness of 20 nuclear interaction-lengths. This thickness is only trespassed by muons due to their minimal ionizing properties. The absorbing material is interleaved by multi-wire proportional counter (MWPC) chambers to detect the muon track.

The first Muon Station (M1) is positioned in front of the calorimeters and is exploited in the first level (L0) hardware trigger for the data acquisition of the detector [21].

### The planned LHCb upgrade

The signal event yield,  $S$ , for a given B decay in the LHCb experiment is given by

$$S = \mathcal{L}_{int} \times \sigma_{b\bar{b}} \times 2 \times f_B \times \mathcal{B}_{vis} \times \epsilon_{tot} \quad (2.6)$$

with the integrated luminosity  $\mathcal{L}_{int}$ , the cross-section for  $b\bar{b}$ -pair production  $\sigma_{b\bar{b}}$ , the hadronization probability  $f_B$  of the corresponding mesons, the branching fraction of decays of interest  $\mathcal{B}_{vis}$  and the total detection efficiency  $\epsilon_{tot}$  [48].

Only two of these parameters leave room for improvements. First is the integrated luminosity,  $\mathcal{L}_{int}$  and second, the trigger efficiency,  $\epsilon_{trigger}$ , which is a part of the total efficiency  $\epsilon_{tot}$ .

With the upgrade [24], the LHCb detector is planned to operate at a luminosity of  $2 \times 10^{33} \text{ cm}^{-2} \text{ s}^{-1}$ , which is half of the maximal luminosity taken by ATLAS and CMS, but about 5 times the peak luminosity of LHCb during Run I [41].

This would lead to an integrated luminosity of about  $50 \text{ fb}^{-1}$  during the designed LHC era, which is an increase by a factor 5 compared to the expected recorded luminosity of  $10 \text{ fb}^{-1}$  by the end of Run II.

Currently, the detector operates with a two stage trigger system, named L0 trigger and High Level Trigger (HLT) [48]. At the stage of the L0 trigger, the read-out rate is limited to 1.1 MHz by the front-end electronics (FEE). To maximize the rate at which interesting events can be read out, sharp cuts on transverse energy of hadrons, electrons and photons are applied to remove uninteresting events and to reduce the rate to 1 MHz. Unfortunately, at higher luminosity these cuts do not only cut away unwanted events, but also events of interest. Already with the luminosity received in 2012, the applied cuts are not sufficient to reduce the event rate to be recorded completely. This difference of delivered luminosity and recorded luminosity is visible in Figure 2.7. Therefore, the hardware trigger level (L0) will be removed and replaced with a fully flexible 40 MHz software trigger. The new trigger configuration increases the expected event yield by an additional factor of up to two

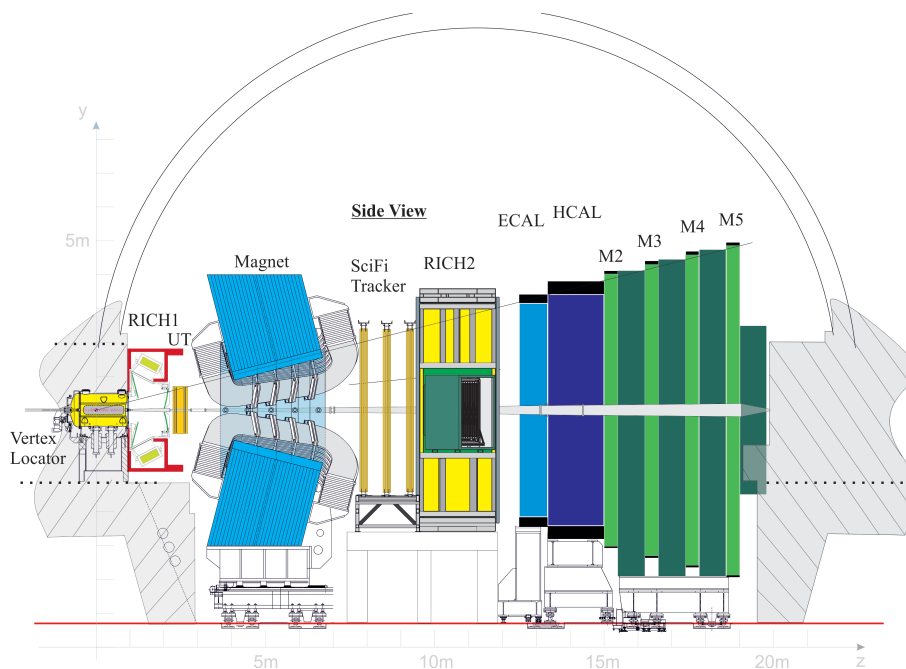


Figure 2.6: Side view of the upgraded LHCb detector. The SciFi tracking detector is positioned between the magnet and RICH2. Further visible changes compared to the current LHCb detector in Figure 2.5 are the Upstream Tracker (UT) between the magnet and RICH1 and the removal of the muon station M1 and the SPD/PS detector [50].

for fully hadronic decays. In total, the expected annual increase of the data samples is a factor 10 and 20 for leptonic and hadronic decays, respectively, compared to the data sample of  $1 \text{ fb}^{-1}$  recorded in 2011. This will result in the same magnifications of 10 and 20 for the total recorded data samples compared to the expected data samples after Run II.

The main requirements to operate at a higher collision rate is new front-end electronics for all subsystems but the muon stations. Further, the Outer Tracker will be challenged by the further increase of the luminosity, as the detector already suffers from occupancies of about 10% at 50 ns bunch spacing at the current luminosity. For a bunch spacing of 25 ns the occupancy at the current luminosity would be  $\mathcal{O}(20\%)$  [20]. So far, this has only little influence on the tracking efficiency. However, the performance of some modules near the beam pipe would dramatically decrease in upgrade running conditions [49]. Therefore the Inner- and Outer Tracker will be replaced by a new detector, the Scintillating Fibre Tracker. As this detector is the main focus of this thesis it will be described in detail in the following section.

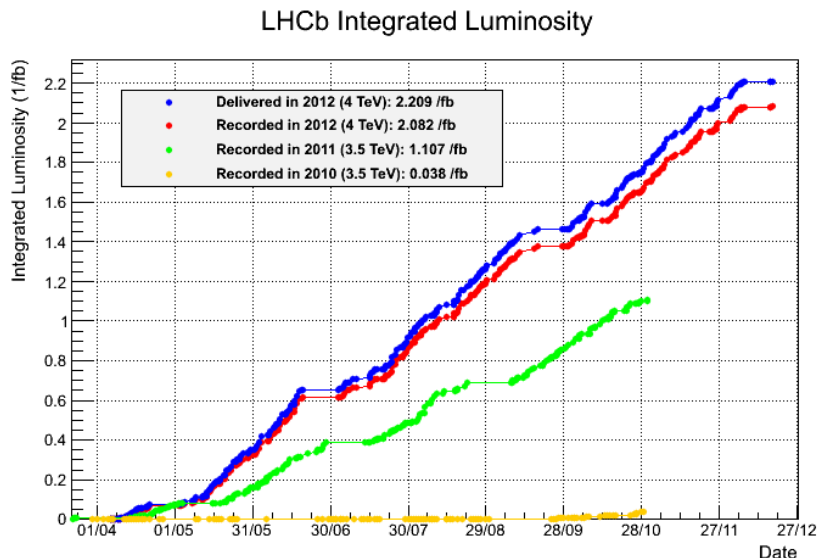


Figure 2.7: The annual recorded luminosity by the LHCb experiment during Run I. The difference between the recorded data (red) and delivered data (blue) in 2012 indicates the loss of events due to the limited readout capacities [51]

## 2.3 The Scintillating Fibre Tracker

The Scintillating Fibre (SciFi) Tracker will be installed during the next long operation pause (LS2) and replace the IT and OT at the tracking stations T1-T3. The technical proposal for the new detector is published in [50], which is summarized in the following. Like the former tracking stations, the new detector will consist of three groups of four layers which are positioned in the x-y-plane as seen in Figure 2.6. The set of four detection planes ( $x, u, v, x$ ) are orientated at  $(0^\circ, 5^\circ, -5^\circ, 0^\circ)$  with respect to the vertical axis, to allow for a two dimensional track reconstruction. One detection layers consist of twelve modules of the approximated size  $52 \text{ cm} \times 500 \text{ cm}$ . A schematic cross section of a module is shown in Figure 2.8.

Each module comprises eight fibre mats of size  $13 \text{ cm} \times 250 \text{ cm}$ . These mats are made of scintillating fibres of diameter  $250 \mu\text{m}$ . The fibres are positioned parallel in longitudinal direction and with high precision<sup>12</sup> inside the mats. Each mat consist of five or six<sup>13</sup> layers of these fibres. The mats will be sandwiched in between two carbon fibre panels to provide stability.

A mirror is placed at the central end ( $y = 0 \text{ cm}$ ) of each fibre mat to increase the light yield of the fibres. At the outer ends ( $y = \pm 250 \text{ cm}$ ) of these modules, SiPM arrays are mounted to detect the photons created by passing particles in the scintillating

<sup>12</sup>The average distance between the center of neighboring fibres is  $275 \mu\text{m}$

<sup>13</sup>The inner modules around the beam pipe will consist of six layers, whereas the outer modules only consist of five layers.

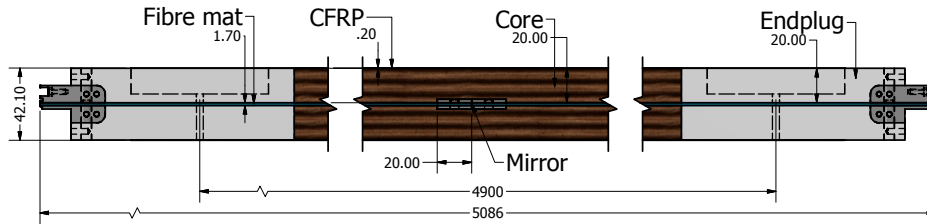


Figure 2.8: Side view of a trimmed SciFi module. The active mat of scintillating fibres is indicated in blue in the center of the module. At both ends the end caps for the mounting of the SiPMs are shown [50].

fibres. The SiPM arrays are put in a light tight end cap as such that they are facing the end face of the fibres. The overlay of the fibre structure and the pixels of the SiPM are shown in Figure 2.9. Four SiPM arrays with 128 channels each are installed over 130 mm of fibre endface. In total, a length of about 150 m is covered with SiPM arrays, resulting in a total number of 590000 channels for the entire fibre tracker. The read-out and digitization of the signals is performed by new FEE in the read-out box (ROB). A cluster algorithm determines the tracked position from the SiPM signals as shown in Figure 2.9.

The SiPMs will be cooled to  $-40\text{ }^{\circ}\text{C}$  to reduce thermally excited noise signals (see Section 3.3 for more details).

## Radiation environment

The collision of hadrons inside the LHCb detector creates a great flux of particles. These particles ionize the detector material. On one hand, this is intended, as the ionization of detector material is used for the detection of the particles, but on the other hand it degrades the functionality of parts of the detector over time. The scintillating fibres will become less transparent over time due to ionizing radiation, decreasing the light yield at the photo-detectors, but are expected to survive over the life of the experiment. The SiPMs are not expected to be damaged by the relatively low ionizing radiation dose of about 60 Gy, but the non-ionizing damage to the silicon by neutrons and other hadrons is quite significant. The major source of high energetic hadrons is backscattering from primary interactions with the calorimeter stations [34]. In the calorimeters, particle showers are created, from which some particles may emerge into the upstream direction towards the tracking stations. The accumulated radiation dose and normalized neutron fluence is simulated using a FLUKA simulation of the LHCb detector [23, 40]. Figure 2.10 shows the x-y-dependence of the fluence distribution. In Figure 2.11, the expected energy spectrum of neutrons for the SiPMs in the SciFi tracker at different positions in y-direction are shown. The SiPMs are positioned outside the inner dense fluence region at  $y = \pm 250\text{ cm}$ .

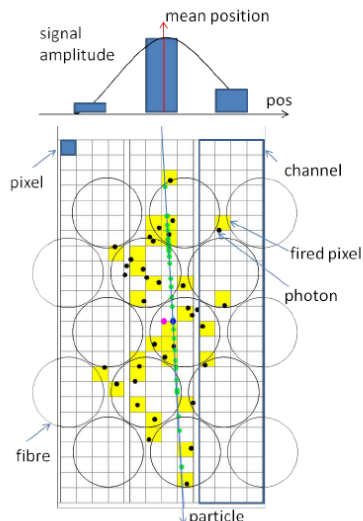


Figure 2.9: View from above onto the end faces of the fibres (larger circles). The scintillation photons are produced inside the fibres at the trajectory of the trespassing particle (green dots) and some photons reach the fibres end faces (black dots), where they trigger pixels of the SiPM array (yellow squares). The amount of fired pixels per channel results in a proportional signal amplitude, indicated by the bar chart at the top. From the mean of this amplitude distribution the position of the trespassing particle is reconstructed [50].

At the designed position of the SiPMs at  $y = \pm 250$  cm the resulting fluence after collecting an integrated luminosity of  $50 \text{ fb}^{-1}$  for the tracking stations T1 and T3 is  $9.5 \times 10^{11} \text{ n}_{\text{eq}} \text{ cm}^{-2}$  and  $13 \times 10^{11} \text{ n}_{\text{eq}} \text{ cm}^{-2}$ , respectively. This radiation dose might be reduced by at least a factor 2 by implementing shielding of borated polyethylene near the SiPMs, as it was shown by the simulations [50].

### SiPM requirements

The SiPMs have to fulfill the following criteria to be operated at upgrade conditions

- High detection efficiency: The scintillation photons created in the fibres have to be detected with an efficiency as high as possible, to ensure a high track reconstruction efficiency.
- Short dead times: The desired collision rate of 40 MHz requires a short dead time of the detector of  $\mathcal{O}(25 \text{ ns})$ .
- High granularity: The high granularity provides a high tracking resolution, prevents an overlap of close by clusters and reduces the relative occupancy of the event.

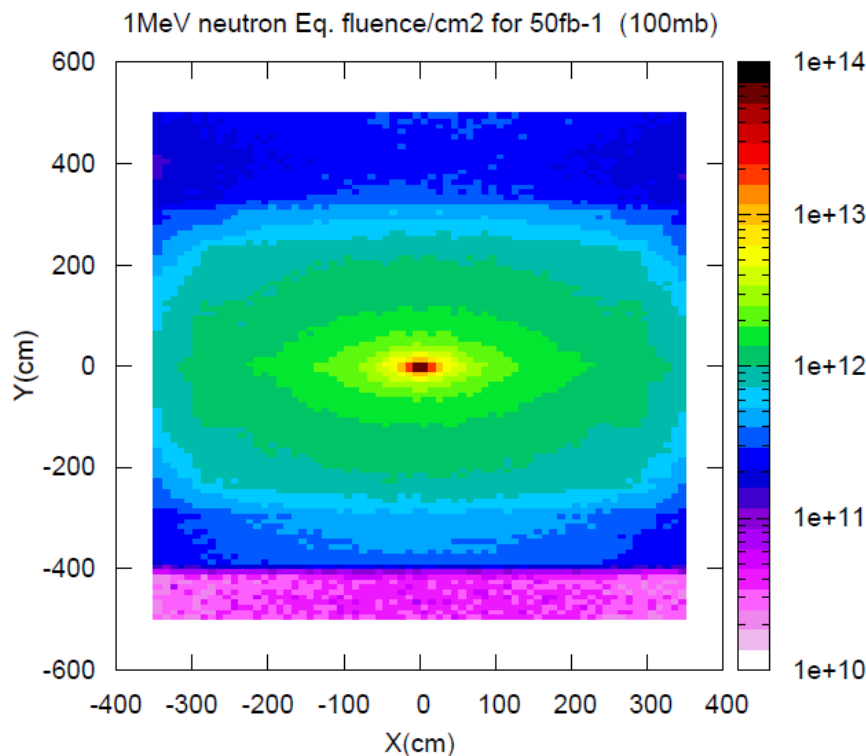


Figure 2.10: Two dimensional plot of the expected accumulated neutron fluence at the tracking station T1 after an integrated luminosity of  $50 \text{ fb}^{-1}$ . The SiPM arrays are positions at  $y = \pm 250 \text{ cm}$  [50].

- Radiation hardness: The degradation by radiation damage has to be kept under control. This means, that the rate of signals caused by other reasons than the light of a trespassing particle must stay significantly below the rate of real signals. Also the shape of the signals must not change significantly to provide stable conditions for the clustering algorithm. Further, the changes in required operation voltage should vary as little as possible.
- Temperature dependency: The temperature stability in the experiment can only be guaranteed up to  $\pm 1^\circ\text{C}$  and therefore the operational parameters should depend only mildly on the temperature.

Two companies are developing potentially suitable SiPMs for the LHCb SciFi tracking upgrade: the German company KETEK<sup>14</sup> and the Japanese company Hamamatsu<sup>15</sup>. In this thesis, the latest type of Hamamatsu detectors, MPPC S12571-050C<sup>16</sup> is investigated and its compatibility with the SciFi conditions is tested.

<sup>14</sup>KETEK GmbH, Hofer Str. 3, 81737 München, Germany

<sup>15</sup>Hamamatsu Photonics K.K., 325-6, Sunayama-cho, Naka-ku, Hamamatsu City, Shizuoka Pref., 430-8587, Japan.

<sup>16</sup>See Subsection 3.3.1 for detailed information about the SiPMs.

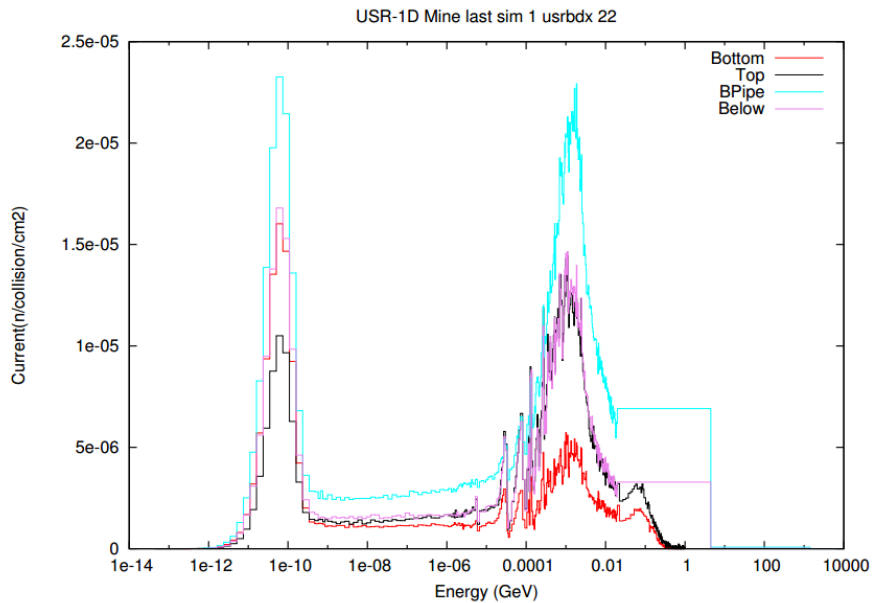


Figure 2.11: The energy spectrum of neutrons from FLUKA simulations at the tracking station T1 for the SciFi modules. The spectral distribution of neutrons is summarized over the energy range from meV up to GeV. The spectrum at the approximated position of the SiPM arrays are indicated in black ( $y = +260$  cm) and purple ( $y = -260$  cm). The cyan colored spectrum is taken near the beam pipe ( $y = +40$  cm) and the red spectrum underneath the detector at  $y = -340$  cm [55].

# SILICON PHOTOMULTIPLIERS

Particle detectors must translate the signature of an incoming particle into an electronic signal, which is then passed into a software based analysis system. Such a signal can consist of photons emitted in a scintillator or of the creation of charge carriers via ionization. In the case of scintillation, a photo-detector is used for the conversion of light to an electronic signal. Traditional and well established photo-detectors are, for example, photomultiplier tubes (PMTs). As shown in Figure 3.1, an incoming photon creates a photoelectron at the cathode (on the left side of the figure) through the photoelectric effect. This electron is accelerated by an applied electric field towards a chain of dynodes. The dynodes have an increasing potential from left to right and the primary electron liberates further electrons from the first dynode material. At every successive dynode, the electron avalanche grows by kicking out more electrons. By reaching the anode at the end of the cascade, the total amount of electrons in the avalanche lies in the order of  $10^5 - 10^7$ , which creates a measurable electric charge. This is then typically measured as a voltage pulse over a resistor. A very strong electric field, and therefore a high applied voltage, between anode and cathode is needed for this high multiplication. The cascade inside the PMTs requires a geometry of at least a few centimeters in length.

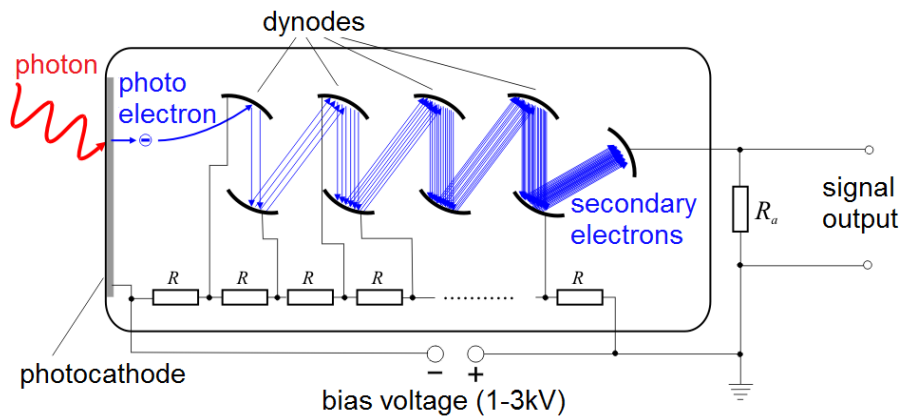


Figure 3.1: Schematic of the working principle of a photomultiplier tube [70] (modified)

A new type of photon detectors are Silicon Photomultipliers (SiPM), based on semi-

conductor technology. SiPMs were first mentioned in 1989 by V. Golovin, et al. (Russian patent #1702881). Ever since, the development has brought up a large variety of different detectors for individual purposes such as high energy physics or medical physics.

Silicon Photomultipliers are pixelated photo-sensitive solid-state detectors with a high granularity. Incoming photons create electron-hole-pairs in the bulk of a pixel, which are accelerated towards the anode and cathode by an electric field. Each pixel consists of a diode, onto which an outer voltage in opposite direction of its internal electric potential is applied. These photo-diodes are assembled in arrays forming multi-pixel photon counters (MPPC). The size of an individual pixel can vary from 10-100  $\mu\text{m}$ . The photo-detector is sensitive to very weak light at the photon-counting level. In Section 3.1, the working principle of the SiPMs is described and the specific parameters to characterize SiPMs are introduced in Section 3.3.

One main advantage of SiPMs over the longer established detectors such as photomultiplier tubes (PMT) is its low operation voltage. Due to the small geometry, the operation voltage can be rather small to create the needed electric field strength. Whereas classic PMTs need an operation voltage of few 1000 V to reach a detectable charge multiplication of the primary electron. Furthermore, the extremely compact geometry leads to a very small distance between anode and cathode, which reduces the drift time of the ionized particles dramatically and makes the SiPM insensitive to magnetic fields. The small pixels allow the usage of SiPMs for a high channel granularity, which with classical PMT is only possible up to a limited granularity in the order of  $\text{cm}^2$ . Each SiPM channel is a group of same number of pixels that allows for a dynamic range of incoming light. All this is reached at comparable internal charge multiplication ( $\mathcal{O}(10^6)$ ) and time resolution ( $\mathcal{O}(100\text{ ps})$ ).

These properties make SiPMs suitable for the read-out of scintillation fibres in the LHCb SciFi Tracker upgrade. Disadvantages are in general the limited range for the detectable photon wavelength<sup>1</sup> and, compared to PMT, the high rate of fake signals induced by thermal excitation inside the silicon at room temperature.

The production companies use different names for SiPMs. Therefore, a Silicon Photomultiplier can also be referred to as SSPM<sup>2</sup>, MPPC or MAPD<sup>3</sup>.

## 3.1 Introduction into semiconductor technology

Solid metallic materials are found in a crystal-like structure which can be described by solid state physics as a three dimensional lattice. For an electron in this periodic potential of atomic nuclei one gets a so called dispersion relation, which is the relation between the wave number of the electron's wave function in the crystal and the energy of the electron. The dispersion relation for electrons in pure silicon is shown in Figure 3.2. Projecting the dispersion relations onto the ordinate, one receives

<sup>1</sup>PMT also have a limited wavelength acceptance due to the photoelectric effect.

<sup>2</sup>Solid-State Photomultiplier

<sup>3</sup>Multi-Avalanche Photon Detector

allowed energy regions, the so called energy bands. Since the atomic potential is different for every nuclide the energy bands differ from one material to another.

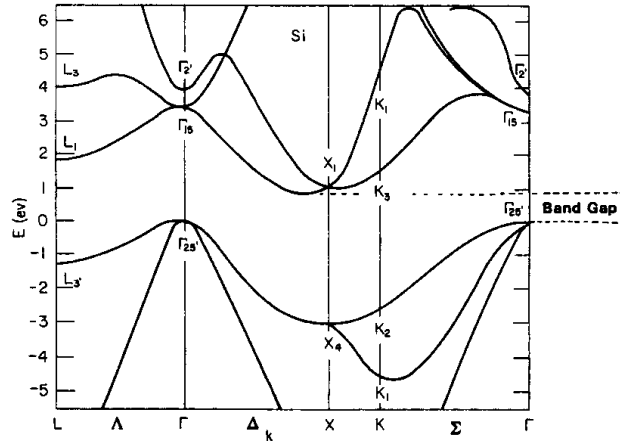


Figure 3.2: Dispersion relation for a pure silicon crystal. The abscissa marks all possible spatial orientation of the propagation directions of an electron's wave function inside the crystal's primitive cell. The different orientations are of no further interest, since the allowed energy bands are created by the projection of the covered energy regions onto the ordinate. The slope of the dispersion curves accounts for the different density of states (Equation 3.2 and 3.3) as well as the effective mass [8].

- **Valence band:** Electrons at this energy level are strongly bound to the atomic nuclei
- **Conduction band:** The binding is weak and electrons are moving almost freely inside the crystal

The difference of three electrically conducting properties arises from the energy gap between the valence band and the conduction band as well as the position of the Fermi energy level,  $E_F$ . The Fermi energy is defined as the energy level up to which all energy states are filled at absolute zero temperature. The energy gap,  $E_g = E_C - E_V$ , is the difference between the upper energy level of the valence band,  $E_V$ , and the lower energy boundary of the conduction band,  $E_C$ . The three different types of electric conductivity are depicted in Figure 3.3 and described below

- An electric insulator has an energy gap of at least a few eV and therefore strongly suppresses the probability of a valence electron to move into the conduction band. This prevents any electrical conduction. The Fermi energy lies in between the valence and the conduction band.
- The other extreme case is the electrical conductor, which has no energy gap. Valence band and conduction band overlap and therefore allow electrons to

move into the higher energy bands. Since the bands overlap, the Fermi energy lies inside a band.

- Semiconductors are somewhere in the middle of these two cases. There is a non-zero energy gap, usually in the order of 1 eV. The Fermi energy lies between valence and conduction band. The gap is small enough for electrons to tunnel into the conduction band by thermal or optical excitation.

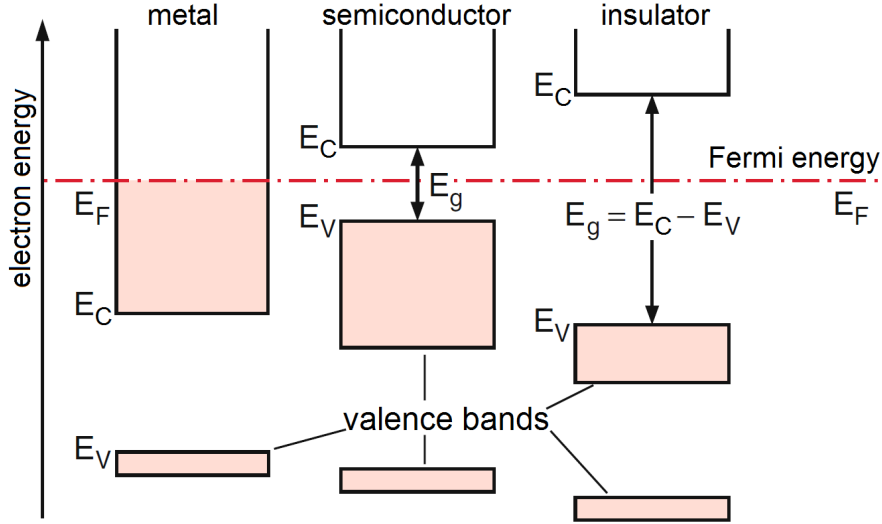


Figure 3.3: Energy bands of metals, semiconductor and insulator [35] (modified).

The bands are filled with charge carriers accordingly to the Fermi-Dirac-distribution

$$f(E) = \frac{1}{\exp\left(\frac{E-E_F}{k_B T}\right) + 1} \approx \exp\left(\frac{-(E - E_F)}{k_B T}\right) \quad (3.1)$$

with the Boltzmann constant,  $k_B$ . The density of states defines the amount of allowed states per energy interval. The more shallow the slope of the dispersion curve, the higher is the density of states  $D_C$  and  $D_V$  for the conduction and valence bands, respectively. For the two bands one gets

$$D_C(E) = \frac{(2m_n^*)^{3/2}}{2\pi^2\hbar^3} \sqrt{E - E_C} \quad E > E_C \quad (3.2)$$

$$D_V(E) = \frac{(2m_p^*)^{3/2}}{2\pi^2\hbar^3} \sqrt{E_V - E} \quad E < E_V \quad (3.3)$$

The effective masses of electrons,  $m_n^*$  and holes,  $m_p^*$  inside the bands is derived from the slope of the dispersion curves

$$m^* = \hbar^2 \cdot \left[ \frac{d^2 E}{dk^2} \right]^{-1} \quad (3.4)$$

with the direction of propagation,  $k$ . The integration over the product of the Fermi-Dirac-distribution and density of states yields the charge carrier density of electrons,  $n$  and holes,  $p$ , in the two bands, where

$$n = 2 \left( \frac{m_n^* k_B T}{2\pi\hbar^2} \right)^{3/2} \exp\left(\frac{-(E_C - E_F)}{k_B T}\right) = N_C \cdot \exp\left(\frac{-(E_C - E_F)}{k_B T}\right) \quad (3.5)$$

$$p = 2 \left( \frac{m_p^* k_B T}{2\pi\hbar^2} \right)^{3/2} \exp\left(\frac{(E_V - E_F)}{k_B T}\right) = N_V \cdot \exp\left(\frac{(E_V - E_F)}{k_B T}\right) \quad (3.6)$$

with Planck's constant  $\hbar^4$  and the effective charge carrier densities  $N_C$  and  $N_V$ .

### 3.1.1 Intrinsic semiconductors (type I)

In extremely pure materials, usually isotopes of *group IV* elements such as carbon (C), silicon (Si) or germanium (Ge), one speaks of intrinsic semiconductors.

For an intrinsic semiconductor, the charge carrier density in the two bands equal

$$n_i = p_i = \sqrt{N_C \cdot N_V} \exp\left(\frac{E_g}{k_B T}\right) \quad (3.7)$$

with index  $i$  indicating *intrinsic*. The Fermi energy level lies in the middle between these two bands.

### 3.1.2 Doped semiconductors (type II)

The other type of semiconductors are doped semiconductors. Here the number of positive and negative charge carriers differs, since impurities are added (*doped*) into the pure crystal. The majority of charge carriers comes from the doping material, the so called *dopant*.

- **n-type semiconductor:** dopant has more electrons in the outer shell than the intrinsic material itself, usually isotopes of *group V* like phosphor (P), arsenic (As) or antimony (Sb). These dopants are also called electron donors.
- **p-type semiconductor:** isotopes mainly of *group III* with an insufficient amount of electrons like aluminum (Al), indium (In) or gallium (Ga). One also speaks of electron acceptors.

The energy boundaries  $E_V$  and  $E_C$  of the semiconductor do not change due to the doping, since the doping concentration typically lies in the order of ppm<sup>5</sup> or ppb<sup>6</sup>. Very high doped materials can reach concentrations up to ‰-levels. But

---

<sup>4</sup>Planck's constant  $h = \hbar \cdot 2\pi$

<sup>5</sup>ppm = parts per million

<sup>6</sup>ppb = parts per billion

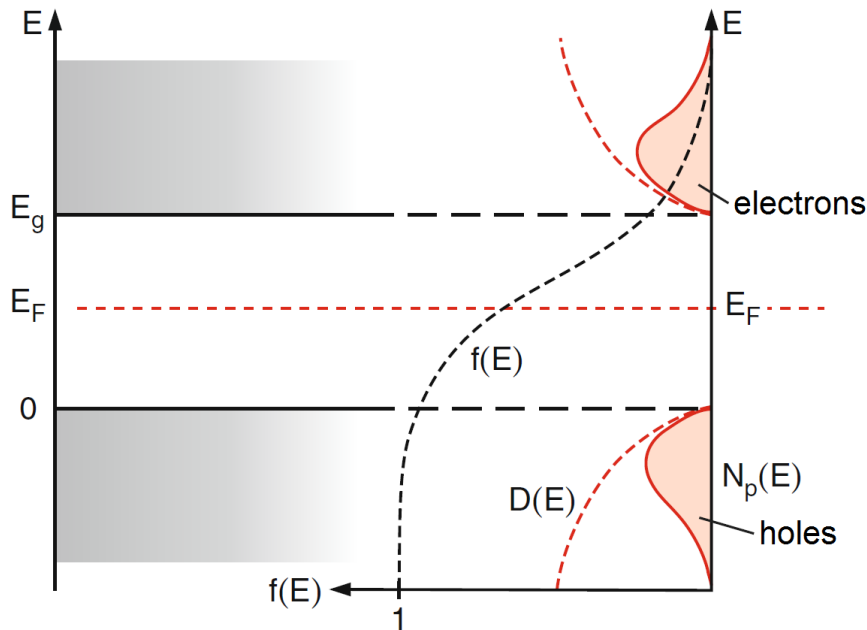


Figure 3.4: Density of states, energy bands and occupation for an intrinsic semiconductor [35] (modified).

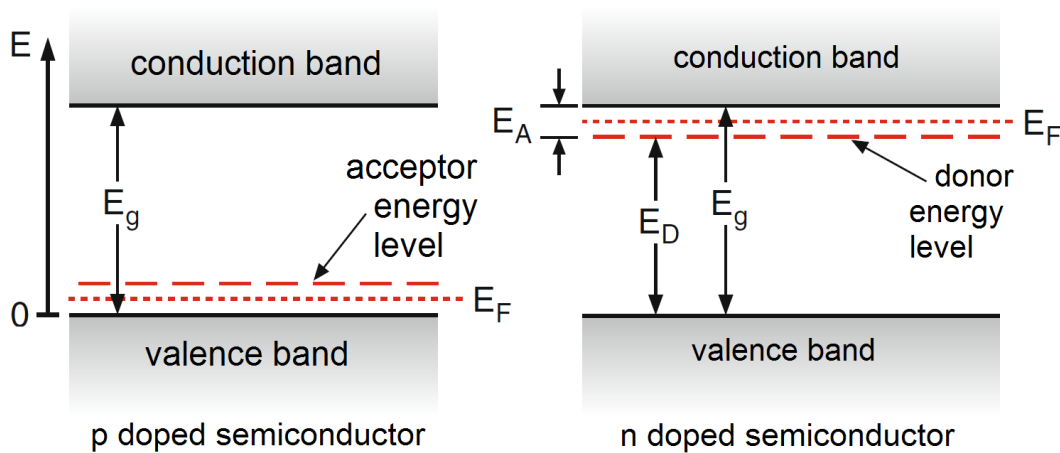


Figure 3.5: Energy levels of p- and n-doped semiconductors on the left and right side, respectively. The added energy levels from the dopant,  $E_A$  and  $E_D$ , are shown. The boundaries of the conduction band and the valence band do not change due to the doping [35] (modified).

dopants are chosen such that the energy level of the dopant's charge carriers are near the corresponding energy band of the intrinsic semiconductor. In other words, the donor's electron energy level is close to the conduction band, whereas the acceptor's energy level for holes is close to the valence band. Boron inside an intrinsic silicon

semiconductor has an energy level of  $E_C - 0.045 \text{ eV}$  below the conduction band, decreasing the energy gap drastically in comparison to the one of pure silicon  $E_g = 1.12 \text{ eV}$ . But since the numbers of the two types of charge carriers now differs due to the doping, the Fermi energy level changes as well. This can be seen in Equation 3.5 and Equation 3.6 and is illustrated in Figure 3.5.

### 3.1.3 p-n-junction

Bringing a p-doped area in contact with an n-doped area creates a so called p-n-junction. In thermal equilibrium, the Fermi energy level equalizes in the two regions, which lowers  $E_V$  and  $E_C$  in the n-part with respect to the p-part of the junction. This is also referred to as band-bending. As a result, free electrons move from the n- to the p-part and holes the opposite direction. Figure 3.6 shows the behavior of the energy levels as well as electrons and holes in a p-n-junction. This creates an electric potential or electric field in the counter direction. The electric field stops the diffusion and an equilibrium state is generated with

$$eU_D = \Delta E_{pot} = E_C^p - E_C^n = E_V^p - E_V^n \quad (3.8)$$

with  $U_D$  the potential difference between n- and p-doped side.

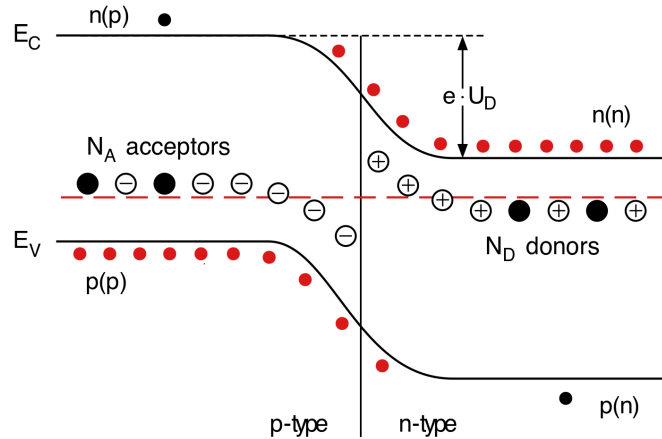


Figure 3.6: Energy levels and charge carrier occupation within a p-n-junction [35] (modified).

At this equilibrium the p-type and n-type side are occupied with a negative and positive charge density, respectively.

This is the simplest form of a diode. Into one direction (*forward bias operation*) the resistance of the p-n-junction is almost negligible whereas in the opposite direction the external field first has to overcome the internal field (*reversed bias operation*). During this voltage region, the diode behaves like a capacitor, being charged by the outer electric field. The small observed current in the reversed region below breakdown voltage is leakage current due to quantum tunneling electrons from valence to conduction band. This is shown in Figure 3.7.

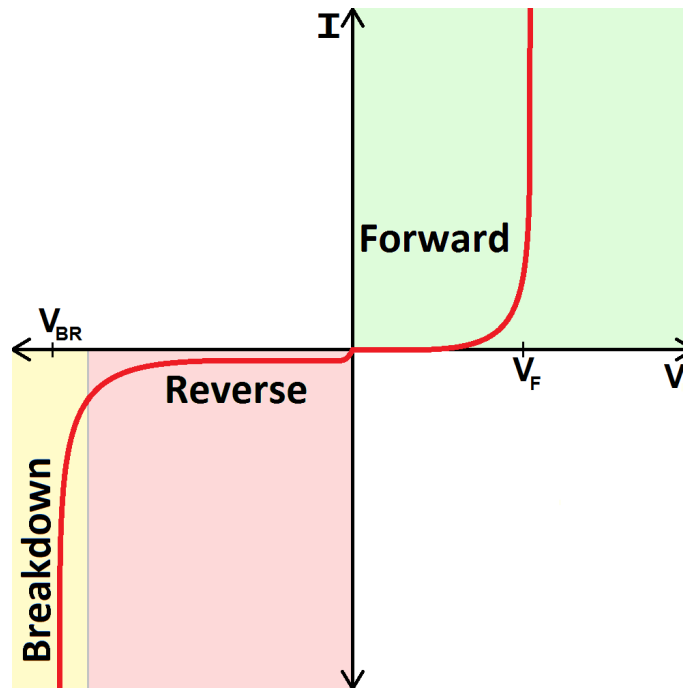


Figure 3.7: A standard curve of the drawn current of a diode. The plot covers both forward and reversed bias operation [3] (modified).

## 3.2 The working principle of SiPMs

Combinations of intrinsic and doped semiconductors are used inside each pixel of a SiPM. SiPMs consist of an intrinsic semi-conductor where incoming photons create electron-hole-pairs by depositing energy. This so called depletion region or drift region is sandwiched by doped areas. The geometry of this region is responsible for the time response of the detector, as larger drift regions require longer drift times. A schematic sketch is shown in Figure 3.9.

For this configuration of intrinsic and doped semiconductors to work as a photon detector, the reverse bias voltage  $V_{BIAS}$  must exceed the internal potential of the p-n-junction,  $U_D$ . The potential wall of the p-n-junction prevents a current flow into the reversed direction and, therefore, the diode is charged comparable to a capacitor. The charge stored in this capacitor is equal to the product of one pixel's capacity and the applied over-voltage. Given these mechanical and electric conditions, an incoming photon may create an electron-hole-pair inside the SiPM by lifting an electron from the valence band to the conduction band. The probability for this is called the quantum efficiency (QE). After creation, the electron-hole-pair is separated by the applied outer electric potential. Electrons are accelerated towards the anode and holes to the cathode of the diode. The strong electric field in a p-n-junction accelerates electrons such that they create an avalanche of electron-hole-pairs in the silicon. The movement of electrons and holes in an avalanche is illustrated in Figure 3.10. The probability for an initial electron-hole-pair to trigger an avalanche

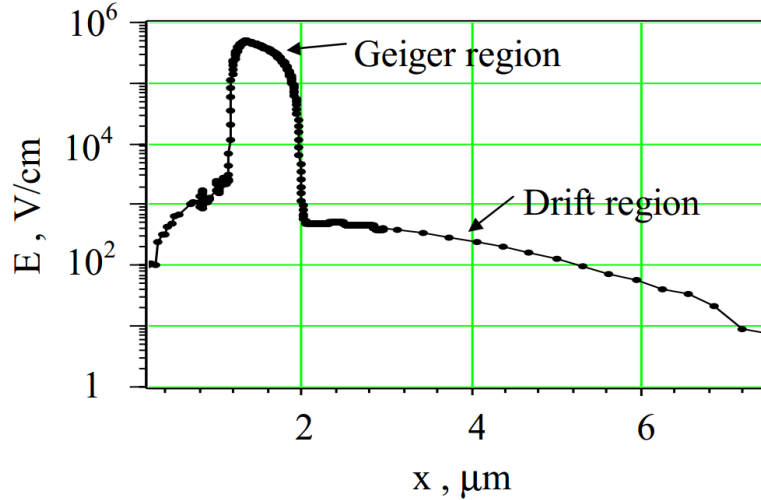


Figure 3.8: The electric field inside a SiPM pixel. The high pedestal is the Geiger region, where the charge multiplication occurs. This high electric field is produced by a p-n-junction. The lower pedestal is the drift region, which consist of an intrinsic semiconductor [31] (modified).

is called Geiger efficiency ( $\epsilon_G$ ) and, if the reversed over-voltage is strong enough to create avalanches, the operation mode is referred to as Geiger mode. Therefore, each pixel is an avalanche photo-diode (APD) operated in Geiger mode (G-APD).

An avalanche is stopped by a resistor in series, which is etched into the silicon as indicated in red in Figure 3.9. As an avalanche is triggered, a current is flowing through the diode and this so called quenching resistor. The voltage drop over the resistor increases due to the increasing current, which is reducing the voltage drop over the diode consequently and thus stopping the avalanche. Due to the quenching, the disposed charge of one avalanche equals the charge stored in one pixel and, therefore, every avalanche discards a discrete amount of charge at same over-voltage. The total charge of such an avalanche is read out as increase of voltage over a resistor, which gives the resulting electric signal of the detector.

A SiPM is assembled by many of these pixels, which are operated in parallel as indicated in the schematic electric circuit in Figure 3.11. The signal amplitude is proportional to the number of fired pixels and the disposed charge consists of integer multiples of the charge of one avalanche. The resulting discrete charge values of different signals are referred to as photoelectron peaks and are used for different measurements, as described in the next section [31, 35, 39, 65, 69].

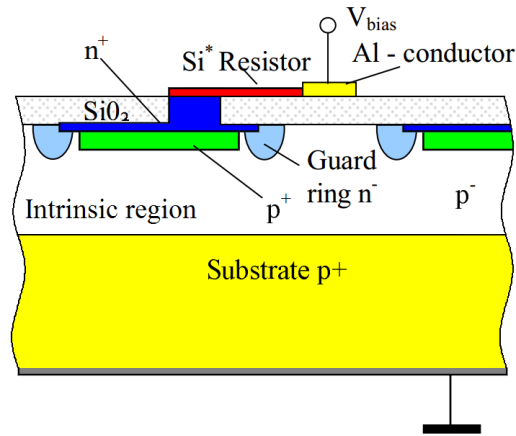


Figure 3.9: Schematic of an assembled SiPM pixel using a NPIP doping-structure and with trenches between the pixels [31] (modified).

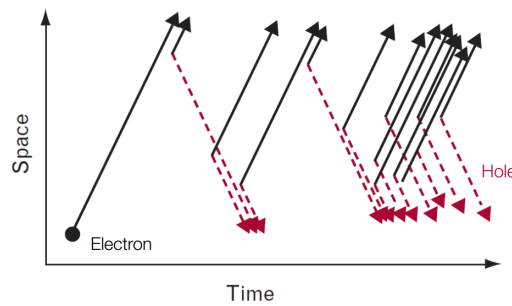


Figure 3.10: Movement of electrons and holes in the avalanche region over time. New electron-hole-pairs are created constantly by both types of charge carriers [65].

### 3.3 Parameters of SiPM characterization

A SiPM is characterized by different parameters, which are used to compare different types of SiPMs with each other. These parameters are introduced and described in the following. Thereby, the focus will be on parameters like dark count rate and dark current, which are determined by using thermally induced signal in the absence of light.

#### Breakdown Voltage

Operating the diode against the orientation of its internal electric field creates a very characteristic current over voltage curve (IV curve). The breakdown voltage ( $V_{BD}$ ) is defined as the bias voltage large enough to create an external electric potential to overcome the internal electric potential of the diode. This is a requirement for the creation of avalanches in the APD. Bias voltages ( $V_{BIAS}$ ) above breakdown voltage

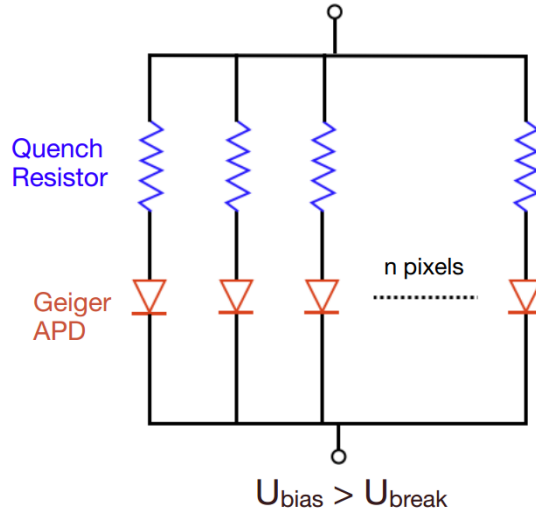


Figure 3.11: A schematic of the electric assembly of a SiPM, including a diode and a quenching resistor for each pixel of the detector [65]

are referred to as over-voltages  $V_{OV}$ :

$$V_{OV} = V_{BIAS} - V_{BD} \quad (3.9)$$

The resulting electric field in the SiPM is proportional to the applied over-voltage.

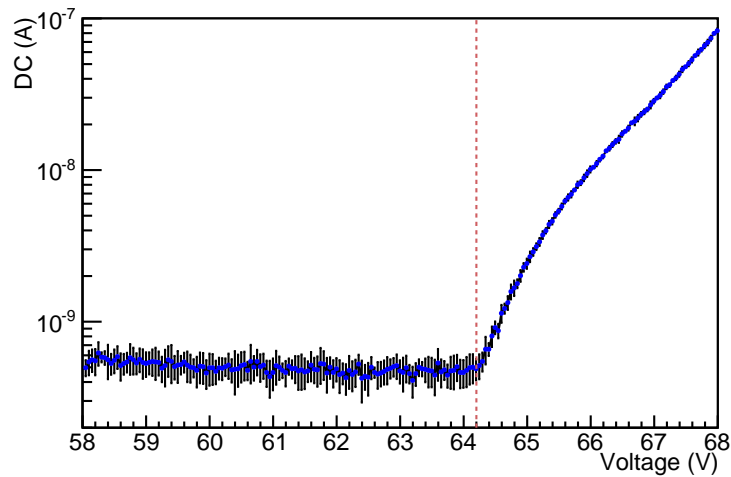


Figure 3.12: Current over voltage curve of an unirradiated SiPM at temperature  $T = 20^\circ\text{C}$ . The dotted line indicates the approximate position of the breakdown voltage

The breakdown voltage dependence on the temperature can be simplified by a linear correlation for the temperature range between 200-300 K for Hamamatsu MPPC [66]

$$V_{BD}(T) \propto \kappa \cdot T \quad (3.10)$$

For the investigated SiPMs, the temperature coefficient is stated by the production company as approximately

$$\kappa = 60 \text{ mV K}^{-1} \quad (3.11)$$

### Gain

The multiplication factor of an elementary charge  $e$  in the avalanche is called the gain of the detector.

$$G = \frac{Q_{\text{avalanche}}}{e} = \frac{V_{OV} \cdot C}{e} \quad (3.12)$$

where  $Q_{\text{avalanche}}$  is the charge of one avalanche. This charge depends linearly on the over-voltage and on the capacity  $C$  of each individual pixel, as explained in Section 3.2. A high gain is desirable to separate signals from electrical noise in the circuit. The temperature dependence is already taken into account in the determination of the breakdown voltage as shown in [60]. Technically, the gain is determined by collecting signals. Since every avalanche creates a discrete signal, gain is determined from the charge difference between a signal with  $n$  pixels firing and a signal with  $n + 1$  pixels firing. With  $n$ , a small integer. The resulting spectrum is shown in Figure 3.13. The difference is equivalent to one avalanche charge  $Q_{\text{avalanche}}$ . A signal with multiple avalanches either comes from crosstalk between the pixels (see below) or from an external light source. Here, the light source provides multiple photons, which fire multiple pixels.

### Dark count rate

Dark count rate (DCR) describes the rate at which the assembly of pixels fires with no incident light on the SiPM. The probability for such an event is a function of temperature [60]:

$$p(T) = CT^{\frac{2}{3}} \cdot \exp\left(-\frac{E_g}{2k_B T}\right) \quad (3.13)$$

with  $C$  a proportionality constant. The dark count rate is determined as the frequency of signals whose voltage amplitude is above half the amplitude of a signal coming from one single pixel. It is therefore referred to as  $DCR_{0.5PE}$ , to separate from dark count rates of signals with larger amplitudes.

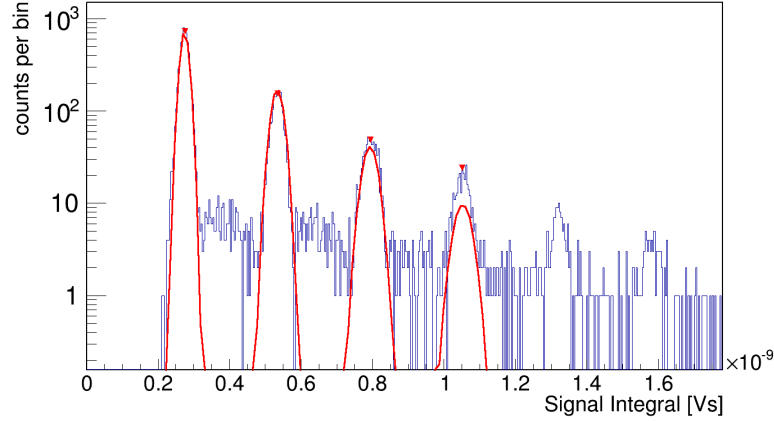


Figure 3.13: Spectrum of the integrated signal amplitude of 5000 signals. The data was taken by a SiPM with no radiation dose at temperature  $T = -35^\circ\text{C}$  and operation voltage of  $V = 63.4\text{ V}$ . The performed simultaneous fit of four Gaussian distributions is shown in red. The distance between all peaks is fixed while the width of the peaks is propagated from the first peak  $\sigma_n = n \cdot \sigma_1$ . The contour of the amplitudes is an exponential curve.

### Dark current

Dark current is the observed current drawn by a SiPM when it sees no light. The current arises from thermally excited electrons and it is the product of the dark count rate, charge per avalanche and average number of avalanches per signal  $\bar{n}$ .

$$DC = DCR \times Q_{avalanche} \times \bar{n} \quad (3.14)$$

where  $\bar{n}$  lies between 1-2 and is the result of crosstalk between the pixels (see next paragraph). The exact average number of avalanches per signal can be determined from the Geometric series

$$\bar{n} = \frac{1}{1 - q}, \quad (3.15)$$

with  $q$  the crosstalk probability. Plots as shown in Figure 3.12 are often referred to as IV curves.

### Crosstalk

As a result of a high electron multiplication inside an avalanche, a huge amount of accelerated charge carriers is moving through the drift regions of the SiPM. Every electron in this avalanche is undergoing acceleration and therefore has a probability to emit synchrotron photons. These photons can emerge from the pixel and trigger a neighboring pixel as it is illustrated in Figure 3.14. The crosstalk probability

lies usually in the order of 20% and may be reduced by physical trenches between the diodes which prevent photons transmission. The geometry and functionality of the implemented trenches is shown on the right side of Figure 3.14. The crosstalk is defined as

$$X_{talk} = \frac{DCR_{1.5PE}}{DCR_{0.5PE}} \quad (3.16)$$

where  $DCR_{1.5PE}$  is the count rate of all signal above background and  $DCR_{0.5PE}$  the count rate of signals firing more than one pixel. Therefore, the DCR at different amplitude thresholds for the trigger is measured. This result is shown in Figure 3.15. The scan through the threshold amplitude creates a characteristic step-like spectrum. The plateau of each step corresponds to the region between two photo peaks, where the DCR rate does not decrease with rising trigger threshold. Since the plateau corresponds to a trigger level in between two neighboring signal amplitudes, it is referred to as  $x.5 PE$ , with integer  $x = 0, 1, 2, \dots$  and the  $.5$  indicating the center between two peaks.

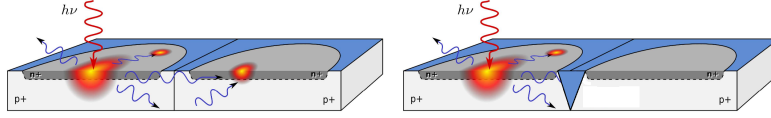


Figure 3.14: Schematic of crosstalk in the SiPM bulk on the left side. The implemented trench to prevent crosstalk is illustrated on the right side [64] (modified).

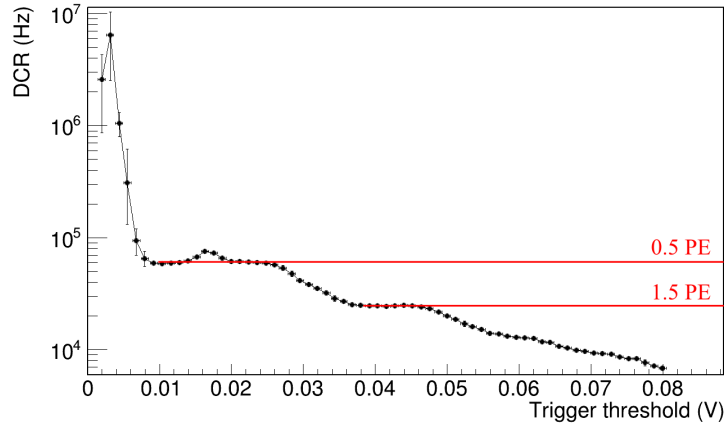


Figure 3.15: Dark count rate spectrum over trigger threshold. The data was taken by a SiPM with no radiation dose at temperature  $T = 20^\circ\text{C}$  and operation voltage of  $V = 67.2\text{ V}$

### Photon detection efficiency

The photon detection efficiency (PDE) is the ratio of the detected photons,  $N_{detected}$  to the total number of incoming photons,  $N_{total}$ .

$$PDE = \frac{N_{detected}}{N_{total}} = QE(\lambda) \times \epsilon_{Geiger}(V, T) \times \epsilon_G \quad (3.17)$$

The PDE is the product of the quantum efficiency (QE), the Geiger efficiency ( $\epsilon_{Geiger}$ ) and the geometry fill factor ( $\epsilon_G$ ). Quantum efficiency is the probability of a photon creating an electron hole pair in the semiconductor. This factor is strongly dependent on the wavelength of the incoming photon. The Geiger efficiency indicates the probability of such an electron hole pair to create a detectable avalanche. It is dependent on the over-voltage and the ambient temperature. Both  $QE$  and  $\epsilon_{Geiger}$  can be designed to be close to unity [66]. The geometry fill factor takes into account that only a part of the surface is sensitive to photons due to trenches, connectors and resistors in the packaging.

The photon detection efficiency for SiPMs lies in the order of 20-50%<sup>7</sup>. The measurement of an absolute PDE value is a complex measurement and is not included in this thesis. A complete measurement of a comparable SiPM was performed by [39].

### Afterpulsing

Impurities in the silicon crystal create energy levels in the forbidden band gap. An impurity could be a damage to the lattice structure or simply an unwanted atomic nuclei. Electrons and holes can be trapped in these impurity centers and once a trapped electron or hole is released after the pixel recovers its charge, it may create a new avalanche identical to the primary avalanche. These fake signals are not distinguishable from the real signals. A study of the time constants of afterpulsing, which are typically in the order of 10-100 ns, is performed in [37].

At the LHCb SciFi upgrade with a read-out every 25 ns, these afterpulses therefore endanger the tracking algorithms. Shorter delays may occur in clusters in the next or second next bunch crossing time window and therefore create correlated fake hits in the tracker.

#### 3.3.1 Hamamatsu S12571-050C

The SiPMs studied in this thesis are produced by Hamamatsu<sup>8</sup>. At Hamamatsu one refers to MPPC instead of SiPM. A different nomenclature is common by the different manufactures for SiPMs. The official naming of the type of MPPC in this thesis is *Hamamatsu S12571-050C*, with the production series *S12571.050* indicating the pixel size of  $50 \mu\text{m} \times 50 \mu\text{m}$  and *C* stands for the ceramic package of the SiPMs. The detectors consist of 400 pixels forming a detector of the size of  $1 \text{mm}^2$ . All

<sup>7</sup>SiPMs with high PDE are for example the KETEK PM3350 series

<sup>8</sup><http://www.hamamatsu.com>

400 pixels are operated and read out by one channel. A picture of one of the used SiPMs is shown in Figure 3.16. The recommended operation voltage is 2.6 V above breakdown voltage. Compared to previous Hamamatsu products, the major improvement of this version is the reduction of afterpulsing.

The total amount of eight SiPMs, which are used within the course of this thesis, are listed in Table A.1.

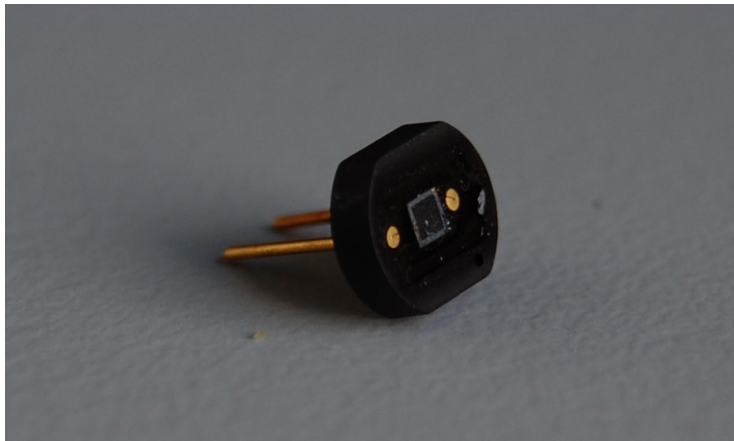


Figure 3.16: Picture of a used SiPM from Hamamatsu

### 3.4 Radiation damages

During the irradiation of Silicon Photomultipliers in a complex radiation environment such as the LHC (Section 2.3), two different processes occur. The first effect is caused by ionization of atoms in the detector material by high energetic particles like electrons or positrons. An electron is released from its bound state inside an atom, leaving a positively charged ion behind. This radiation effect is referred to as *surface damage* and the damage is proportional to the total ionizing dose (TID). The dose is a measure for the deposited energy per mass of the target material and given in units of Gray (Gy).

Studies in [59] with a high activity Cs-137 sources indicate that the small TID has no observable effect on the performance of SiPM.

The second effect for causing radiation damage is the displacement of a Primary Knock on Atom (PKA) in the crystal's lattice [54]. The effect is caused by Non Ionizing Energy Loss (NIEL) of hadrons such as neutrons or higher energetic leptons with a high scattering cross section in the material. The atoms in the lattice are displaced by the recoil energy of the inelastic scattering, which results in the name *displacement damage effect* for this effect. In addition, one often refers to it as *bulk damage*. The displacement generates a so called Frenkel pair [59]. For low PKA energies in the  $\mathcal{O}(25\text{ eV})$  only a point defect in the silicon is created. At recoil energies of above 5 keV, which corresponds to neutron and electron energies of above

35 keV and 8 MeV, respectively, dense clusters of defects are created at the end of a PKA track [59]. The performance of the SiPM is reduced by a growing number of point defects and cluster defects. These defects may work as a trapping center for generated photo electrons, reducing the photon detection efficiency and increasing the afterpulsing probability. If the neutron scatters on a dopant atom, the doping concentration changes which results in a change of breakdown voltage.

The main effect which is investigated in this thesis is the increase of dark count rate and dark current under irradiation. This happens, because the created pair provides energy levels for charge carrier between the valence and conduction band. These further allowed energy levels increase the change for an electron to tunnel from the valence band into the conducting band.

To compare different sources of radiation damage, the radiation damage is normalized to a 1 MeV neutron equivalence. For the radiation tests in this thesis, the 1 MeV equivalence of the different sources is discussed in detail in Subsection 5.1.6.

# SiPM CHARACTERIZATION SETUP

During the course of this thesis a setup to characterize SiPMs is designed and assembled. The studied parameters are breakdown voltage, gain, dark current and dark count rate. The setup is designed to provide automatic temperature regulation of the SiPM during the performed measurements over a range from room temperature ( $\approx 25^\circ\text{C}$ ) down to about  $-37^\circ\text{C}$ .

A LabView program is created to control the temperature, power supplies and read-out devices.

## 4.1 Structures of the setup

The SiPM is placed inside an aluminum case of the size  $127\text{ mm} \times 127\text{ mm} \times 76\text{ mm}$  to protect the electric circuits from interference from external electromagnetic radiation.

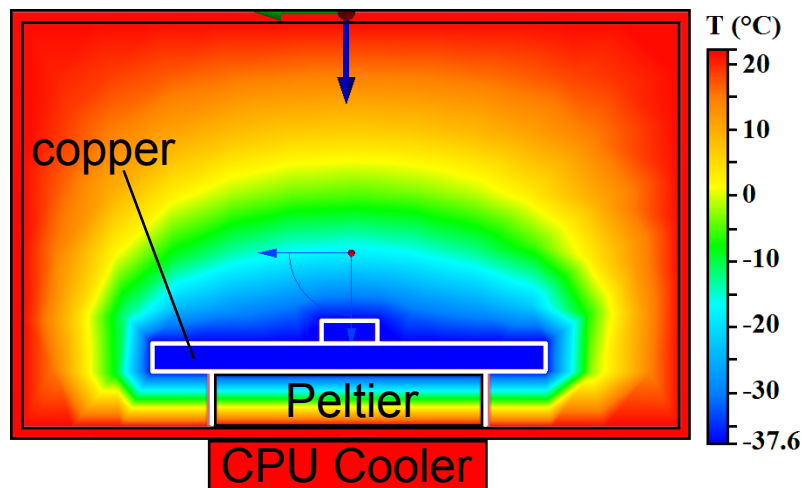


Figure 4.1: A schematic view of the sandwich structure inside the aluminum box. The Peltier element is stacked between the copper plate and the CPU cooler. The thermal simulation was performed using Autodesk Simulation CFD<sup>1</sup>. The simulated temperatures are in good agreement with the experimentally measured values.

A simple CPU water cooler is used as a heat sink for the generated heat output. The water inside the CPU water cooler circuit is cooled by a radiator and fans using air at room temperature. This prevents water condensation on the water hoses and reduces the risk of water spilling onto the electrical equipment. On the inside of the lid sits a three-stage Peltier element, the heart of the cooling process. The Peltier element is introduced below. A 70 mm × 70 mm × 5 mm copper plate is mounted

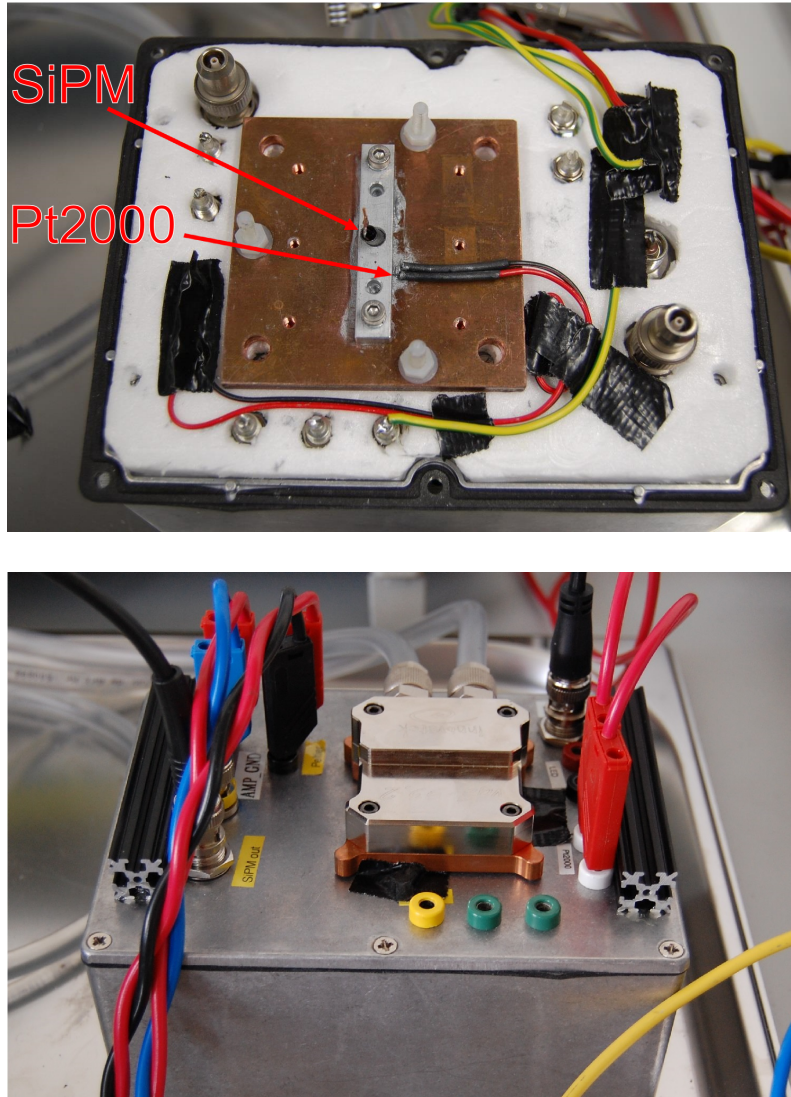


Figure 4.2: Photos of the inside (top) and outside (bottom) of the aluminum box. The Peltier element is not visible. It is positioned underneath the copper plate in the upper picture. The SiPM is mounted by the small aluminum brick, facing down onto the copper plate.

onto the cool side of the Peltier element. It functions as a temperature stabilizer and heat spreader as well as a mechanical base plate for the SiPM mounting. On

this copper plate the SiPM and a Pt2000 temperature sensor<sup>2</sup> are mounted as seen in the upper picture of Figure 4.2. A schematic view of this assembly, including a temperature simulation of the entire box, is shown in Figure 4.1. The resistance to temperature relation of this temperature sensor is

$$R(T) = R_0 \cdot (1 + \alpha T - \beta T^2) \quad (4.1)$$

with  $R_0 = 2000 \Omega$ ,  $\alpha = 3.9083 \times 10^{-3} \text{ K}^{-1}$  and  $\beta = 5.775 \times 10^{-7} \text{ K}^{-2}$  [45]. The SiPM faces the copper block. A slit for light injection is implemented in the setup, but has not been used throughout the measurements. The residual interior is fill with insulating polystyrene to prevent thermal convection and water condensation on any cooled parts inside the box.

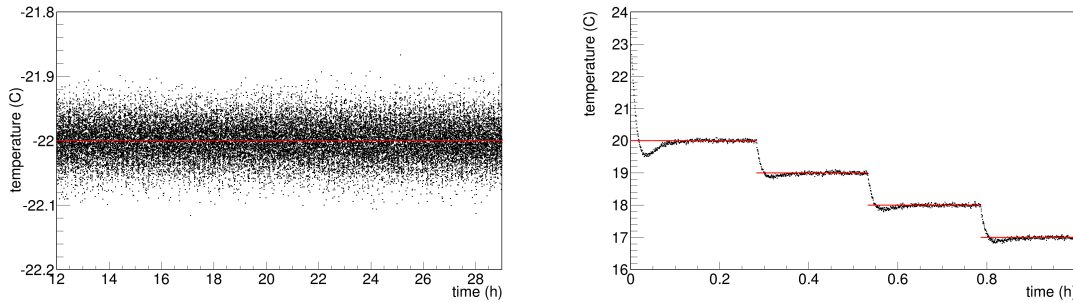


Figure 4.3: Left: The stability of the temperature inside the setup is displayed over a period of many hours. The maximal deviation of the measured temperature (black) from the set temperature (red) hardly exceeds  $0.1^\circ\text{C}$ . Right: The automatic change of set temperature (red) is shown. The actual temperature (black) readjust after the change. A small undershoot is not preventable.

## Peltier element

The Peltier element is a further application of semiconductor technology. The method of thermoelectric cooling makes use of the higher energy level of charge carriers in doped semiconductors compared to the usual electric conductors. An array of small p- and n-doped connections is aligned between two plates such that the current runs in a zig-zag between the hot and the cold side. A few pairs of two doped connectors with the major charge carriers are shown in Figure 4.4.

From the hot to the cold side, the current runs through an n-doped area in which electrons are the major charge carriers going in opposite direction of the current. In the p-doped area, holes are the main charge carrier.

This creates a heat transport from cool to hot side by an electric current, because both types of charge carriers draw energy from the surroundings at the transition

<sup>2</sup>The temperature sensor is produced by *heraeus*. More information are found on the webpage [45].

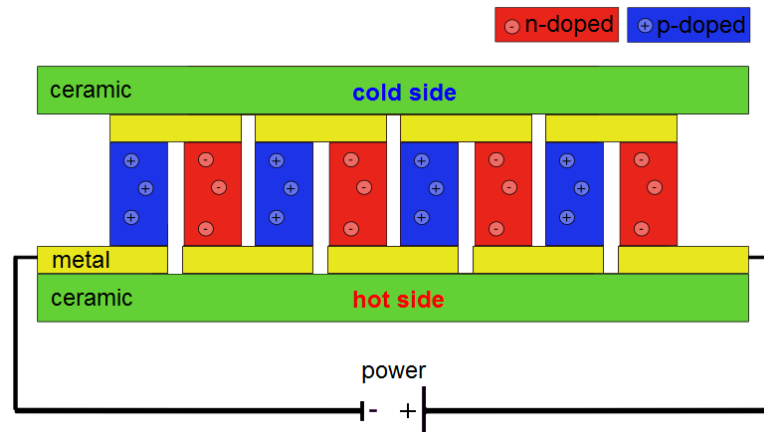


Figure 4.4: Schematic view of an array of pairs of n-doped and p-doped connectors between the hot and cold surface of a Peltier element. The direction of the current is given by the polarity of the power source [68] (modified).

between the doped and the conductive region. This effect is due to the changing energy levels of the charge carriers in the material, as described in Section 3.1. This effect is reversed at the hot side of the Peltier element.

Temperature differences are in the order of  $60\text{ }^{\circ}\text{C}$  for single stage and above  $100\text{ }^{\circ}\text{C}$  for three-stage peltier elements for perfectly insulated elements and no applied heat load.

Under working conditions in the studied setup, a temperature difference  $\Delta T$  of about  $60\text{-}65\text{ }^{\circ}\text{C}$  is reached with a three-stage Peltier element.

## 4.2 Electric circuit and devices

The electric circuit schematic is shown in Figure 4.6. The Pt2000 temperature sensor's resistance is measured by an amperemeter<sup>3</sup> using a 2-wire circuit. The power for the Peltier element comes from a separate power supply unit<sup>4</sup>. A further power supply<sup>5</sup> provides the SiPM power and measures the drawn current. The connections of the electric devices are illustrated in Figure 4.5.

A small PCB board is used to regulate the power supply of the SiPM and its signal read-out. It includes an Low Noise Amplifier<sup>6</sup> with a frequency range of 0.5 to 500 MHz. In order to suppress electric noise in the amplifier circuit, a filter<sup>7</sup> is implemented to prevent noise coupling. To reduce noise on the SiPM bias voltage,

<sup>3</sup>Keithley 6487 Piccoammeter/Voltage Source

<sup>4</sup>HMP4040 by HAMEG Industries, a Rohde & Schwarz company

<sup>5</sup>Keithley 2611B SourceMeter SMU

<sup>6</sup>Plug-In Low Noise Amplifier MAN-1LN by Mini-Circuits

<sup>7</sup>The used noise filter is a Implemented On-Board Type (DC) EMI Suppression Filter BNX002-01 by Murata

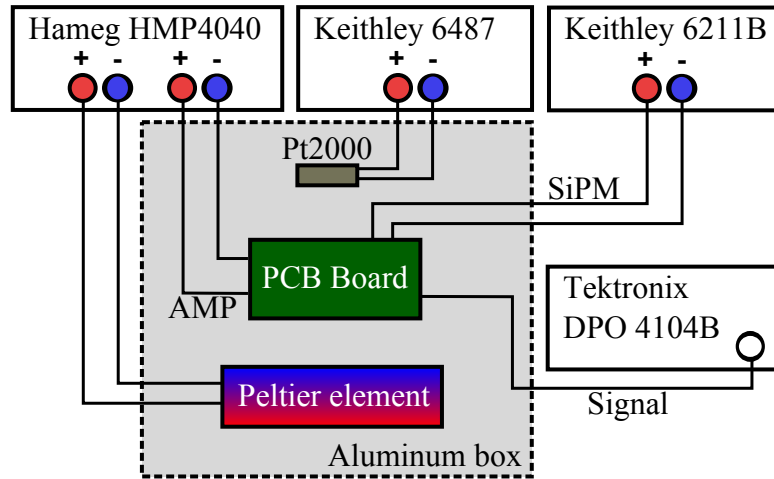


Figure 4.5: The schematic view of the electric circuits of the setup. The SiPM and the amplifier are mounted on the PCB board. See Figure 4.6 for details and connections of the board.

an AC filter ( $R1$  and  $C1$  in Figure 4.6) is coupled in front of the SiPM. At currents in the order of  $1\mu\text{A}$  and above, a significant voltage drops over the resistor  $R1$ , which reduces the operation voltage of the SiPM and has to be taken into account for the calculation of the over-voltage. The charge of an avalanche is measured as the voltage drop over a  $50\Omega$  resistor ( $R2$ ). A capacitor ( $C2$ ) in front of the amplifier removes any DC offset in the signal. The recording of signal waveforms and the measurement of dark count rates is performed by an oscilloscope<sup>8</sup> with 1GHz bandwidth.

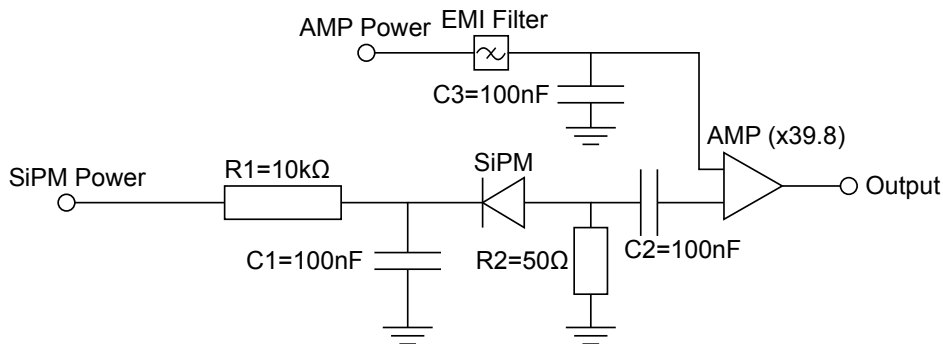


Figure 4.6: The electric circuit layout of the read-out PCB board. See text for details

The resistor  $R1$  in Figure 4.6 is switched in series with the SiPM and, therefore, at high currents of  $\mathcal{O}(\mu\text{A})$  it requires a correction of the operation voltage, which is set by the power supply, due to the voltage drop over this resistor. The resulting

<sup>8</sup>Tektronix DPO 4104B

corrected operation voltage reduce by the current,  $I$  running through the resistor,  $R_1$

$$V_{OV}^{\text{corr}} = V_{OV}^{\text{meas}} - R_1 \cdot I \quad (4.2)$$

### 4.2.1 LabView program

The LabView program's temperature control consists of the read-out of the Pt2000 temperature sensor's resistance and a regulation of the power output for the Peltier element. The required output is derived from a LabView PID tool kit. PID is the abbreviation for proportional-integral-derivative<sup>9</sup>. This PID controller is given a desired setpoint for the temperature of the system. At the same time, the current temperature is measured and fed into the PID controller. The frequency of measuring the temperature and changing the Peltier output is 0.5 Hz. The stability of the temperature control and automatism of change of the desired temperature is shown in Figure 4.3. Once the set temperature is reached with sufficient accuracy<sup>10</sup>, the SiPM measurements are started and run in parallel to the temperature control. The setup is able to perform three types of measurements:

- IV curves for the determination of dark current
- Dark count rate trigger scans to determine dark count rate and crosstalk
- Collecting signal waveforms for gain measurements

After the measurement is finished, the program sets a new temperature and starts off again.

---

<sup>9</sup>In this setup the PID coefficients to weight the corresponding contributions to the PID control are chosen as such:  $P = 0.2$ ,  $I=2.0$  and  $D = 2.0$

<sup>10</sup>For the required accuracy, the mean and standard deviation of the last 100 values of the difference between set and measured temperature both have to be below 0.05 °C

# NEUTRON IRRADIATION

---

In the course of this thesis, SiPMs are irradiated with two different neutron sources to test the behavior of different performance parameters.

- A  $^{241}\text{Am}^9\text{Be}$ -source at the Physikalisches Institut (PI) (see Subsection 5.3.1)
- The TRIGA Mark II neutron fission reactor in Mainz (see Subsection 5.3.2)

For all these sources the neutron flux,  $\Phi$ , was measured and the neutron energy spectrum,  $\phi$ , was investigated. This was done in detail to understand the radiation damage in Silicon Photomultipliers. The method and the results of this investigation are presented in this chapter. The sources used for the irradiation of SiPMs are described in detail in Section 5.3, including the detailed explanation of the irradiation process for the SiPMs at each source. The results of all irradiation measurements with all sources are discussed in Chapter 7.

## Introduction

Neutrons are neutrally charged hadrons, consisting of two d-quarks and one u-quark. They make up the visible matter by forming atomic nuclei together with protons. The free neutron lifetime is [26]

$$T_{1/2} = (880.0 \pm 0.9) \text{ s} \quad (5.1)$$

The direct detection of a neutron is not possible due to the lack of an electric charge. This makes a standard particle detection measurement based on the ionization of the detector material impossible. An indirect measurement is required to determine the neutron flux. The shape of the energy spectrum is more difficult to determine because in indirect measurements information about the neutron's energy are lost. The method used for the measurements of the neutron fluxes for the SiPM irradiation is the so called *Neutron Activation Analysis*, which is explained in details in Section 5.1. In the following paragraphs, the production of neutrons is described. Neutrons with larger energies, which are able to create NIEL radiation damage are described in Section 3.4.

## Production

Free neutrons usually are obtained from fission reactions. In fission of unstable elements like  $^{235}\text{U}$  or  $^{252}\text{Cf}$ , neutrons are emitted directly. Whereas in other cases such as the combination of  $^{241}\text{Am}$  and  $^9\text{Be}$ , the primary emission of the  $^{241}\text{Am}$ -decay is an alpha particle, which then creates a neutron by fusion with  $^9\text{Be}$ . The neutron emission spectrum covers the range of some MeV. The very long lifetime of the neutron allows to moderate these high energy neutrons down to the meV range and use them for experiments, e.g. activation analysis in nuclear chemistry to determine substance concentrations.

Neutrons are formally separated into three groups depending on their energy:

- **Fast neutrons:** Fission neutrons with energies above  $E_{fast} > 100\text{ keV}$ .
- **Thermal neutrons:** Moderated neutrons with energy equal to room temperature  $E_{thermal} = k_B \cdot T \approx 25\text{ meV}$ . A upper boarder is often defined at  $40\text{ meV}$ .
- **Epithermal neutrons:** Neutrons in between the two energy regions:  $40\text{ meV} < E_{epi} < 100\text{ keV}$ .

Fast neutrons are the main source for radiation damage in silicon detectors as described in Section 3.4 and thus the focus is on these high energy neutrons in the following.

## 5.1 Neutron Activation Analysis

For the Neutron Activation Analysis (NAA), small material samples are irradiated by the neutron source. The neutrons create isotopes inside the samples through interactions with nuclei. The concentration of the activated isotopes is measured by collecting the emitted photons from the decaying isotopes. This concentration is proportional to the production rate of the isotopes which is directly correlated to the neutron flux.

Different activation reactions are possible. They differ in their cross-section as well as in the resulting isotopes and side products. The reactions are usually referred to in the following notation



where the isotope on the left side and the right side stand for the sample material and the produced isotope, respectively. Inside the brackets one finds an incoming

neutron (n) and side products of the reaction such as gamma ( $\gamma$ ) or proton (p).

The sample materials are chosen by a couple of criteria

- The cross-section of neutron reactions has to be large enough to be sensitive to the expected neutron spectrum
- The produced isotopes have to be unstable and need a lifetime in the order of minutes or hours
- The decay of the produced isotopes has to have gamma emission
- The number of gamma lines in the decay spectrum should be as small as possible to allow a clear separation and assignment

The different cross-sections further allow to separate fast neutrons from (epi-)thermal neutrons by simply requiring a high neutron energy for the reaction to occur. The threshold energy for  $(n, p)$ - and  $(n, \alpha)$ -reactions often is in the order of MeV. The most used material in this thesis is aluminum, with the reactions shown in Equations 5.2 - 5.4. The geometry and material of each sample is listed in Table A.3. The cross-sections of these reactions is plotted in Figure 5.1 as a function of energy.

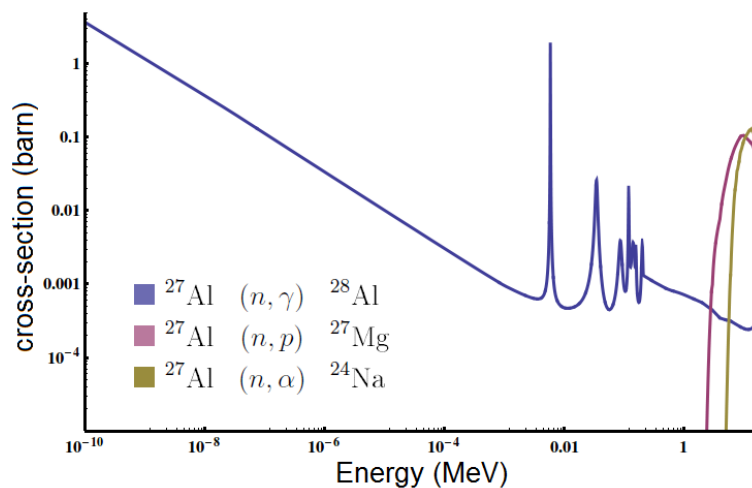


Figure 5.1: The cross-sections for the most common reactions of neutrons in an aluminum bulk. The purple and olive colored lines clearly indicate the existence of a threshold energy for the corresponding reactions.

### 5.1.1 Production rate

The broad energy spectrum requires an integration of the energy dependent cross-section,  $\sigma(E)$ , and the neutron energy distribution,  $\phi(E)$ , over the relevant energy

range. The result is the effective cross-section,  $\sigma_1$ .

$$\sigma_1 = \int_E \phi(E)\sigma(E)dE \quad (5.5)$$

The data of all used cross-section is taken from the neutron database Jendl4.0 [67]. The production rate,  $P$ , of isotopes inside the target is

$$P = N_{target}\Phi_{neutron} \cdot \int_E \phi(E)\sigma(E)dE = N_{target}\Phi_{neutron}\sigma_1 \quad (5.6)$$

with the number of atoms in the target sample,  $N_{target}$ , and the neutron flux,  $\Phi_{neutron}$ .

### 5.1.2 Activation and decay

A material sample exposed to a neutron flux becomes activated with a certain production rate (see section 5.1.1). Therefore, the time dependent change of isotope nuclei numbers in the target is

$$\frac{dN(t)}{dt} = P \quad (5.7)$$

If the produced isotope is unstable, it decays with its characteristic halftime  $T_{1/2}$ . The decay rate is proportional to the number of isotopes

$$\frac{dN(t)}{dt} = -\lambda N(t) \quad (5.8)$$

with the decay constant,  $\lambda = \frac{\ln(2)}{T_{1/2}}$ . In total the change in the number of isotopes is

$$\frac{dN(t)}{dt} = P - \lambda N(t) \quad (5.9)$$

The solution of this differential equation is the number of activated isotopes at time  $t$ . The activation process does not saturate for an activation time,  $t_A < 5 \cdot T_{1/2}$ , such that in this case the number of activated isotopes is

$$N_0(t_A) = \frac{P}{\lambda}(1 - \exp(-\lambda t_A)) \quad (5.10)$$

with the index 0 indicating the final number of isotopes after the irradiation process and therefore the start value for the pure decay process. The trend of  $N_0(t_A)$  during the activation is shown in Figure 5.2 (left). For a long activation time  $t > 5 \cdot T_{1/2}$ , the number of isotope nuclei reaches saturation and the exponential term is negligible

$$N_0(t_A \rightarrow \infty) = \frac{P}{\lambda} \quad (5.11)$$

Inserting the production rate,  $P$ , from Equation 5.6 into Equation 5.10 and solving this equation for the desired neutron flux,  $\Phi_{neutron}$ , results in the following

$$\Phi_{neutron} = \frac{N_0(t_A)\lambda}{N_{target} \cdot \int_E \phi_1(E)\sigma(E)dE} \quad (5.12)$$

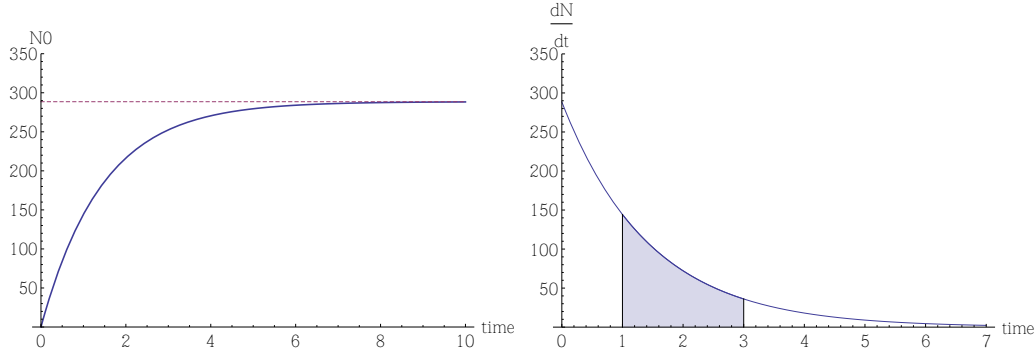


Figure 5.2: Trend of the activation process (left) and illustration of the integration measurement of the exponential decay (right). The time scale in both plots is in units of the  $T_{1/2}$  with the production rate  $P = 200$  per time unit.

### 5.1.3 Measurement of the activity

For the measurement of the neutron flux,  $\Phi$ , the number of activated isotopes after the irradiation,  $N_0$ , is determined by counting the gammas emitted from the isotope decay. The time period between withdrawing the sample from the source and beginning of the measurement is needed to obtain the absolute number of isotope atoms at the end of the activation process. The atoms decay accordingly to the exponential decay law

$$\frac{dN(t)}{dt} = N_0 \exp(-\lambda t) \quad (5.13)$$

and the number of decayed atoms is detected as an time integrated count rate

$$N = \int_{t_s}^{t_e} \lambda N_0 \exp(-\lambda t) dt \quad (5.14)$$

with  $t_s$  and  $t_e$  the start time and end time of the count rate measurement with respect to the end of the activation process. Solving Equation 5.14 for  $N_0$  gives

$$N_0 = \frac{N}{\exp(-\lambda t_s) - \exp(-\lambda t_e)} \quad (5.15)$$

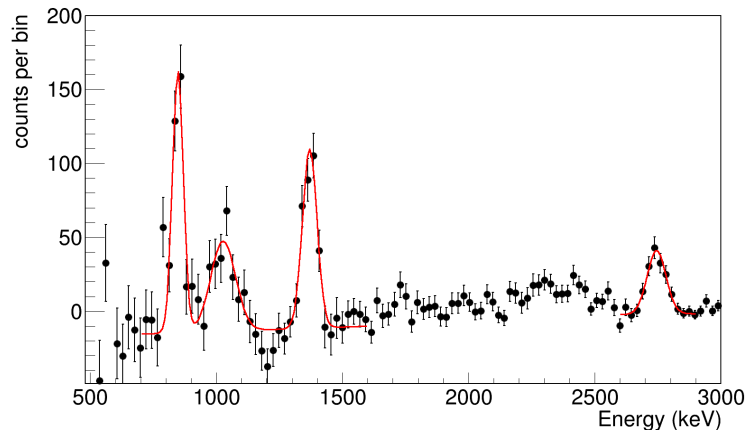


Figure 5.3: The measured decay spectrum of an activated aluminum plate (Lateral 1, see Section A.2). The plate was activated at the surface of the cylinder of source 4117. The two left peaks at 843.8 keV and 1014.4 keV belong to photons emitted by  $^{27}\text{Mg}$ , whereas the other two at 1368.6 keV and 2754.0 keV are from  $^{24}\text{Na}$ . The measurement time is equal to five half-times of  $^{27}\text{Mg}$   $T = 49.3$  min. The occurrence of negative bin contents is due to subtraction of a background spectrum.

A resulting spectrum of a decay measurement is shown in Figure 5.3. From a Gaussian fit and including a linear background subtraction to the photon peaks in the spectrum, the counted number of decaying isotopes  $N$  of the different isotopes is determined.

#### 5.1.4 Photopeak efficiency

An absolute measurement requires an ideal detector with an efficiency to detect a decaying photon,  $\epsilon = 1$ . Since every detectors has a certain efficiency smaller than one, one has to correct for missed counts in the measurement. The integrated count rate has to be corrected for the so called photopeak efficiency.

It is defined as the probability of a photon with energy  $E$  being successfully detected with the *exact* energy  $E$ . The term *exact* is limited by the detector's finite energy resolution, which results in a Gaussian shaped photopeak in the measured energy spectrum. The width of the Gaussian distribution is the energy resolution of the detector. This resolution  $\sigma(E)$  is energy dependent. The photopeak efficiency therefore is the probability to detect a photon of energy  $E$  within a Gaussian distribution with mean  $E$  and  $\sigma(E)$ . It is the result of different factors, which are further introduced in detail below.

The detector does not cover the total sphere of  $4\pi$  around the source, but only a certain solid angle  $\Omega_D$ . Therefore, a geometrical efficiency factor is applied. At

close distance from the detector, the efficiency depends on the photon's angle with respect to the detector orientation. A greater angle results in a shorter pathway through the detector's bulk material. This results in a lower efficiency.

In any case, the incoming photon may only partially deposit its energy. For a photon with energy below 1 MeV Compton scattering is the largest contribution to partial energy deposition. As a result, the photon appears as a photon of lower energy. The detected electron has an energy equivalent to the deposited energy of the scattered photon, which can be derived from the Klein-Nishina-cross section [36]

$$E_{electron} = E_{\nu} \left( 1 - \frac{1}{1 + \frac{E_{\nu}}{m_e} (1 - \cos(\phi))} \right) \quad (5.16)$$

Including the photopeak efficiency  $\epsilon$ , the total neutron flux is

$$\Phi_{neutron} = \frac{N_0(t_A)\lambda}{N_{target} \cdot \int_E \phi_1(E)\sigma(E)dE} \cdot \frac{1}{\epsilon}. \quad (5.17)$$

### Sodium-Iodide detector

For the measurements performed at the Physikalisches Institut, a sodium iodide (NaI) scintillator in combination with a PMT is used. At this detector an additional reduction of efficiency is caused by photo-electrons which scatter on material atoms and are deflected before reaching the PMT. A further reduction is caused by the quantum efficiency of the PMT's cathode. If created and accelerated towards the amplification region, almost all photo electrons entering the cascade of the PMT are detected as a signal. The small fraction of electron avalanche extinction within the photomultiplier tube is negligible.

At energies above twice the electron mass (1.022 MeV) electron positron pair production has an additional effect on the photopeak efficiency. The produced positron annihilates with an electron from ambient material and one or both photons may escape the detector. This results in two additional peaks in the spectrum at energies  $E_1 = E - 511 \text{ keV}$  and  $E_2 = E - 2 \cdot 511 \text{ keV}$  respectively.  $E$  denotes the energy of the photopeak.

The values of the photopeak efficiency have been simulated with the Geant4 [15] Monte Carlo. The correct performance of the Monte Carlo simulation was verified by a measurement with two identical NaI crystals. The coincidence setup is sketched in Figure 5.4 (left).

The isotopes used for the coincidence measurement are  $^{22}\text{Na}$  and  $^{60}\text{Co}$ .  $^{22}\text{Na}$  is a  $\beta^+$  emitter which results in a 511 keV annihilation line. The advantage is the back-to-back orientation of the two annihilation gammas, which is used for the coincidence. The two pulse signals are both cut in energy by a Timing Single Channel Analyser (TSCA) such that only photons with energy in the photopeak range are considered. The background in this region is subtracted offline from sideband interpolation. The isotope has an additional photon line at 1274 keV. The relative fraction between

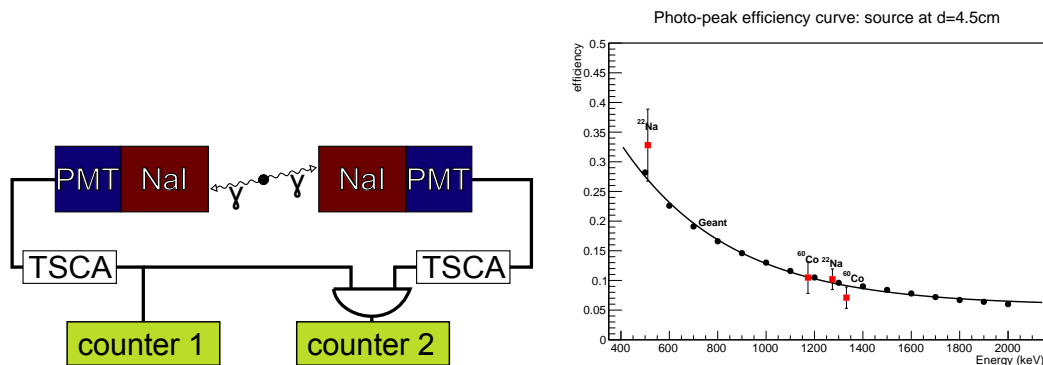


Figure 5.4: Left: The setup to measure photopeak efficiency for a source at distance  $d = 4.5$  cm from the detector. Right: The photopeak efficiency curve including both measured values from the setup on the left in red and the simulated values in black using a pointlike source distance  $d = 4.5$  cm from the detector. The measured and simulated values agree, which verifies the correct simulations with Geant4.

the two decays is  $\frac{N_{511}}{N_{1274}} = 1.799$  and the angular distribution is isotropic.

$^{60}\text{Co}$  emits two photons at 1173 keV and 1332 keV with relative fraction of 1. The angular distribution of the second photon with respect to the primary photon is described in [56] by the formular

$$W(\theta) = 1 + \frac{1}{8}\cos^2(\theta) + \frac{1}{24}\cos^4(\theta) \quad (5.18)$$

The photopeak efficiency then equals the ratio of measured coincidences and single counts on one of the detector, taking geometry, relative fraction, angular distribution and background into account.

$$\epsilon = \frac{N_{coinc}}{N_{single}}, \quad (5.19)$$

with the count rate of counter 1 in Figure 5.4 (left),  $N_{single}$  and the coincidence count rate of counter 2,  $N_{coinc}$ . The uncertainty of the efficiency,  $\epsilon$  propagates from the uncertainty of the coincidence rate  $N_{coinc}$ . Since the number of triggered counts is known, the error for the coincidence rate is given by the binomial distribution

$$\sigma_{coinc} = \sqrt{N_{single} \cdot \epsilon(1 - \epsilon)} \quad (5.20)$$

### Germanium-Lithium detector

The NAA measurements at the neutron reactor in Mainz are performed by a Germanium Lithium (GeLi) semiconductor detector. The cylindrical Germanium crystal is doped with Lithium to create a photon detector. The working principle is similar

to the principle of SiPMs described in Section 3.2 as the doping of the Germanium creates an electric field which separates electrons and holes. One electrode lies in the central axis of the cylinder while the lateral surface is the other electrode. Therefore the electric field has a radial orientation inside the Germanium detector. The main difference is that the GeLi detector does not work in Geiger mode in which the incoming photons create avalanches, but is operated in *Linear mode*. In this mode the collected charge is proportional to the energy of the incoming photon which allows a spectroscopy with a very high resolution (compared the NaI scintillator). More about the exact working principle can be found in common detector physics literature.

The efficiency for this setup is determined using a calibration sample<sup>1</sup> with a volume of 0.5 mL. This sample contains different isotopes. The decay photon lines of their decays cover the energy range of interest. The complete list of included isotopes is found in Section A.2. The concentration and therefore the gamma emission per unit time of the different included isotopes is known with a high precision. From this the efficiency is determined as the ratio of the number of measured photons to the number of expected photons. The resulting efficiency is shown in Figure 5.5.

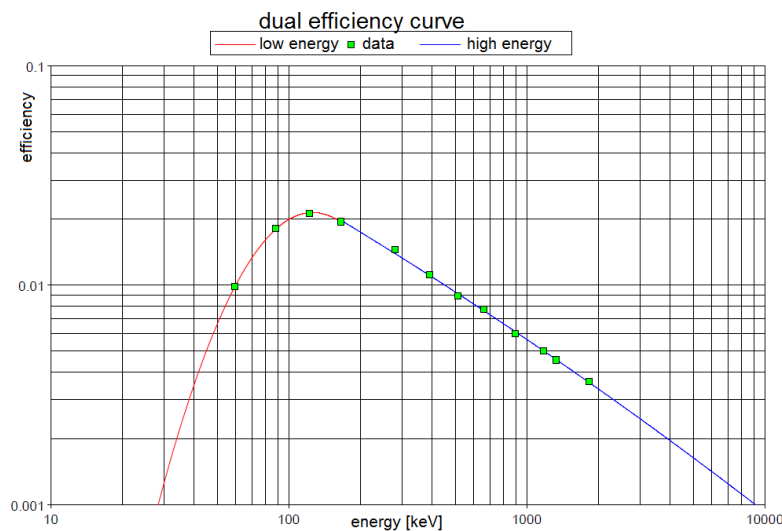


Figure 5.5: The photopeak efficiency curve for the detector 49 at the Mainz TRIGA reactor. The calibration sample is positioned in slot No.4, which is a calibrated position in front of the GeLi detector where most of the NAA samples are positioned during the measurement. For measurements at different slots, the efficiency is determined accordingly.

<sup>1</sup>The used sample is catalog number QCY48 from Eckert & Ziegler Isotope Products

### 5.1.5 Uncertainty evaluation

The uncertainty of the measured neutron fluxes is investigated by taking the statistical and systematical uncertainty from all parameters. The systematic error of the neutron flux in Equation 5.12 is dominated by the product of the cross-section  $\sigma(E)$  with the energy distribution  $\phi(E)$  and the photopeak efficiency  $\epsilon$  of the NaI detector.

The systematic uncertainties of the cross-section are approximated by varying the slope of the initial neutron spectrum (e.g. compare a Maxwellian distribution to a mono energetic spectrum) and by moving the spectrum with respect to the energy. The highest deviation in the resulting effective cross-sections is used for assigning systematic uncertainties. They are listed in Table 5.1.

For the photopeak efficiency the systematic error is dominated by the uncertainty on the geometry of the setup. Slight movements of the source or the activated sample with respect to the detector lead to a significant deviation in the count rate. This is a result of the acceptance of the detector, which varies largely with changes in the solid angle. In addition, the required extrapolation of energy range and geometrical accuracy within the Geant4 simulation requires the application of an uncertainty on the determined efficiency.

If the irradiation is not performed for at least five halftimes, the error on the exact irradiation duration becomes significant. This is the case for the irradiation at the reactor in Mainz (Subsection 5.3.2). The uncertainty of the absolute irradiation duration is estimated to be 10%. The statistical uncertainty of the measurement is derived from the count rate of the decaying isotopes.

$$\sigma_{stat} = \sqrt{N} \quad (5.21)$$

The corresponding values for the systematical uncertainties are listed in Table 5.1. The statistical uncertainties are stated together with the resulting fluxes at the according Subsections in Section 5.3.

<b>Systematic uncertainties</b>	
Cross-section	8.0% (AmBe)
	9.4% (Mainz)
Photopeak efficiency	20.0% (AmBe)
	5.0% (Mainz)
Irradiation duration	10.0% (Mainz)
total (sys)	21.5% (AmBe)
	14.6% (Mainz)

Table 5.1: Sources of systematic uncertainties for the neutron flux determination.

### 5.1.6 Normalization of the neutron spectrum

A determined neutron spectrum is normalized to 1 MeV neutron equivalence. This is done by introducing a hardness factor  $\kappa$  for a neutron spectrum  $\phi(E)$ . This hardness factor converts the potential radiation damage of a neutron with the energy spectrum  $\phi(E)$  such, that it corresponds to the damage of a mono energetic 1 MeV neutron [63]. In this way, irradiation at different neutron sources is comparable. If further referring to the 1 MeV neutron equivalence, the index *eq* is used. As well the conversion of the displacement damage due to proton irradiation is convertible as shown in Chapter 6. For the determination of the hardness factor, the neutron's displacement function,  $D(E)$  is folded with the spectrum and afterwards normalized.

$$\kappa = \frac{\int D(E) \cdot \phi(E) dE}{D(1 \text{ MeV}) \cdot \int \phi(E) dE} \quad (5.22)$$

with the normalization of the 1 MeV displacement damage  $D(1 \text{ MeV}) = 95 \text{ MeV mb}$  [63]. The equivalent neutron flux is then calculated by

$$\Phi_{eq} = \kappa \int \Phi(E) dE \quad (5.23)$$

with the neutron flux  $\Phi(E)$ . The normalized displacement function for silicon is shown in Figure 5.6.

Source	Hardness factor $\kappa$
AmBe-source	1.443
TRIGA Mark II in Mainz	1.048
100.46 MeV protons <sup>2</sup>	1.285

Table 5.2: Determined hardness factors for the two investigated neutron sources and in addition the hardness factor for 100.46 MeV protons as they are used for irradiation (see Section 6.1). Due to the general uncertainty of neutron spectroscopy, an error in the order 10-20% has to be applied to all values.

## 5.2 Dose measurements with PIN-diodes

A cross-check of the Neutron Activation Analysis is the direct dose measurements of 1 MeV equivalent neutrons in silicon by irradiating PIN-diodes<sup>3</sup>. This technique is described and calibrated in [63]. For the calibration, the PIN-diodes are irradiated with diverse proton beams, like 24 GeV protons from IRRAD1 facility at CERN or with neutron sources, like the *Jozef Stefan Institut* TRIGA reactor in Ljubljana,

<sup>3</sup>See Subsection 3.1.3 for an explanation of the semiconductor properties

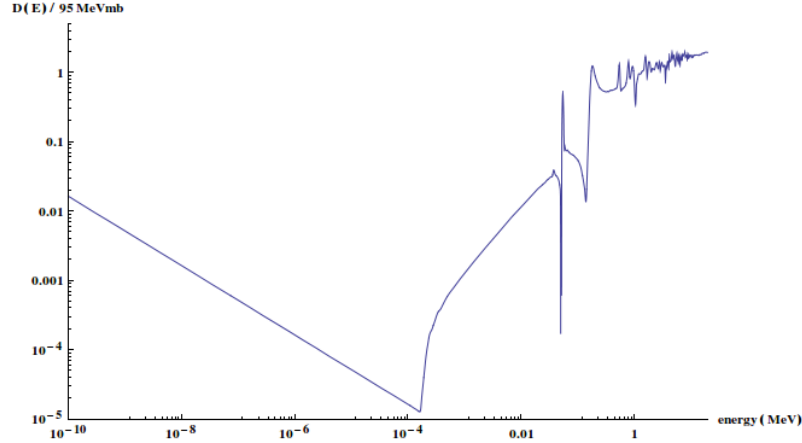


Figure 5.6: The silicon displacement function for the energy range from  $1 \times 10^{-10}$  MeV up to 20 MeV is plotted. The general 1 MeV normalization to 95 MeV mb, as for example in [63], [46], is applied. The data is taken from [27] and converted from ENDF file format by [32].

Slovenia.

The diodes are operated in forward bias and the voltage drop over this diode at a defined operation current is measured before and after irradiation. The difference of these voltage drops,  $\Delta V = V_{after} - V_{before}$  is in a certain range (see Table 5.3) linearly proportional to the radiation dose of 1 MeV neutrons.

$$\Delta V = c \cdot \int \Phi_{eq} dt \Leftrightarrow \int \Phi_{eq} dt = \frac{1}{c} \cdot \Delta V \quad (5.24)$$

For the LBSD Si-2 diode at integrated fluences above  $1 \times 10^{11} \text{ n}_{eq} \text{ cm}^{-2}$ , a logarithmic model is used to describe the increasing forward biased voltage drop.

$$\Delta V = A \cdot \ln(\Phi_{eq}) + B \quad (5.25)$$

The calibration parameters,  $A$  and  $B$ , are soon going to be published in a new version of [62] and the fluences in this thesis are determined by private communication with the author<sup>4</sup>.

Different diodes are available and characterized by [63], i.e. the constant  $c$  for each type of diode is measured. The calibration is performed by irradiating the diodes with well known radiation sources and measuring the voltage drop over the diode. Two types of these diodes are used in this thesis for the determination of the neutron dose in the reactor in Mainz (Subsection 5.3.2) and for the AmBe source in house (Subsection 5.3.1). The constant  $c$  and the sensitive fluence range for the used types of diodes is given in Table 5.3.

<sup>4</sup>Federico Ravotti: [Federico.Ravotti@cern.ch](mailto:Federico.Ravotti@cern.ch)

PIN diodes	Sensitive range [ $n_{\text{eq}} \text{ cm}^{-2}$ ]	calibration $\frac{1}{c} [\frac{\text{cm}^{-2}}{\Delta V}]$
LBSD Si-2	$10^{10} - \cdot 10^{11}$	$2.7 \cdot 10^{10}$
	$> 10^{11}$	logarithmic relation [61]
BPW34F	$10^{12} - 10^{14}$	$9.1 \cdot 10^{12}$

Table 5.3: The parameters of two different PIN-diodes used for the measurement of the normalized neutron fluence. The calibration constant  $\frac{1}{c}$  of both diodes has a uncertainty of 15% [63].

## 5.3 Irradiation facilities

The first neutron source is an AmBe source located in the Physikalisches Institut. With this source, an accumulated dose of about  $9.8 \times 10^{10} n_{\text{eq}} \text{ cm}^{-2}$  is reached after 32 days of radiation at a flux of  $3.5 \times 10^4 n_{\text{eq}} \text{ cm}^{-2} \text{ s}^{-1}$ , which corresponds to the expected neutron dose after collecting  $4\text{-}5 \text{ fb}^{-1}$  with the LHCb experiment. The other irradiation facility is the TRIGA Mark II neutron fission reactor in Mainz. At the reactor, the maximal dose given to a SiPM of about  $1.9 \times 10^{12} n_{\text{eq}} \text{ cm}^{-2}$  is exceeding the SiPM's expected lifetime dose of  $1.3 \times 10^{12} n_{\text{eq}} \text{ cm}^{-2}$  at the SciFi tracker.

### 5.3.1 AmBe source

The Americium Beryllium source is comprised of  $^{241}\text{Am}$ , an  $\alpha$ -emitter and  $^9\text{Be}$ , which has a high ( $\alpha, n$ )-cross-section:



This combination of materials has a high yield of fast neutrons. From an activity of 3.7 GBq per source, one receives a neutron emission rate of  $2.2 \times 10^5 \text{ s}^{-1}$  [7]. In the Physikalisches Institut there are three almost identical neutron sources, labeled 434, 4116 and 4117. The active material is placed inside a cylindrical stainless steel container, which are positioned in a triangular shape around a central holder for SiPMs. The distance from the central axis of each source to position of the SiPMs is 13.0 mm. The cylinder's outer dimensions are  $h = 19.2 \text{ mm}$  with a diameter of  $d = 17.4 \text{ mm}$ .

For the Neutron Activation Analysis, only one source is positioned on the bottom of a box, whereas the other two sources are removed from the setup. This box is sketched in Figure 5.7 and has outer dimensions of  $74.0 \text{ cm} \times 97.5 \text{ cm} \times 63.0 \text{ cm}$  and is made out of a 15 cm thick wall of borated Polyethylene (PE)<sup>5</sup>, which is covered with a 2.5 cm thick lead shielding. The PE is used as a moderator and the additional boron inside the PE has a large neutron capture cross-section at thermal energies and therefore absorbs the moderated neutrons. This seems to create an environment free of thermal neutrons inside the inner air volume of the box. The additional lead

<sup>5</sup>Polyethylene consists of  $(\text{H}_2\text{C})_n\text{H}_2$ -chains and therefore has a high hydrogen concentration

coating prevents thermal neutrons or produced gammas from emerging the setup. During the activation process, the samples for the Neutron Activation Analysis are placed directly on the lateral surface of the source. The determined neutron flux corresponds to the ratio of the source's neutron yield and the cylinder surface.

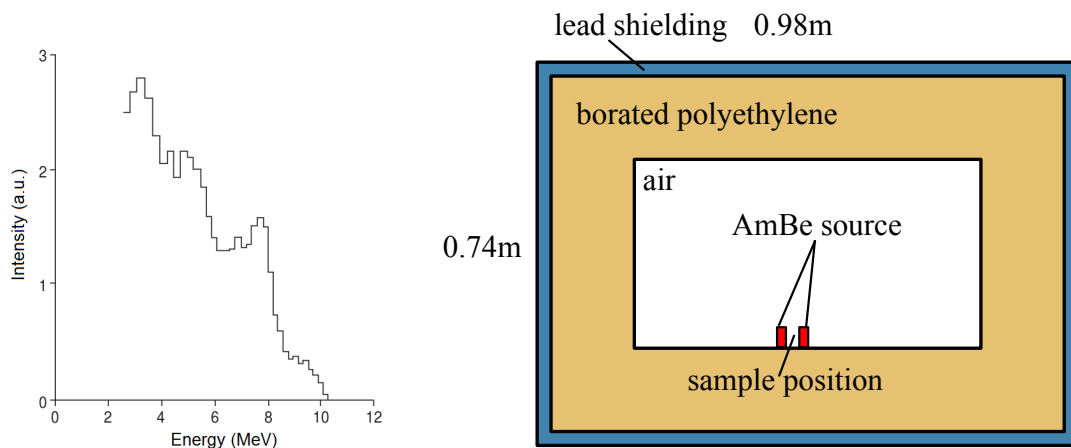


Figure 5.7: Left: The neutron energy spectrum of the  $^{241}\text{Am}^9\text{Be}$  source, as it is provided by the producer. The normalization of this distribution for one neutron is 0.77, since 23% of the neutrons are located in the low energy tail not included in the spectrum [7]. Right: The schematic sketch shows a cross-section through the setup. The small red boxes indicate the neutron sources on the bottom of a box, which is made out of borated polyethylene with an outer lead shielding. The SiPMs are positioned in between the sources. The sketch is not to scale.

## Results

The measurement results are displayed in Table 5.4.

Neutron source	Flux [ $\text{cm}^{-2} \text{s}^{-1}$ ]
AmBe-source 434	$10697 \pm 425(\text{stat}) \pm 2300(\text{sys})$
AmBe-source 4116	$10977 \pm 431(\text{stat}) \pm 2360(\text{sys})$
AmBe-source 4117	$12908 \pm 467(\text{stat}) \pm 2776(\text{sys})$
Total	$34582 \pm 761(\text{stat}) \pm 7435(\text{sys})$

Table 5.4: Measured neutron fluxes for the three AmBe-sources at the cylinder surface at a distance of half the diameter  $\frac{d}{2} = 8.7 \text{ mm}$  from the source. The flux at the cylinder surface is assumed to be homogeneously distributed. The statistical and systematic errors are given for each source. The spectrum of these resulting fluxes is the emission spectrum shown in Figure 5.7

The neutron flux close to the sources is expected to reduce linearly with the distance, which is a plausible assumption due to the cylindrical geometry. Therefore the neutron flux at the position where the SiPMs are irradiated requires a geometrical correction with respect to the measured flux on the surface

$$K_{GEO} = \frac{R_{cyl} + 0.5 \text{ mm}}{R_{SiPM}} = \frac{9.2 \text{ mm}}{13.0 \text{ mm}} = 0.67 \quad (5.27)$$

The additional 0.5 mm corresponds to half the thickness of the sample materials. The resulting flux of 1 MeV equivalent neutrons for the SiPM irradiation is determined with the hardness factor from Table 5.2 and the geometrical correction  $K_{GEO}$

$$\Phi_{eq}^{AmBe} = 35315 \pm 777(stat) \pm 10383(sys) \text{ n}_{eq} \text{ cm}^{-2} \text{ s}^{-1} \quad (5.28)$$

with the systematic uncertainty of the neutron flux measurement combined with the uncertainty of the hardness factor.

This result is cross-checked by an irradiation of a LBSD Si-2 diode as described in Section 5.2. Due to the relatively low flux, the irradiation is performed over a time of almost 13 days. The annealing effects during this time are taken into account by assuming an additional systematic error of 10%, resulting in a total systematic uncertainty of 18.0%.

$$\Phi_{eq}(\text{LBSD Si-2}) = 35406 \pm 6373(sys) \text{ n}_{eq} \text{ cm}^{-2} \text{ s}^{-1} \quad (5.29)$$

This value is in very good agreement with the determined flux from the NAA measurements.

### SiPM irradiation settings

Two SiPMs<sup>6</sup> are irradiated in this source. The irradiation is interrupted at regular intervals by measurements of the SiPM's DC, DCR and recording of signal waveforms. With a neutron dose of about

$$\Phi_{eq}^{AmBe} = 3.05 \pm 0.07(stat) \pm 0.90(sys) \times 10^9 \text{ n}_{eq} \text{ cm}^{-2} \text{ day}^{-1} \quad (5.30)$$

the SiPMs are given exponentially increasing doses between each measurement. Starting with one day the accumulated dose is always double by the next irradiation up to a total irradiation duration of 32 days equal to a total dose about  $9.8 \times 10^{10} \text{ n}_{eq} \text{ cm}^{-2}$ . The complete irradiation is executed at room temperature and with no bias voltage or connections attached. A further SiPM<sup>7</sup> is not irradiated and measured as a reference to assure the stability of the measurement setup and exclude any aging effects.

The results of the irradiation are discussed in Chapter 7.

---

<sup>6</sup>Serial No. 160 and 161

<sup>7</sup>Serial No. 159

### 5.3.2 Mainz TRIGA reactor

The Mainz Training, Research, Isotopes, General Atomic (TRIGA) Mark II reactor is sited on the campus of the Johannes Gutenberg University Mainz. The facility was officially opened in 1967 by Otto Hahn after the first critical, self-sustaining operation was performed in 1965. Today, 75 fuel rods with 20% concentrated  $^{235}\text{U}$  are placed inside the reactor. With an amount of 36 g per rod, the total amount of Uranium in the reactors core is about 3.2 kg [1]. The reactor has a normal operation power of 100 kW in terms of thermal heating. It is used for research and training purposes only. These and further information about the reactor are outlined in [38] and [44].

For the investigation of irradiation damage, the neutron research reactor in Mainz is used to irradiate SiPMs with a high neutron dose in the order of  $1 \times 10^{12} \text{ n}_{\text{eq}} \text{ cm}^{-2}$ .



Figure 5.8: Left: A photo of the reactor inside the reactor hall. The control room is in the top corner. Right: A look into the swimming pool from the top of the reactor is shown. Blue Cherenkov light is visible [5].

The flux of thermal and fast neutrons in the reactor at a thermal power of 100 kW is measured by Neutron Activation Analysis. Every sample is positioned in a capsule and shot into the reactor with an air pressure system<sup>8</sup>. A resulting spectrum

<sup>8</sup>The system is referred to as *Rohrpost 2*, German for *pneumatic post 2*

of an activated sample containing aluminum and gold is shown in Figure 5.9. To

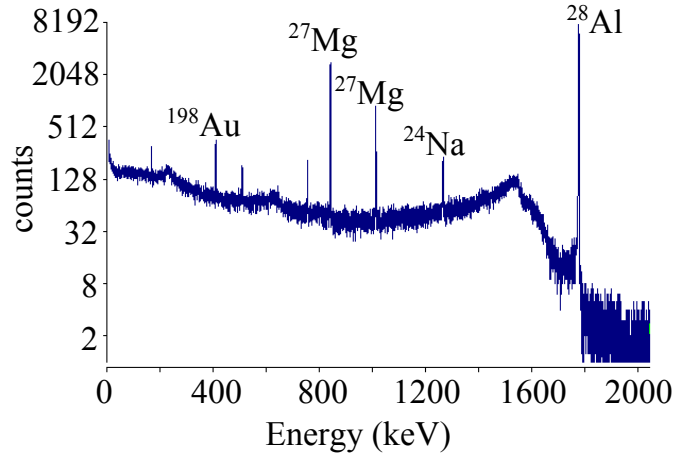


Figure 5.9: A measured spectrum of sample, which was irradiated in the neutron reactor in Mainz. The gamma lines of all three activation products of aluminum, which are shown in Equation 5.2 to 5.4, are visible. Further, the thermally activated product of gold is visible. The number of gammas is used to determine the neutron flux of the reactor.

determine the activation performed by the thermal neutron flux, the same activation was performed with and without Cadmium (Cd) shielding. Cadmium has a very high cross section for thermal neutrons and prevents their transmission by absorption. The thermal neutron flux is used to compare the measurement technique with known values of the neutron reactor. For the fast neutron flux only assumptions are available, since the value has not been measured precisely to this point. Therefore the measurement of this flux is performed in the course of this thesis. For the energy distribution of the fast neutrons, the Watts fission spectrum equation is assumed [46, 67]

$$W(E) = \sqrt{\frac{4}{\pi a^3 b}} \cdot \exp\left(-\frac{ab}{4} - \frac{E}{a}\right) \cdot \sinh\sqrt{bE} \quad (5.31)$$

with the parameters  $a = 0.988 \text{ MeV}$  and  $b = 2.249 \text{ MeV}^{-1}$ .

The activation of aluminum and gold by thermal neutrons at a reactor power of 100 kW results in a flux of

$$\Phi_{thermal} = 1.57 \pm 0.04(stat) \pm 0.23(sys) \times 10^{12} \text{ cm}^{-2} \text{ s}^{-1} \quad (5.32)$$

This value is in very good agreement of former measurements of the thermal neutron flux.

The analysis of the flux of fast neutrons results in

$$\Phi_{fast} = 4.91 \pm 0.14(stat) \pm 0.72(sys) \times 10^{11} \text{ cm}^{-2} \text{ s}^{-1} \quad (5.33)$$

And with the hardness factor given in Table 5.2 the equivalent 1 MeV neutron flux at a reactor power of 100 kW is

$$\Phi_{eq}^{Mainz} = 5.15 \pm 0.15(stat) \pm 0.75(sys) \times 10^{11} \text{ cm}^{-2} \text{ s}^{-1} \quad (5.34)$$

In addition both types of PIN-diodes are used at different doses to verify the NAA measurement and to compare the neutron flux of the reactor with the neutron flux of the AmBe source in Heidelberg. The measurement of the neutron flux at a power of 100 kW using a total of six diodes of type BPW34F (see Table 5.3) at different doses results in

$$\Phi_{eq}(BPW34F) = 8.35 \pm 0.20(stat) \pm 1.25(sys) \times 10^{11} \text{ cm}^{-2} \text{ s}^{-1} \quad (5.35)$$

where the statistical error is the standard deviation of the different measurements and the systematic uncertainty comes purely from the uncertainty of the calibration factor  $\frac{1}{c}$  from Subsection 5.1.6. The uncertainty of the long irradiation duration is negligible.

One diode of type LBSD Si-2 at a reactor power of 1 kW (see next paragraph) gives the result

$$\Phi_{eq}(\text{LBSD Si-2}) = 6.12 \pm 1.37(sys) \times 10^9 \text{ cm}^{-2} \text{ s}^{-1} \quad (5.36)$$

with the systematic uncertainty on the logarithmic calibration and the uncertainty of the irradiation duration of 10% due to the short irradiation of 25 s.

### Reactor operation at 1kW

Due to the high neutron flux at a power of 100 kW the reactor is operated a power of 1 kW for the SiPM irradiation. The flux is expected to scale linearly with the operation power.

The two PIN diode measurements result in a reduction factor  $R_{100}$  between the reactor operation at 100 kW and 1 kW of

$$R_{100} = 136 \pm 37(sys) \quad (5.37)$$

where the systematic uncertainty is treated as uncorrelated and the statistical uncertainty of the former measurement is neglected. The value therefore is compatible with the expected reduction of the neutron flux by a factor 100. A cross-check of this reduction is performed by NAA with short wires made out of an Al-Au alloy. The results of the measured activities at different operation power and same irradiation duration are shown in Table 5.5. The NAA as well confirms the reduction of the neutron flux by about a factor 100.

Since the measurements using the PIN diodes and the scaling factor from the NAA agree, the accepted neutron flux for the SiPM irradiation is taken from the LBSD Si-2 measurement

$$\Phi_{eq}(\text{LBSD Si-2}) = 6.12 \pm 1.37(sys) \times 10^9 \text{ cm}^{-2} \text{ s}^{-1} \quad (5.38)$$

<b>Isotope</b>	<b>Activity(100 kW)Bq mg<sup>-1</sup></b>	<b>Activity(1 kW)Bq mg<sup>-1</sup></b>	<b>Ratio <math>R_{100}</math></b>
<sup>198</sup> Au	437 ± 1.3%	4.2 ± 2.3%	104 ± 4.4%
<sup>24</sup> Na	44.5 ± 2.0%	0.4 ± 18.0%	111 ± 18.1%
<sup>27</sup> Mg	1.94 × 10 <sup>4</sup> ± 2.0%	174 ± 4.0%	110 ± 4.5%
averaged			108 ± 6.4%

Table 5.5: The activity of different isotopes at a reactor power of 100 kW and 1 kW. The ratio is used to investigate the expected reduction of a factor 100 for the reduced reactor operation power.

### SiPM irradiation settings

Four SiPMs<sup>9</sup> are irradiated individually in the reactor at a power of 1kW. They are positioned in a Cd-shielded capsule and shot into the reactor using the same pneumatic post system as described in the previous paragraph. The irradiation duration of each SiPM differs to expose the SiPMs to different neutron doses. Contrary to the irradiation with the AmBe source, every SiPM is irradiated only once. The temperature during the irradiation is the ambient temperature of the reactor and the swimming pool water, which is in the order of 30 – 60 °C [2].

<sup>9</sup>Serial No. 163,164,166 and 168

# PROTON IRRADIATION

---

The advantage of proton irradiation is the high precision of the proton beam flux compared to neutrons, due to electric charge of protons. The proton beam inside an accelerator consists of mono energetic protons with a well known beam profile. This allows an irradiation at a proton facility while performing in-situ measurement. The accelerator beam pipe usually directs into a laboratory where the experiment is positioned directly behind the exit window of the beam pipe. The irradiated SiPM can be operated on the spot and it can be biased during the irradiation itself without irradiating the surrounding experimental setup.

The silicon hardness factor of protons in the energy range of a few 100 MeV is in the same order as 1 MeV neutrons.

$$\kappa = 1.285 \pm 0.050 \quad (6.1)$$

The value is taken from Figure 6.1.

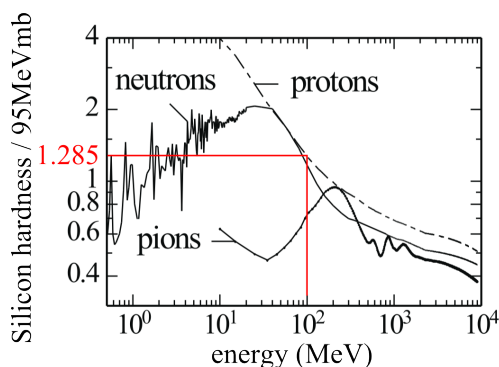


Figure 6.1: The normalized irradiation damage function for different particles, normalized to the damage of 1 MeV neutrons. The red lines indicate the 100.46 MeV proton hardness factor of  $\kappa = 1.284$  [46]. (modified)

## 6.1 Heidelberg Ionenstrahl-Therapiezentrum

The Heidelberg Ionenstrahl-Therapiezentrum<sup>1</sup> (HIT) is a medical radiation institute in Heidelberg [57, 47]. It is on the campus *Im Neuenheimer Feld* and belongs to the *UniversitätsKlinikum* Heidelberg. This facility uses protons and isotopes such as carbon (C) to irradiate tumors in cancer patients. The proton or isotope irradiation deposits a certain energy dose in the tumor tissue to break cell structures and DNA. This irradiation is a possible treatment of inoperable tumors. The main advantage of hadron irradiation is the non homogeneous energy deposition in the tissue compared to other irradiation with for example X-rays or electrons. Hadrons deposit most of their energy close to the end of their penetration into the tissue. This effect results in the so called Bragg peak and is caused by the high cross section of low energetic hadrons. Nevertheless the proton beam for the irradiation has to be known to a very high precision to prevent damages to healthy tissue surrounding the tumor. This high precision is made use of for the irradiation of a SiPM.

### SiPM irradiation settings

A 100.36 MeV proton beam with a two dimensional Gaussian profile is used to deposit at total dose of about  $1.76 \times 10^{12} \text{ n}_{\text{eq}} \text{ cm}^{-2}$  onto one SiPM<sup>2</sup>. The proton flux of the proton accelerator is not continuous, but the dose is deposited in small packages, the so called spills. The proton current is well known during a spill and the spill's duration defines the total disposed fluence per spill. The duration of a spill is determined by observing the beam activity throughout the measurement with a time resolution of approximately 250 ms. The average spill duration is 2.34 s, which is determined by a single-Gaussian fit, which is shown in Figure 6.2.

The resulting systematic uncertainty is taken from the distribution width  $\sigma = 0.15 \text{ s}$ , which corresponds to a relative uncertainty of 6.4%. All systematic uncertainties are summarized in Table 6.1. The resulting average proton fluence per spill is  $\Phi_{\text{spill}}^p = 4.68 \times 10^9 \text{ spill}^{-1}$ . The beam profile with a FWHM<sup>3</sup> of 15.7 mm for the 100.46 MeV proton beam results in a fluence per spill in the central square millimeter of

$$\Phi_{\text{mm}^2}^p = 1.66 \times 10^9 \text{ cm}^{-2} \text{ spill}^{-1} \quad (6.2)$$

which is determined using the fraction factor  $F$  from the 2D Gaussian as

$$F = \int_{-0.5 \text{ mm}}^{0.5 \text{ mm}} \int_{-0.5 \text{ mm}}^{0.5 \text{ mm}} \text{Gaus}(x, y) dx dy \times 100 \frac{\text{mm}^2}{\text{cm}^2} = 0.355 \text{ cm}^2 \quad (6.3)$$

with the factor 100 to normalize to squarecm. The setup is aligned with a precision of 2 mm which results in an asymmetric systematic uncertainty of the proton flux

<sup>1</sup>German for Heidelberg Ion-Beam Therapy Center

<sup>2</sup>Serial No. 162

<sup>3</sup>FWHM = full width at half maximum of a normal distribution. For a Gaussian distribution the FWHM can be determined from the width  $FWHM = 2\sqrt{2\ln(2)}\sigma$

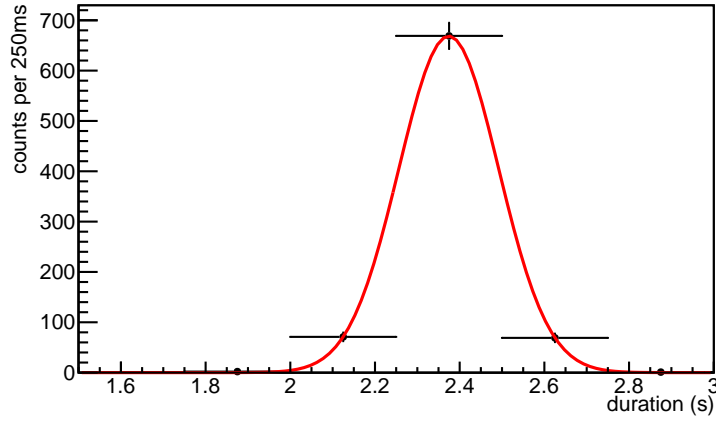


Figure 6.2: The distribution of the spill duration of the proton beam. The mean duration with the corresponding uncertainty from the Gaussian fit are listed in the text.

of  $^{+0\%}_{-9\%}$  with respect to the ideal position in the center of the Gaussian beam profile. Via the multiplication with the hardness factor of protons in silicon, the resulting 1 MeV neutron fluence per spill in the central  $1 \text{ mm}^2$  is

$$\Phi_{eq} = 2.13^{+0.25}_{-0.32}(\text{sys}) \times 10^9 \text{ cm}^{-2} \text{ spill}^{-1} \quad (6.4)$$

**Systematic errors:**

spill duration	6.4%
beam profile	-9% (asymmetric)
hardness factor	10%
total (sys)	+11.9%
	-14.9%

Table 6.1: Summary of the distributions to the systematic uncertainty of the neutron equivalent fluence by proton irradiation

The dose deposition onto the SiPM is interrupted by measurements of the DC at  $T = -30^\circ\text{C}$ . Throughout the entire irradiation process, the SiPM was continuously cooled down to  $T = -30^\circ\text{C}$  and biased during the irradiation  $V_{BIAS} = V_{BD} + 1.2 \text{ V}$ .

## RESULTS

A total of eight SiPMs are used for the studies of temperature dependence and irradiation induced performance changes. The list of these SiPMs is found in Table A.1. Seven of these SiPMs undergo irradiation in the different irradiation sources mentioned in Chapter 5 and 6. Whereas the eighth detector is used as a reference. In the following section the temperature dependence of the SiPMs is investigated before moving to the results of the different irradiation studies. If not mentioned otherwise, the temperature dependence is determined from the non-irradiated reference SiPM<sup>1</sup> as a representative of all eight SiPMs<sup>2</sup>.

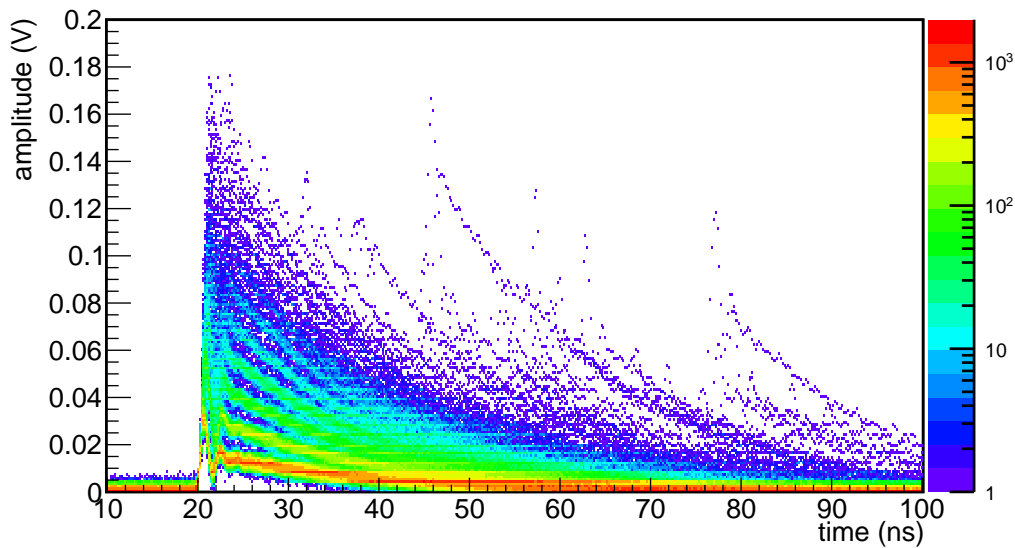


Figure 7.1: The accumulation of 5000 dark signal waveforms of SiPM No. 159 at temperature  $T = 15^\circ\text{C}$  and operation voltage  $V = 66.6\text{ V}$ , which corresponds to an over-voltage  $V_{OV} = 3.0\text{ V}$ . The signal amplitudes of multiple photoelectron peaks due to crosstalk are clearly visible.

<sup>1</sup>Serial No. 159

<sup>2</sup>See Figure 7.4 for a validation of this assumption

## 7.1 Temperature dependence

### Gain & breakdown voltage

The temperature dependence of the breakdown voltage shows a linear behavior over the temperature range from  $-35^{\circ}\text{C}$  to  $20^{\circ}\text{C}$  as shown in Figure 7.2. The determination of this correlation is the most essential measurement, since it is required for the correct conversion of operation voltage to over-voltage at each temperature, as it is shown in Equation 3.9. Further temperature dependencies are always compared at the same over-voltage to correct for the effect of a changing breakdown voltage. The breakdown voltage at a temperature  $T$  is determined from the extrapolation of a linear fit of gain measurements at different voltages for this temperature  $T$ , as it is shown for multiple temperatures in Figure 7.3 (top). As defined in Section 3.3, the gain is linearly dependent on the over voltage without any offset. This allows to measure the breakdown voltage as the voltage where the extrapolation of the linear fit reaches gain  $G = 0$ .

The slope of the breakdown voltage curve in Figure 7.2 of  $62.66\text{ mV K}^{-1}$  is in very good agreement with the stated value from Hamamatsu of  $\approx 60\text{ mV K}^{-1}$ .

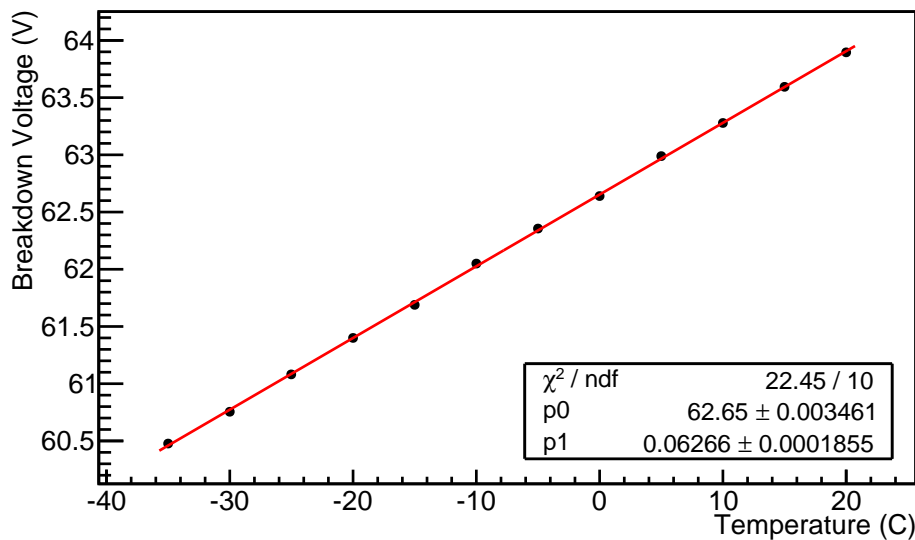


Figure 7.2: The breakdown voltage as a function of the temperature. The expected linear relation is confirmed.

By comparing both plots in Figure 7.3, it is clear that although the breakdown voltage varies with temperature, the gain stays the same at the same over-voltage. This is seen for one single SiPM and, further, below in Figure 7.4 for many SiPMs, where the gain values at same over-voltage for different temperatures are not distinguishable.

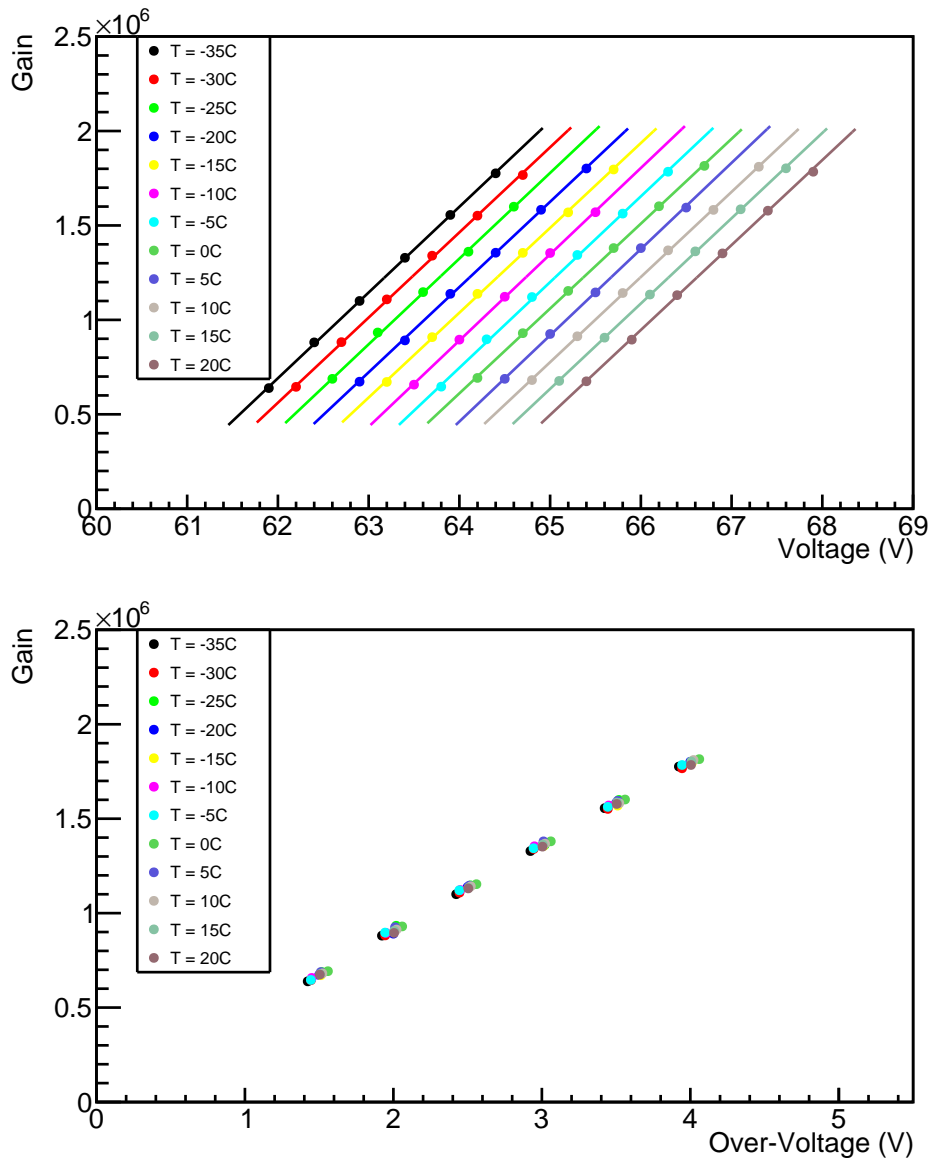


Figure 7.3: Top: The gain as a function of operation voltage at temperatures ranging from  $-35^{\circ}\text{C}$  up to  $20^{\circ}\text{C}$ . The lines are linear fits to the data points. Bottom: The same gain curves as a function of the over-voltage to remove the temperature dependence of the breakdown voltage. The resulting gain curves lie on top of each other and thus show no signs of temperature dependence.

As a verification of the constant properties of all SiPMs throughout the same production series, the gain as a function of the corrected over-voltage is plotted. In Figure 7.4, the gain measurements of all eight used SiPMs are plotted before any irradiation. The plot summarizes measurements at twelve different temperatures for

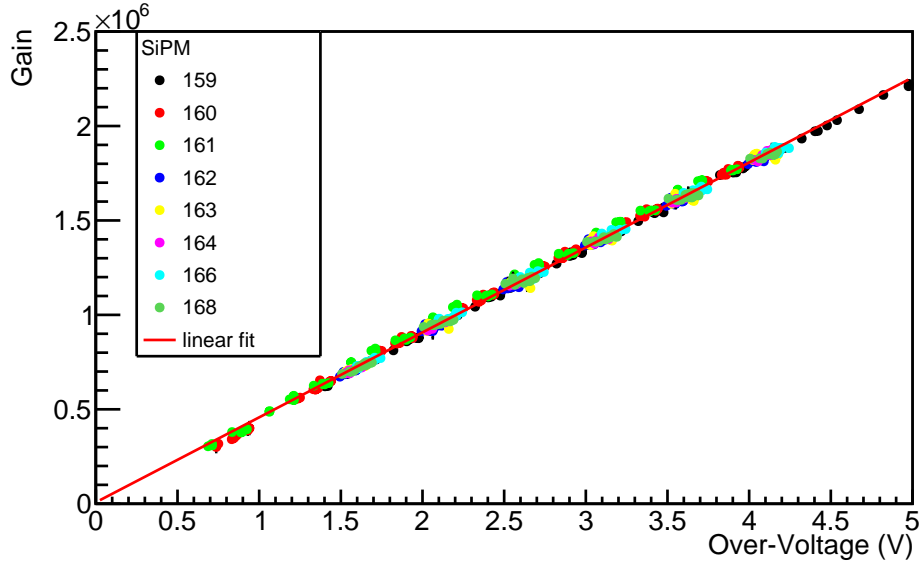


Figure 7.4: Measurements of the gain of all eight used SiPMs over the shown over-voltage range. The datasample for each SiPM consist of measurements at temperatures between  $-35^{\circ}\text{C}$  and  $20^{\circ}\text{C}$ . The gain to over-voltage relation is constant for all SiPMs and for all temperatures. The linear fit is a fit of all data points.

each SiPM. The measurements are performed before any irradiation of the SiPMs. The slope of the global fit describes the correlation between gain and the applied over-voltage.

$$\frac{G(V_{OV})}{V_{OV}} = 4.498 \pm 0.003 \times 10^5 \text{V}^{-1} \quad (7.1)$$

The absolute gain is gauged by injecting a well defined charge into the setup. This is described in Section A.1. For the recommended operation voltage of  $V_{OV} = 2.6 \text{ V}$ , the gain is

$$G(2.6 \text{ V}) = 1.17 \pm 0.01 \times 10^6 \quad (7.2)$$

This value is in good agreement with the value from Hamamatsu of  $G(2.6 \text{ V}) \approx 1.25 \times 10^6$ .

### Crosstalk

A further temperature independent parameter is the crosstalk. At same over-voltage, the different crosstalk measurements are not distinguishable, as clearly visible in Figure 7.5. The crosstalk depends on the over-voltage, as expected due to a higher gain and therefore more electrons per avalanche, but there are no signs of significant deviations over the complete temperature range are observed.

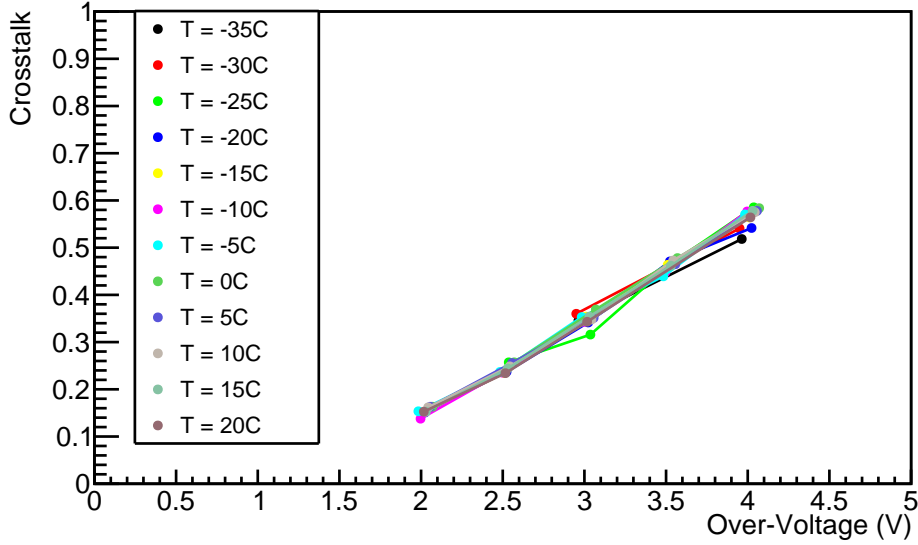


Figure 7.5: The crosstalk probability for a SiPM at temperatures from  $-35\text{ }^{\circ}\text{C}$  up to  $20\text{ }^{\circ}\text{C}$ . The used SiPMs do not contain physical trenches between the pixels to prevent crosstalk. The crosstalk probability at the recommended operation voltage lies in the  $\mathcal{O}(20 - 30\%)$  and it increases with increasing over-voltage. The measurement is in very good agreement with the measurements of Hamamatsu, which are provided in [43].

The probability to trigger a (neighboring) pixel corresponds by definition to the PDE of the SiPM. Therefore, the stability of crosstalk at varying temperature leads to the conclusion that the PDE at same over-voltage must be stable as well.

### Dark count rate & dark current

The former parameters did not show any temperature dependence if the breakdown voltage correction is applied. This is, however, not the case for the dark count rate and the dark current, which is drawn by the SiPM.

The dark count rate is shown on a logarithmic scale for temperatures from  $-35\text{ }^{\circ}\text{C}$  to  $20\text{ }^{\circ}\text{C}$  in steps of  $5\text{ }^{\circ}\text{C}$  and at different operation voltages in Figure 7.6. The projection of the dark count rate at the recommended operation voltage of  $V_{BD} + 2.6\text{ V}$  over the temperature is further shown on the bottom of this figure. The exponential fit to the data points results in a reduction factor  $R_{10}$  of the dark count rate per  $10\text{ }^{\circ}\text{C}$

$$R_{10} = \exp(\alpha_{DCR} \times 10\text{ }^{\circ}\text{C}) = 2.375 \pm 0.007 \quad (7.3)$$

with the exponential fit parameter  $\alpha_{DCR} = 0.086\text{ }50\text{ }^{\circ}\text{C}^{-1}$ .

The dark current is expected to show the same behavior as the dark count rate, since the drawn current of the SiPM is directly correlated to the sum of fired pixels. The measured current is shown in the top plot of Figure 7.7 as a function of the

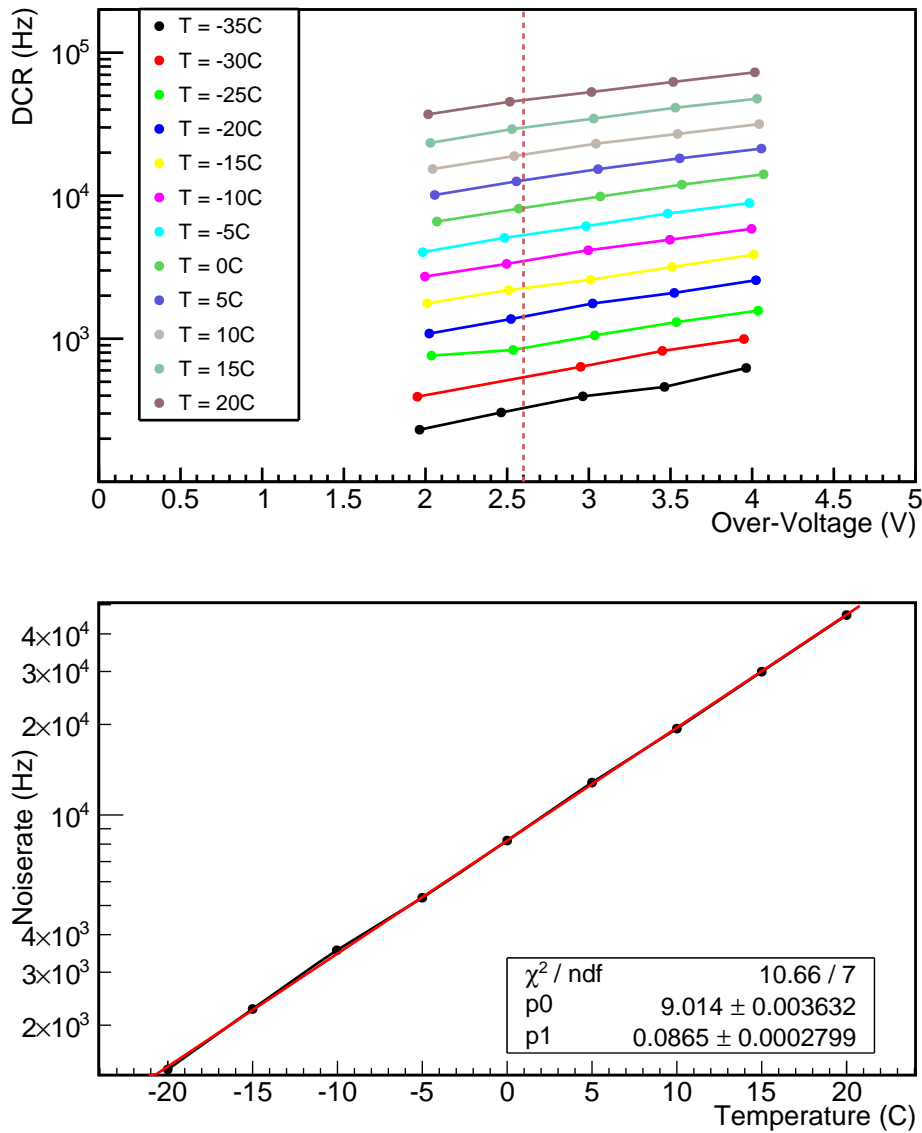


Figure 7.6: Top: The DCR measurements at temperatures from  $-35^\circ\text{C}$  (lowest line) up to  $20^\circ\text{C}$  (topmost line). The dark count rate increases steadily with rising temperature. Bottom: The projection of the DCR at the recommended operation voltage (indicated as the dotted line in the upper figure) is projected onto the temperature. Note the logarithmic scale of the y-axis. The exponential fit allows the determination of the correlation between DCR and temperature (see text for details). Dark count rates below 1 kHz are discarded.

over-voltage. The large error bars on measurements of low currents below 1 nA is probably caused by fluctuations due to the instrument's limitations in the order of

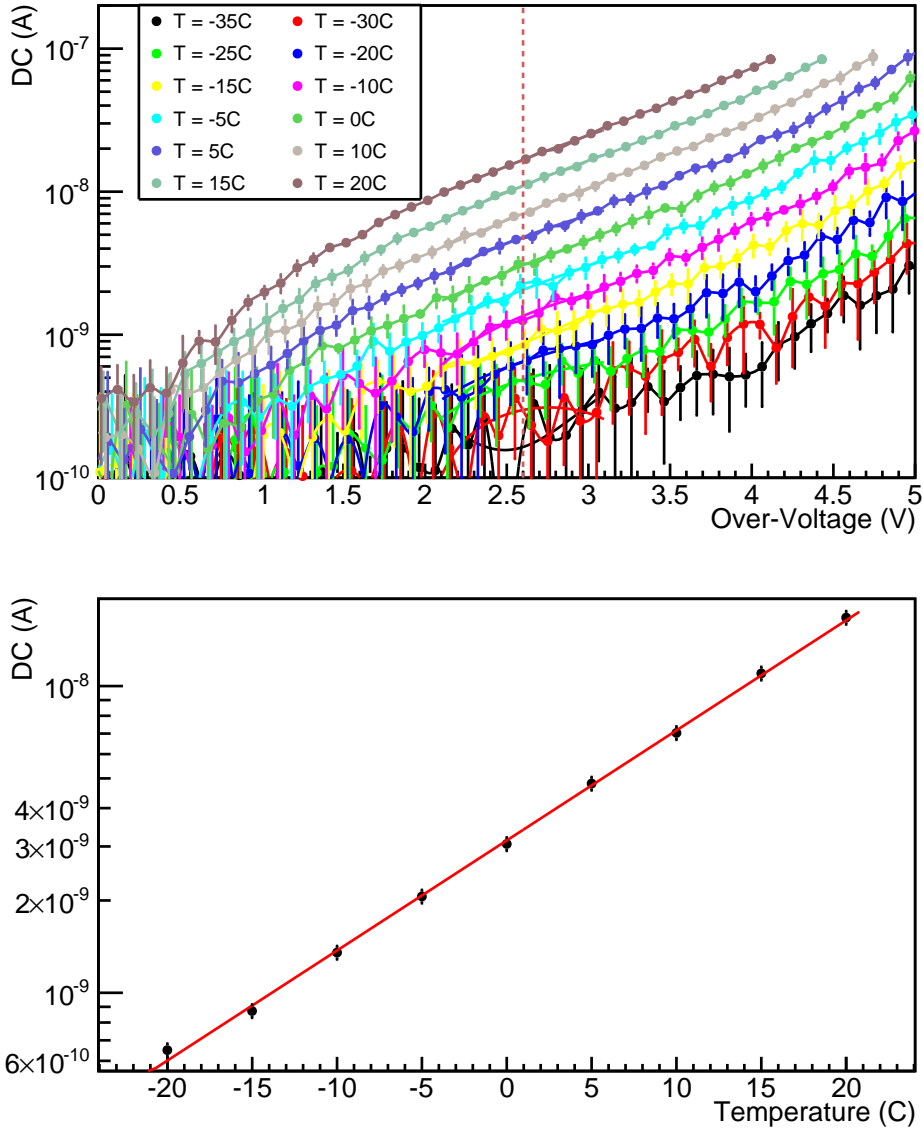


Figure 7.7: The recording of IV curves as shown on the top is performed at the same temperature range and step size as the measurements of DCR and gain. Again the projection at the recommended voltage is projected into the lower figure. Dark currents below 0.5 nA are not considered.

100 pA, which is acceptable.

The projection of the dark current at  $V_{OV} = 2.6$  V is displayed on the bottom including an exponential fit. As before for the DCR, the reduction factor  $R_{10}$  for a 10 °C temperature decrease is determined from the plot

$$R_{10} = \exp(\alpha_{DC} \times 10 \text{ }^\circ\text{C}) = 2.285 \pm 0.031 \quad (7.4)$$

with the exponential fit parameter  $\alpha_{DC} = 0.08262 \text{ }^\circ\text{C}^{-1}$ .

The result of the two reduction factors of dark current and dark count rate are in good agreement, with a relative uncertainty of 3.8%. This shows the direct correlation of dark current and dark count rate over the investigated temperature range.

### Summary

The temperature dependence of the SiPMs shows no deviations from the stated values by the production company. The breakdown voltage changes linearly with the temperature, resulting in unchanged gain and crosstalk properties at constant over-voltage.

The thermally induced dark count rate of the SiPM and the resulting dark current are depending exponentially on the temperature with a reduction factor per 10 °C temperature change of  $2.375 \pm 0.007$  and  $2.285 \pm 0.031$ , respectively.

## 7.2 Radiation effects

The SiPMs irradiation is performed at three different irradiation facilities, which use neutrons and protons for irradiation studies. The facilities, which are introduced in Chapter 5 and 6, are used to deposit different doses on the detectors to obtain a broad range of investigatable irradiation damages. After irradiation the SiPMs are characterized by measuring the parameters dark current and dark count rate. Before presenting the results, a short statement on the measurements of gain and breakdown voltage is given. The results of the DCR and DC measurements are introduced in the following. Afterwards the annealing of irradiation damage is investigated.

### 7.2.1 Gain & Breakdown Voltage

The measurement of the gain of the irradiated SiPM is hardly possible due to the high frequency of the DCR. Signals overlap frequently and, therefore, create integrated charges in between the nicely distinguishable photoelectron peaks, which have been observed before. Further, the high current at high frequencies seems to introduce some oscillations in the pedestal. As a result, the photoelectron peak spectrum as in Figure 3.13 smears out and the required photoelectron peaks are not resolvable. Further, the breakdown voltage cannot be extrapolated from the gain fit.

However, from gain measurements at the lowest temperatures and at low doses of about  $1 \times 10^{10} \text{ n}_{\text{eq}} \text{ cm}^{-2}$  the breakdown voltage does not show any effects on the irradiation dose. Also from IV curves, at which the breakdown voltage can be approximated by the rising edge of the spectrum, the breakdown voltage shows no changes. Therefore, the assumption of an irradiation independent breakdown voltage is considered justified.

### 7.2.2 Dark count rate

The successful particle track reconstruction by the tracking algorithm of the new SciFi Tracker is dependent on the DCR of the SiPM. The SciFi clustering algorithm uses the signal amplitude of a channel, which corresponds to the triggered pixels, to suppress fake noise signals of smaller amplitude. Therefore, the amplitude of the dark count signals is of great interest for the hit detection algorithm. In this thesis, the DCR as a function of triggered pixels is measured at the different irradiation doses. For the different signal amplitudes<sup>3</sup> the following relation between the amplitude threshold at which the DCR is measured and the amount of fired pixels,  $PE + 0.5$ , is obtained empirically from measurements using non-irradiated SiPMs. They are analyzed by setting the position of the trigger threshold level for each photoelectron peak by hand. From the 0.5 PE, 1.5 PE and 2.5 PE trigger threshold, further values are extrapolated linearly.

$$V_{\text{threshold}}(V_{OV}, PE) = -3.1417 \times 10^{-3} \text{ V} + (4.6474 \times 10^{-3} + 6.2520 \times 10^{-3} \cdot PE) \cdot V_{OV}$$

This equation provides the trigger threshold level for a certain photoelectron peak PE at a certain over-voltage  $V_{OV}$ . The step-like DCR spectrum as shown in Figure 3.15 is smeared out after irradiation. Therefore, the trigger level position for each PE at certain over-voltage is applied identically for irradiated SiPMs to obtain the signal amplitude of a certain amount of fired pixels.

In Figure 7.8 the increasing DCR as a function of the delivered dose is shown. The color notation indicates the number of triggered avalanches in a signal. The resulting DCR of signals with at least one triggered avalanche for such a 400 pixel detector with an active silicon surface area of  $1 \text{ mm}^2$  at temperature  $T = -30^\circ\text{C}$  exceeds 10 MHz after a dose of about  $1.3 \times 10^{11} \text{ n}_{\text{eq}} \text{ cm}^{-2}$ , which is expected during one year of operation in the irradiation environment of the LHCb. However, the DCR of signals with five or more triggered avalanches only reaches a rate of  $\mathcal{O}(100 \text{ kHz})$ . The SciFi tracker accepts signal clusters with a total amplitude exceeding 4.5 PE with typically the additional condition that a single channel exceeds 2.5 PE or 3.5 PE. The rate of 2.5 PE signals reaches approximately 1 MHz after the irradiation dose of one year of LHCb operation.

After the total expected lifetime dose of about  $1.3 \times 10^{12} \text{ n}_{\text{eq}} \text{ cm}^{-2}$ , the DCR for the 0.5 PE and 2.5 PE threshold are in the order of 10 MHz, while the 5.5 PE threshold almost reaches a rate of 1 MHz.

Figure 7.9 shows the same data as the former figure, with the DCR at different delivered doses plotted as a function of the threshold in units of PE. The DCR increases linearly with the delivered dose at low doses and continues steadily over the total range of signal amplitudes, but slower than an extrapolation from low doses would expect. Some saturation effects are visible. The overlay at high signal amplitudes and high irradiation doses is probably the result of the off-line corrections of the

<sup>3</sup>The amplitudes are given in units of PE, with  $x.5$  PE being the equivalent voltage amplitude threshold of a signal containing  $x + 1$  avalanches

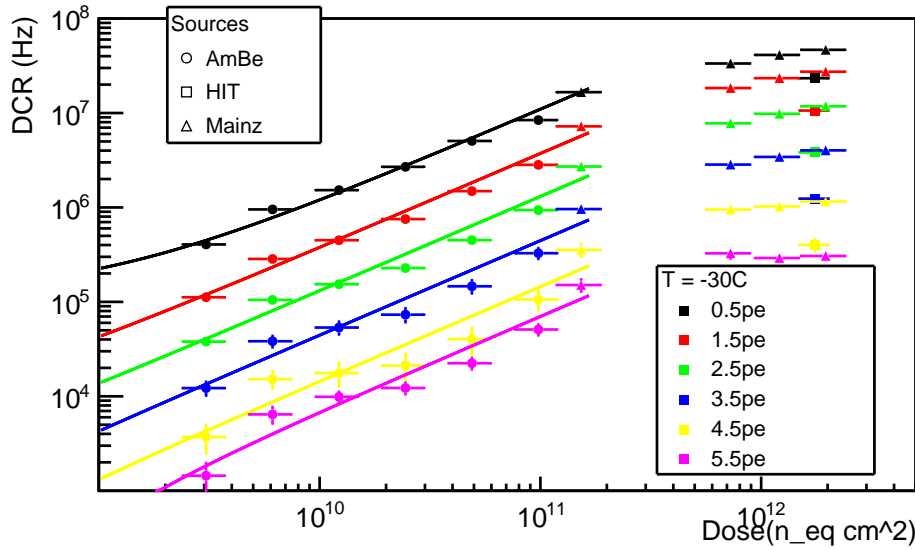


Figure 7.8: The DCR trend of SiPMs at a temperature  $-30^\circ\text{C}$  and  $V_{OV} = 2.6\text{V}$  as a function of the delivered NIEL dose. The color notation indicates different signal thresholds, which indicates to the number of fired pixels. The highest threshold at 5.5 PE takes signals with 6 fired pixels and more into account. The lines are linear fits to the data. The fits' slopes are listed in Table 7.1.

operation voltage due to a high drawn current as mentioned in Section 4.2. The measurement results from the irradiation at the HIT proton beam with a accumulated dose of  $1.75 \times 10^{12} \text{ n}_{\text{eq}} \text{ cm}^{-2}$  shows a systematically lower DCR than expected from the neutron source irradiation. The DCR curve is shown in light grey in Figure 7.9. This feature is further discussed by means of the dark current in the next section.

## Summary

The DCR shows a linear increase with rising irradiation dose throughout all orders of signal amplitude for irradiation doses below  $1.6 \times 10^{11} \text{ n}_{\text{eq}} \text{ cm}^{-2}$ . The resulting proportional constants are summarized in Table 7.1.

At higher doses, the DCR increases slower than expected from linearity and seems to reach saturation at large doses towards  $2 \times 10^{12} \text{ n}_{\text{eq}} \text{ cm}^{-2}$ .

To correctly relate these results to a channel in the SiPM arrays of the SciFi Tracker, the dark count rate is expected to drop by a factor of about 2 due to the reduced operation temperature  $T = -40^\circ\text{C}$  and a further factor 4 due to the amount of pixels per channel<sup>4</sup> or equally the reduced surface area of silicon of one channel.

Therefore the former stated DCRs would reduce by almost one order of magnitude.

<sup>4</sup>The latest Hamamatsu array has 96 pixels per channel of similar pixel size [50]

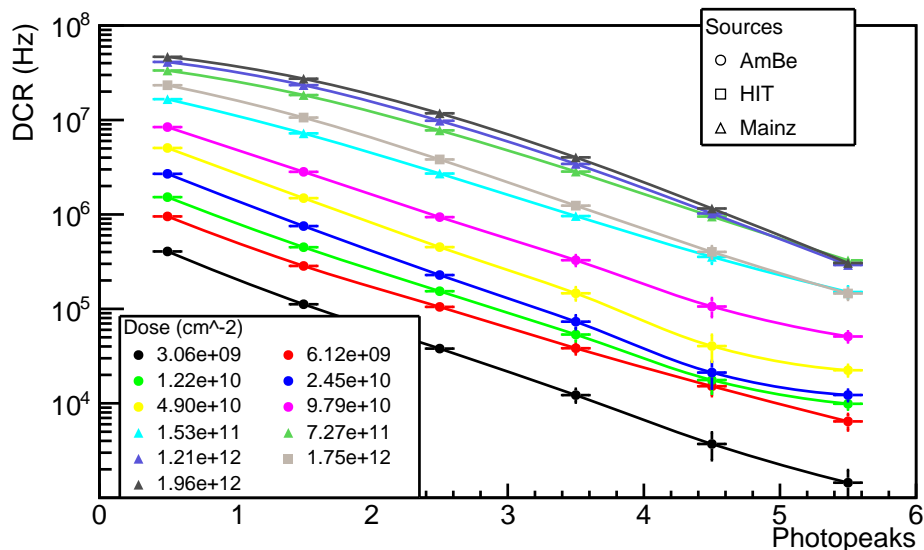


Figure 7.9: The data for this diagram is identical to the information in Figure 7.8, but with reversed projection. The color notation describes the delivered dose in  $\text{n}_{\text{eq}} \text{cm}^{-2}$ . The DCR trend at different doses can be seen to decrease with a rising threshold for the self-triggered signals. The lines are added to guide the eye.

The rate signal with at least one avalanche per one channel in the SiPM array of the SciFi detector increases to about 1 MHz within the first year of LHCb operation and increases further, if no further prevention or annealing (see below) is performed. Signals of higher amplitude increase similar, but with a systematically lower magnitude. The irradiation with protons showed a systematically lower DCR compared to neutron irradiation.

### 7.2.3 Dark current

The dark current is found to match a linear increase as a function of the deposited irradiation dose over the complete investigated range up to a fluence of almost  $2 \times 10^{12} \text{n}_{\text{eq}} \text{cm}^{-2}$ . This counts for all three irradiation studies using neutron and proton irradiation.

The interleaved measurements of the dark current during the HIT irradiation are shown in Figure 7.10. The steady increase of dark current with increasing dose is clearly visible.

The same behavior was observed throughout the measurements at the irradiation with the AmBe neutron source and with the irradiation with the neutron reactor in Mainz. The IV curves of the performed measurements at diverse doses do not differ in shape, but the dark current changes quantitatively in correlation with the delivered dose. For each measurement, the resulting dark current at the recommended

Trigger threshold	DCR increase (Hz n <sub>eq</sub> <sup>-1</sup> cm <sup>-2</sup> ) at $T = -30^\circ\text{C}$
0.5	$1.086 \pm 0.120 \cdot 10^{-4}$
1.5	$3.724 \pm 0.426 \cdot 10^{-5}$
2.5	$1.307 \pm 0.161 \cdot 10^{-5}$
3.5	$4.454 \pm 0.616 \cdot 10^{-6}$
4.5	$1.448 \pm 0.253 \cdot 10^{-6}$
5.5	$7.034 \pm 1.074 \cdot 10^{-7}$

Table 7.1: The linear increase of dark count rate up to a dose of  $1.6 \times 10^{11}$  n<sub>eq</sub> cm<sup>-2</sup> at temperature  $T = -30^\circ\text{C}$  for signal thresholds up to 5.5 PE.

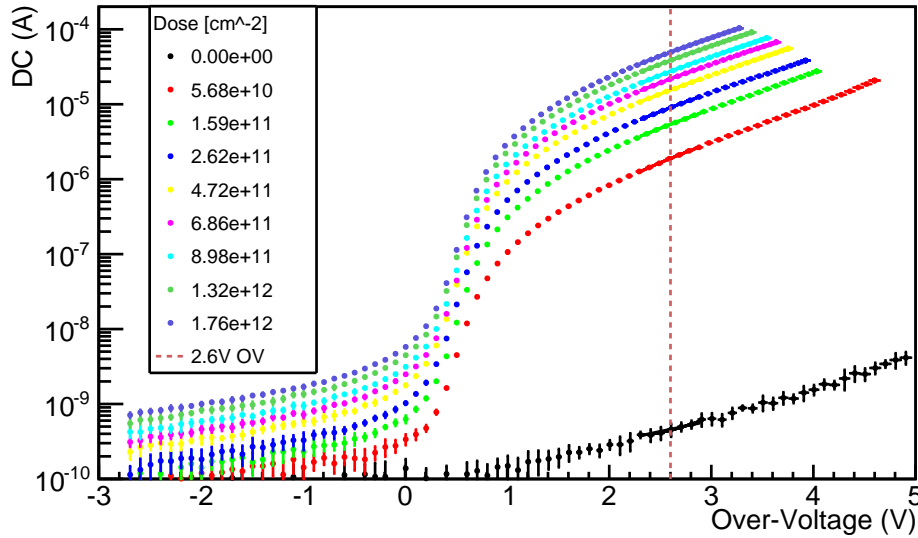


Figure 7.10: The measured IV curves are taken in between the irradiation process at the proton accelerator (HIT). For the measurement, the irradiation process was interrupted. The data is taken at the constant temperature of  $T = -30^\circ\text{C}$ .

operation voltage is determined for a comparison of the three irradiation series.

In Figure 7.11 the final results of the dark current behavior are summarized for all three irradiation series and with the SiPMs operated at the recommended operation voltage and at temperature  $T = -30^\circ\text{C}$ .

The measurements show some significant deviation between the irradiation using protons and the irradiation at the neutron reactor in Mainz. On the background of the double cross-checked neutron fluence of the reactor and the well known properties of the proton beam, this deviation is surprisingly high. Due to the purely systematical deviation, the source is thought to be in the conversion of the irradiation doses to 1 MeV equivalence. This, however, is in contradiction with the former statement of a well calibrated irradiation flux. The exact cause for the deviation

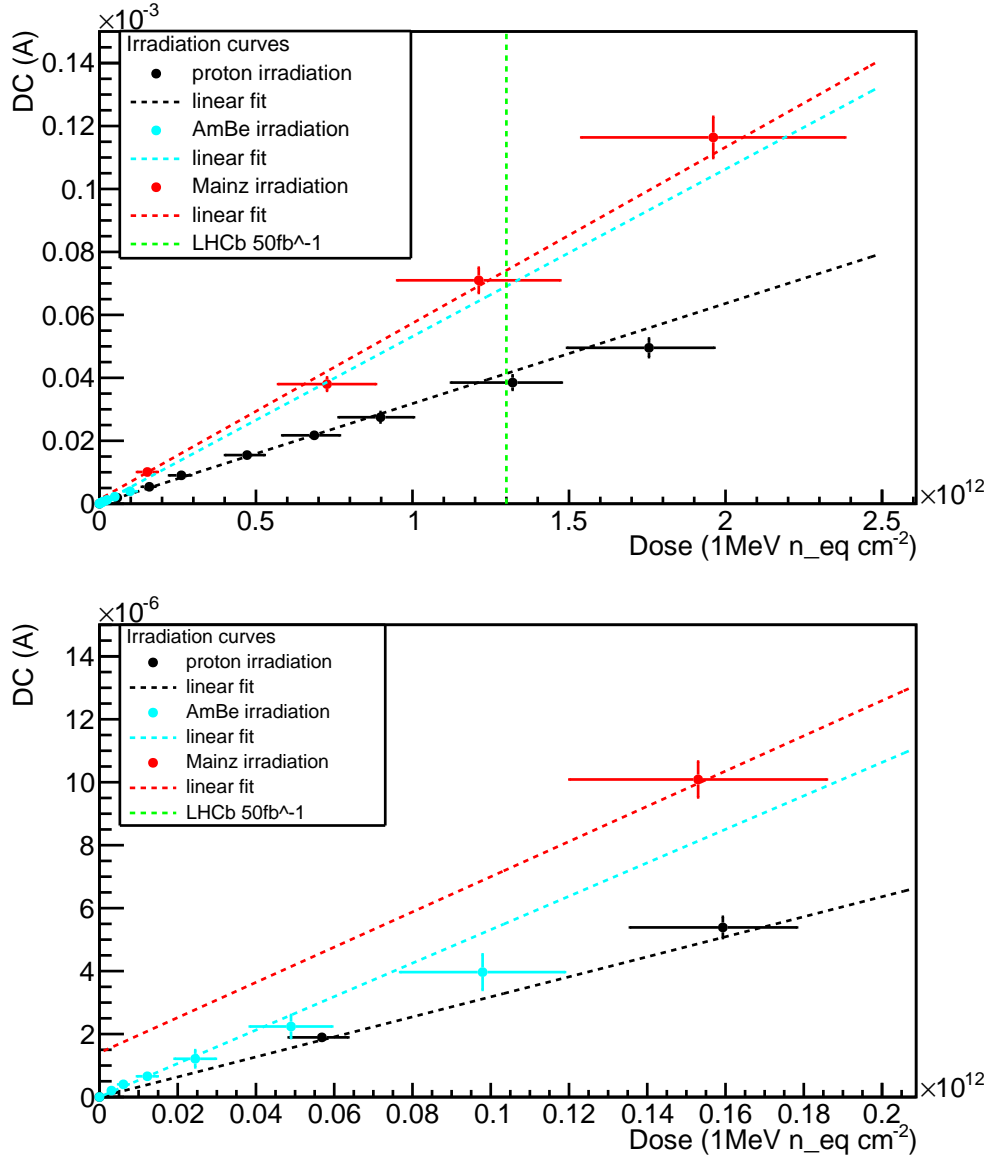


Figure 7.11: The measured DC at a temperature  $T = -30^\circ\text{C}$  and the recommended over-voltage of  $V_{OV} = 2.6\text{ V}$ . The measurements with two SiPMs which are irradiated by the AmBe-source are averaged. The data points of the irradiation at the TRIGA reactor in Mainz correspond to four individual SiPM which obtained different irradiation dose. The HIT measurement was performed with a single SiPM while the data was taken in between the irradiation process. A linear fit of each data sample is performed and extrapolated to the to full range of the diagram. The lower figure is a zoom to the low dose measurements performed with the AmBe source and it is containing the same data.

is not yet understood. One likely cause is the overestimation of the exact proton fluence, which might be reduced due to multiple scattering in the air between the beam pipe exit window and the SiPM, or in a thin ice layer, which covers the SiPM during the alignment procedure.

For the area of low doses from the irradiation using the AmBe source for an integrated flux of below  $1 \times 10^{11} \text{ n}_{\text{eq}} \text{ cm}^{-2}$  no significant deviation between all three measurements is observed.

At the irradiation at the proton facility (HIT) and the irradiation with the AmBe-source a small systematic deviation towards lower dark current at high doses is visible. The cause of this feature is not understood, but causes due to annealing can be excluded. The irradiation at the reactor in Mainz does not show this behavior at high doses. The deviation is not significant and no further investigation has been performed.

## Summary

As a result of the irradiation with neutrons and protons the dark current increases mostly linearly with the delivered dose. For the three irradiation series, some deviations in the increase are found. The resulting slopes are summarized in the following table

<b>Irradiation facility</b>	<b>DC increase (<math>\text{A n}_{\text{eq}}^{-1} \text{cm}^{-2}</math>) at <math>T = -30^\circ\text{C}</math></b>
HIT proton beam	$3.184 \pm 0.167 \times 10^{-17}$
AmBe	$5.314 \pm 0.611 \times 10^{-17}$
Mainz reactor	$5.594 \pm 0.858 \times 10^{-17}$
Global	$3.591 \pm 0.620 \times 10^{-17}$

Table 7.2: The resulting increase of dark current at a temperature of  $-30^\circ\text{C}$  for the three irradiation series.

### 7.2.4 Annealing

To extend the operation time of the SiPMs for the SciFi detector upgrade, it is planned to heat the SiPMs to reduce the damage due to irradiation. The annealing of the irradiation damage is investigated for two annealing temperatures  $T_1 \approx 24^\circ\text{C}$  and  $T_2 = 40^\circ\text{C}$ . The annealing is quantified by means of the dark current. For the annealing at room temperature, the two SiPMs irradiated in the AmBe source are used and compared. The result of the annealing process is shown in Figure 7.12 for both detectors. The four SiPMs from the irradiation studies with the Mainz reactor are baked out at  $T_2 = 40^\circ\text{C}$ . In Figure 7.13, the resulting annealing curves of the dark current are shown. The annealing process is described with an exponential decay curve plus a constant offset.

$$DC(t) = DC_0 \cdot \exp(\lambda t) + DC_\infty \quad (7.5)$$

The exponential part comes from the solution of the differential equation, since the neutron induced damage centers are expected to *decay* with a certain probability, which depends on the annealing temperature. The offset takes into account that only a certain amount of damages can be revoked due to annealing.

The resulting halftimes determined from the exponential fit<sup>5</sup> are summarized in Table 7.3. The obtained values from the annealing at room temperature are compatible with each other. The annealing process at  $T_2 = 40^\circ\text{C}$  shows some deviation in the halftimes, which are not in agreement within the uncertainty from the fit. However, no systematic dependency on the irradiation dose is visible. The reduction factor of the dark current due to the annealing is as well given in Table 7.3. By comparing the data set of annealing at room temperature and at  $T_2 = 40^\circ\text{C}$ , one can clearly see that annealing of the radiation damage is temperature dependent. At  $T_2 = 40^\circ\text{C}$ , the required annealing time is much shorter compared to room temperature annealing. Further, the annealing at  $T_2 = 40^\circ\text{C}$  is more effective, since the dark current reduces by about a factor 2.5, in relation to a factor of about 1.4 for room temperature annealing.

SiPM No.	Radiation dose ( $n_{\text{eq}} \text{ cm}^{-2}$ )	Annealing $T$ ( $^\circ\text{C}$ )	Halftime $T_{1/2}$ (days)	Reduction
160	$10^{11}$	$\approx 24^\circ\text{C}$	$6.281 \pm 0.435$	$1.368 \pm 0.019$
161	$10^{11}$	$\approx 24^\circ\text{C}$	$6.858 \pm 0.508$	$1.426 \pm 0.020$
163	$2 \times 10^{11}$	$40^\circ\text{C}$	$1.032 \pm 0.005$	$2.612 \pm 0.037$
164	$7 \times 10^{11}$	$40^\circ\text{C}$	$0.824 \pm 0.002$	$2.463 \pm 0.035$
166	$10^{12}$	$40^\circ\text{C}$	$0.917 \pm 0.003$	$2.434 \pm 0.034$
168	$2 \times 10^{12}$	$40^\circ\text{C}$	$0.916 \pm 0.007$	$2.343 \pm 0.033$

Table 7.3: The resulting time constant of the annealing effect by means of dark current at a temperature of  $T = -30^\circ\text{C}$  for different annealing temperatures and irradiation doses. The values are determined from fits to Figure 7.12 and 7.13 with the function in Equation 7.5. The reduction of dark current due to the annealing is determined from the ratio of a DC measurement shortly after the irradiation and one measurement after the annealing process.

<sup>5</sup>From the exponential time constant of the decay,  $\lambda$ , the halftime  $T_{1/2}$  is determined as  $T_{1/2} = \frac{-\ln(2)}{\lambda}$

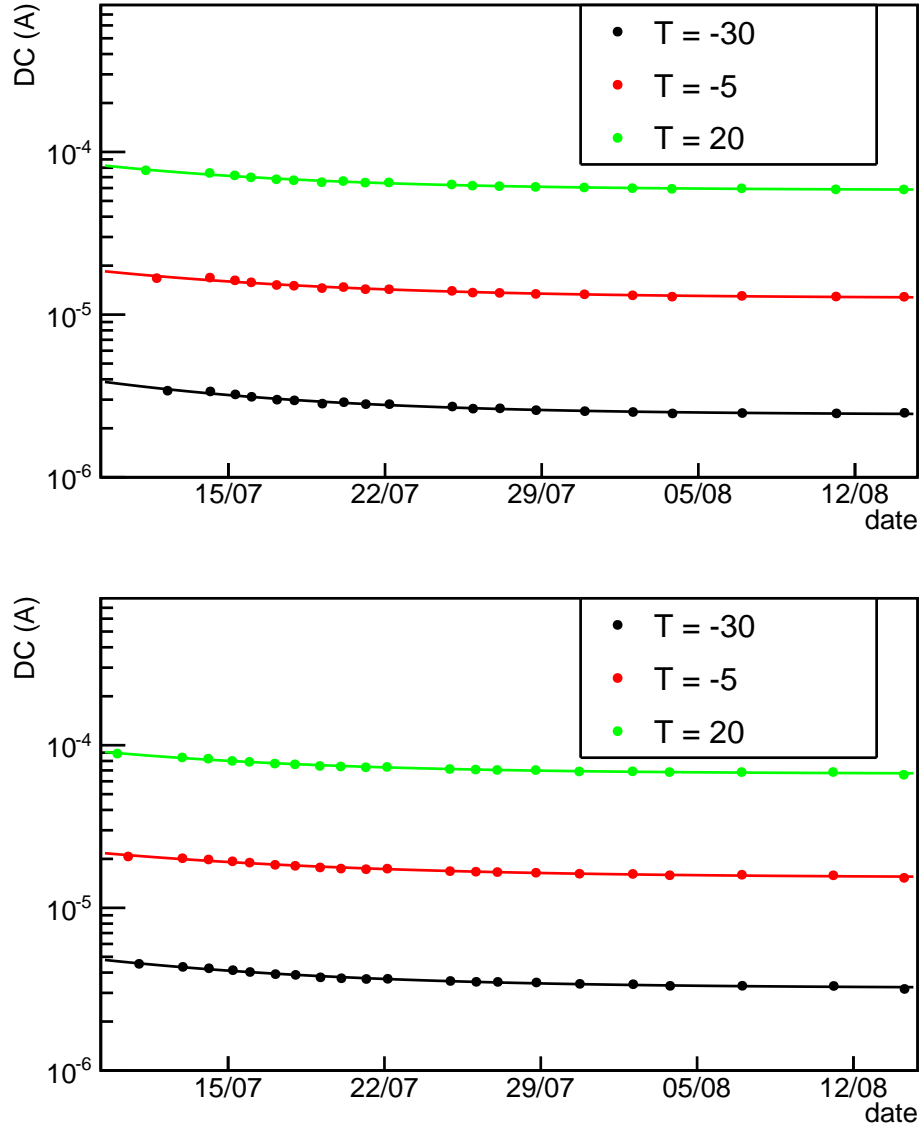


Figure 7.12: The annealing effects in the dark current at three temperatures for the SiPM No. 160 (top) and No.161 (bottom) after receiving a total irradiation dose of nearly  $1 \times 10^{11} \text{ n}_{\text{eq}} \text{ cm}^{-2}$ . The annealing temperature is room temperature of  $T_1 \approx 24^\circ\text{C}$ . The dark current measurements are repeated on a daily to bi-daily manner over at total time of about one month. Towards the end of the measurements, the dark current reaches a plateau. The data is fitted by the exponential decay function in Equation 7.5 and the results are listed in Table 7.3

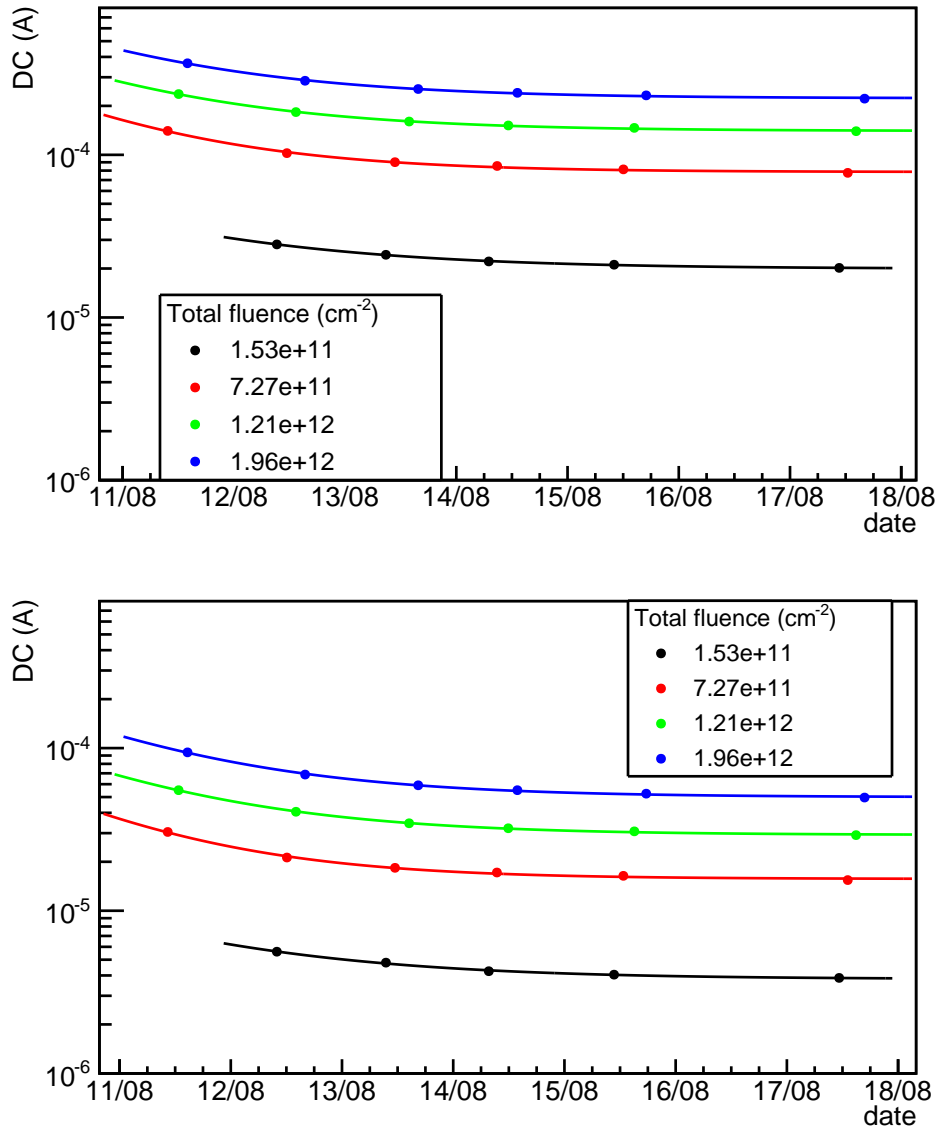


Figure 7.13: Study of the annealing effects using an annealing temperature  $T_2 = 40^\circ\text{C}$ . The dark current at the recommended over-voltage was recorded at  $T = -5^\circ\text{C}$  (top) and at  $T = -30^\circ\text{C}$  (bottom). The four investigated SiPMs have been irradiated with different doses in the reactor in Mainz before the annealing studies. Small deviations between the different doses are found, but no systematic correlation to the delivered dose in the time constants of the annealing process was observed. The resulting halftimes from an exponential fit (Equation 7.5) are shown in Table 7.3

# CONCLUSION

---

In the course of this thesis, a setup for the characterization of SiPM by means of thermally induced signals has been constructed. The setup performs as expected and has shown the required stability over the measurement period of several month. This stability counts for the temperature of the SiPM during the measurements, as well as for the results from the characterization of the reference SiPM over time.

The results from the temperature dependence of the SiPM performance show no deviation from the values, which are given by Hamamatsu, nor show any deviations between SiPMs from the same series. A reduction of a factor  $2.375 \pm 0.007$  and  $2.285 \pm 0.031$  for DCR and DC, respectively, for a temperature reduction of  $10^\circ\text{C}$  is observed with all SiPMs - before and after irradiation.

The irradiation of SiPMs at neutron and proton sources over a large range of delivered dose is a good way to understand the performance behavior of SiPMs at the radiation environment at the LHCb experiment. All SiPMs have withstood the radiation process and no physical damage, such as clouding of the entrance window, is visible by eye.

The increase of dark current is found to be linearly proportional to the increasing radiation dose. The irradiation at the proton beam at HIT shows a systematic lower increase in DC compared to the resulting increases at the neutron radiation facilities, which are compatible to each other. Further, no change of the breakdown voltage of any diode is observed at IV curve measurements.

The DCR of the 400-pixel SiPMs increases linearly from a few 10 kHz before irradiation up to about 10 MHz at a temperature of  $-30^\circ\text{C}$  after receiving a non-ionizing dose equivalent to an operation of one year at the LHCb. This trend continues up to the desired lifetime dose of  $1.3 \times 10^{12} \text{ n}_{\text{eq}} \text{ cm}^{-2}$  and beyond, but with significant observable saturation effects. These saturation effects are caused by overlapping signals, which do not cross the trigger threshold. The rate for the 0.5 PE threshold at  $-30^\circ\text{C}$  reaches about 45 MHz after the expected dose equivalent to  $50 \text{ fb}^{-1}$  in the LHCb experiment.

Being compatible with the results from the DC measurement, the DCR of the SiPM undergoing proton irradiation is systematically lower than of the SiPMs, which have been irradiated at the neutron sources. However, efforts should be made to shield the SiPM arrays at the SciFi Tracker from non-ionizing radiation as much as possible, to enlarge the overall operation time and to reduce the dark count rate for the

---

particle tracking.

The annealing studies at room temperature and at 40 °C show the dependence on the annealing temperature and provide a way to undo radiation damages. At  $T = 40\text{ °C}$  annealing temperature, the dark current is reduced by about a factor 2.5. The measurements throughout this thesis provided an estimation of DC and DCR behavior of Hamamatsu single channel MPPC. To extend the studies on these SiPM, the irradiated exemplars will be used in combination with injected light<sup>1</sup> to test the photon detection efficiency. Further experiments will investigate the behavior after irradiation of SiPM arrays from Hamamatsu and KETEK, which are foreseen for the SciFi tracker. Therefore, an improved setup for the temperature controlled and automated characterization of SiPM arrays is currently under construction.

---

<sup>1</sup>On short term, this light will come from pulse LED, whereas on long term an experimental setup with cooling equipment and scintillating fibres is planned.

# APPENDIX

---

## A.1 SiPM irradiation

### List of used SiPM

Serial No.	Irradiated at	Total dose [ $n_{\text{eq}} \text{ cm}^{-2}$ ]
159	Reference	0
160	AmBe	$9.8 \times 10^{10}$
161	AmBe	$9.8 \times 10^{10}$
162	HIT	$1.76 \times 10^{12}$
163	Mainz	$1.53 \times 10^{11}$
164	Mainz	$7.27 \times 10^{11}$
166	Mainz	$1.21 \times 10^{12}$
168	Mainz	$1.96 \times 10^{12}$

Table A.1: The used SiPMs including their Serial No., the name of the irradiation facility used for irradiation and the total delivered dose at the irradiation.

### Amplifier calibration

The amplification of the SiPM signals is necessary, since the primary signals coming from the SiPM are too small to detect with an oscilloscope or an equivalent data acquisition device. This amplification has to be taken into account for the measurement of the absolute SiPM gain. This gauge factor was obtained by inserting a precisely known charge into the amplifier circuit. The charge was generated by charging a 33 pF capacitor with a voltage pulse of  $\mathcal{O}(10-100 \text{ mV})$  resulting in charge of  $\mathcal{O}(10^{-13} - 10^{-12} \text{ C})$ .

The resulting curve in Figure A.1 shows the relation between the integrated signal in Vs and the disposed charge in C.

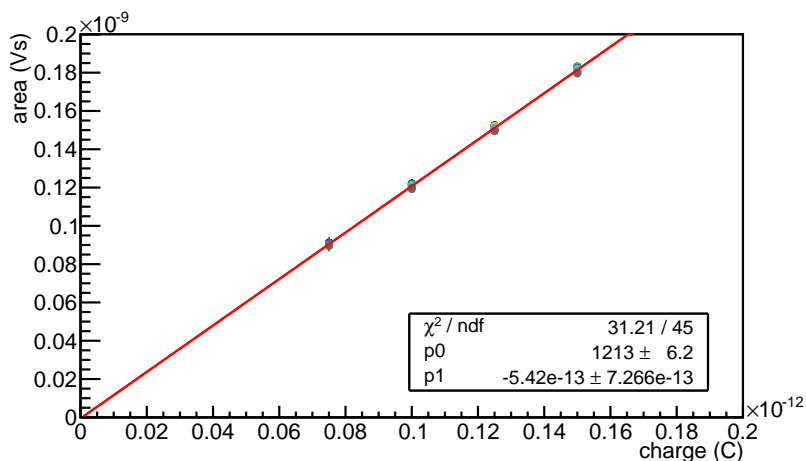


Figure A.1: The relation between the integration of the recorded signal waveforms in Vs and the charge in C. See text for details about the measurement.

## A.2 Neutron Measurements

### Calibration Sample QCY48

energy[keV]	Nuclide	gammas[g <sup>-1</sup> s <sup>-1</sup> ]	total uncertainty[%]
60	Am-241	633.6	3.1
88	Cd-109	903.9	2.4
122	Co-57	481.1	2.3
166	Ce-139	647.2	2.3
279	Hg-203	1483	2.3
392	Sn-113	915.1	2.3
514	Sr-85	1712	2.3
662	Cs-137	563.4	2.3
898	Y-88	2228	2.3
1173	Co-60	1098	2.3
1333	Co-60	1100	2.3
1836	Y-88	2356	2.3

Table A.2: List of the nuclides included in the calibration sample QCY48. The sample is used to determine the photopeak efficiency of the detectors at the Mainz TRIGA reactor

## Used material samples for NAA

Sample name	thickness[mm]	width[mm]	height[mm]	diameter[mm]	weight[g]	purity[%]
Al plate1	4.5			29.9	8.63	93.2
Al plate2	5.5			40.2	18.69	97.4
Al plate3	7.0	44.8	25.0		21.15	94.8
Al plate4	2.2	38.8	38.6		8.04	99.0
Al plate5	2.1	44.3	39.3		9.09	99.5
Al Lateral 1	1	27.3	19.2		1.44	99.99
Al Lateral 2	1	27.3	19.2		1.47	99.99
Al cut big	1				5.14	99.99
Al cut small	1	38.4	22.2		2.22	99.99
Cu plate1					1.34	>99.0
Cu plate2					1.35	>99.0
Au plate1					0.54	>99.0

Table A.3: List of used samples for activation. The column *purity* refers to the concentration of the named material within the alloy.

---

## B.1 List of Figures

2.1	Overview of the LHC accelerator . . . . .	4
2.2	The particle content of the SM . . . . .	5
2.3	Feynman diagrams and angular distribution of $b\bar{b}$ production . . . . .	7
2.4	Feynman diagrams of two example $B_0$ decays . . . . .	8
2.5	Schematic side view of the current LHCb detector . . . . .	9
2.6	Schematic side view of the upgraded LHCb detector . . . . .	12
2.7	Recorded luminosity of the LHCb detector . . . . .	13
2.8	Schematic side view of a SciFi module . . . . .	14
2.9	Schematic view of SiPM channels on fibre mat . . . . .	15
2.10	Neutron flux distribution at T1 station . . . . .	16
2.11	Neutron energy spectra at the station T1 . . . . .	17
3.1	Schematic PMT working principle . . . . .	18
3.2	Dispersion relation of silicon . . . . .	20
3.3	Energy bands of metals, semiconductor and insulator . . . . .	21
3.4	Density of states of intrinsic semiconductor . . . . .	23
3.5	Energy levels of doped semiconductors . . . . .	23
3.6	Energy levels of p-n-junction . . . . .	24
3.7	IV curve of a diode in reverse and forward direction . . . . .	25
3.8	Electric field inside a SiPM . . . . .	26
3.9	Schematic view of an assembled SiPM pixel . . . . .	27
3.10	Movement of charge carriers in an avalanche . . . . .	27
3.11	Schematic circuit of a SiPM . . . . .	28
3.12	IV curve at $T = 20^\circ\text{C}$ . . . . .	28
3.13	Photoelectron peak spectrum of 5000 signals . . . . .	30
3.14	Schematic view of crosstalk and trenches in a SiPM . . . . .	31
3.15	Dark count rate spectrum over trigger threshold . . . . .	31
3.16	Picture of a used SiPM from Hamamatsu . . . . .	33
4.1	Schematic and thermal simulation of the inside of the box . . . . .	35
4.2	Photos of the SiPM test setup . . . . .	36
4.3	Trends of temperature control and stability . . . . .	37

4.4	Schematic view of a Peltier element . . . . .	38
4.5	Schematic of the test setup assembly . . . . .	39
4.6	Electric circuit of the PCB board . . . . .	39
5.1	Cross-sections for neutron-aluminum reactions . . . . .	43
5.2	Trend of activation and decay process . . . . .	45
5.3	Measured spectrum of activated aluminum . . . . .	46
5.4	Coincidence setup and resulting efficiencies . . . . .	48
5.5	Efficiency curve for GeLi detector . . . . .	49
5.6	Silicon displacement function of neutrons . . . . .	52
5.7	AmBe source spectrum and schematic cross-section . . . . .	54
5.8	Photos of the reactor in Mainz . . . . .	56
5.9	Spectrum of activated Al-Au sample in the reactor in Mainz . . . . .	57
6.1	Silicon hardness factor for protons . . . . .	60
6.2	Time measurements of proton spills at HIT . . . . .	62
7.1	Scatter plot of accumulated signal waveforms . . . . .	63
7.2	Breakdown voltage over temperature curve . . . . .	64
7.3	Gain measurements at different temperatures . . . . .	65
7.4	Gain measurements of all eight SiPMs . . . . .	66
7.5	Crosstalk behavior at different temperatures . . . . .	67
7.6	DCR as a function of temperature . . . . .	68
7.7	DC as a function of temperature . . . . .	69
7.8	DCR as a function of delivered dose . . . . .	72
7.9	DCR as a function of signal amplitudes . . . . .	73
7.10	DC trend during the proton irradiation . . . . .	74
7.11	DC as a function of dose for three sources . . . . .	75
7.12	Annealing of two SiPMs at room temperature . . . . .	78
7.13	Annealing of four SiPMs at $T = 40^{\circ}C$ . . . . .	79
A.1	Calibration function of the Amplifier . . . . .	83

## B.2 List of Tables

5.1	Systematic uncertainties of neutron flux . . . . .	50
5.2	Hardness factor for neutron sources and proton beam . . . . .	51
5.3	PIN diode parameters . . . . .	53
5.4	Neutron flux of AmBe sources . . . . .	54
5.5	Activity of different isotopes after irradiation in Mainz . . . . .	59
6.1	Systematic uncertainties of proton irradiation dose . . . . .	62
7.1	Linear increase of DCR at low doses . . . . .	74
7.2	Linear increase parameters of DC with rising dose . . . . .	76

7.3	Decay halftimes of annealing processes . . . . .	77
A.1	List of the used SiPMs . . . . .	82
A.2	List of nuclides in QCY48 sample . . . . .	83
A.3	List of used samples for NAA . . . . .	84

# BIBLIOGRAPHY

---

- [1] [http://www.kernchemie.uni-mainz.de/downloads/triga/TRIGA\\_Forschungsreaktor\\_Mainz.pdf](http://www.kernchemie.uni-mainz.de/downloads/triga/TRIGA_Forschungsreaktor_Mainz.pdf), 2014. [Online; accessed 12-August-2014].
- [2] [http://www.kernchemie.uni-mainz.de/downloads/Reaktorpraktikum-03.2013/TRIGA\\_Neu\\_Reaktorpraktikum\\_03\\_2013.pdf](http://www.kernchemie.uni-mainz.de/downloads/Reaktorpraktikum-03.2013/TRIGA_Neu_Reaktorpraktikum_03_2013.pdf), 2014. [Online; accessed 12-August-2014].
- [3] <https://dlnmh9ip6v2uc.cloudfront.net/assets/4/4/a/5/b/5175b518ce395f2d49000000.png>, 2014. [Online; accessed 03-August-2014].
- [4] <http://www.physik.uzh.ch/~che/FeynDiag/Listing.php>, 2014. [Online; accessed 21-August-2014].
- [5] Institut für Kernchemie, Reaktorhalle. <http://www.kernchemie.uni-mainz.de/234.php>, 2014. [Online; accessed 12-August-2014].
- [6] [http://www.quantumdiaries.org/wp-content/uploads/2014/03/2000px-Standard\\_Model\\_of\\_Elementary\\_Particles.svg\\_.jpg](http://www.quantumdiaries.org/wp-content/uploads/2014/03/2000px-Standard_Model_of_Elementary_Particles.svg_.jpg), 2014. [Online; accessed 15-August-2014].
- [7] <http://www.public.asu.edu/~gbadams/spr06/334/XraySources.pdf>, 2014. [Online; accessed 15-August-2014].
- [8] <http://what-when-how.com/wp-content/uploads/2011/07/tmp11243.png>, 2014. [Online; accessed 03-August-2014].
- [9] G. Aad et al. Observation of a new particle in the search for the Standard Model Higgs boson with the ATLAS detector at the LHC. *Phys.Lett.*, B716: 1–29, 2012. doi: 10.1016/j.physletb.2012.08.020.
- [10] R. Aaij et al. Measurement of  $\sigma(pp \rightarrow b\bar{b}X)$  at  $\sqrt{s} = 7$  TeV in the forward region. *Phys.Lett.*, B694:209–216, 2010. doi: 10.1016/j.physletb.2010.10.010.
- [11] R. Aaij et al. Measurement of the  $B_s^0 \rightarrow \mu^+\mu^-$  branching fraction and search for  $B^0 \rightarrow \mu^+\mu^-$  decays at the LHCb experiment. *Phys. Rev. Lett.*, 111:101805, 2013. doi: 10.1103/PhysRevLett.111.101805.

- 
- [12] R. Aaij et al. Observation of the resonant character of the  $Z(4430)^-$  state. *Phys.Rev.Lett.*, 112:222002, 2014. doi: 10.1103/PhysRevLett.112.222002.
- [13] Roel Aaij et al. Measurement of CP violation in  $B_s^0 \rightarrow \phi\phi$  decays. 2014.
- [14] AC Team. The four main LHC experiments. Jun 1999.
- [15] J. Allison et al. Geant4 developments and applications. *Nuclear Science, IEEE Transactions on*, 53(1):270–278, Feb 2006. ISSN 0018-9499. doi: 10.1109/TNS.2006.869826.
- [16] A. A. Alves et al. The LHCb Detector at the LHC. *J. Instrum.*, 3(LHCb-DP-2008-001. CERN-LHCb-DP-2008-001):S08005, 2008. Also published by CERN Geneva in 2010.
- [17] S. Amato et al. *LHCb calorimeters: Technical Design Report*. Technical Design Report LHCb. CERN, Geneva, 2000.
- [18] S. Amato et al. *LHCb magnet: Technical Design Report*. Technical Design Report LHCb. CERN, Geneva, 2000.
- [19] S. Amato et al. *LHCb RICH: Technical Design Report*. Technical Design Report LHCb. CERN, Geneva, 2000.
- [20] R. Arink et al. Performance of the LHCb Outer Tracker. *JINST*, 9:P01002, 2014. doi: 10.1088/1748-0221/9/01/P01002.
- [21] P. R. Barbosa-Marinho et al. *LHCb muon system: Technical Design Report*. Technical Design Report LHCb. CERN, Geneva, 2001.
- [22] P. R. Barbosa-Marinho et al. *LHCb VELO (VERTex LOCator): Technical Design Report*. Technical Design Report LHCb. CERN, Geneva, 2001.
- [23] G. Battistoni et al. The FLUKA code: Description and benchmarking. In M. Albrow and R. Raja, editors, *Proceedings of the Hadronic Shower Simulation Workshop 2006*, AIP Conference Proceeding 896, pages 31–49, 2007.
- [24] I. Bediaga et al. Framework TDR for the LHCb Upgrade: Technical Design Report. Technical Report CERN-LHCC-2012-007. LHCb-TDR-12, CERN, Geneva, Apr 2012.
- [25] C. Berger. *Elementarteilchenphysik: Von den Grundlagen zu den modernen Experimenten*. Springer-Lehrbuch. Springer, 2006. ISBN 9783540231431.
- [26] J. Beringer et al. Review of particle physics. *Phys. Rev. D*, 86:010001, 2012.
- [27] O. Bersillon et al. *International Reactor Dosimetry File 2002 (IRDF-2002)*. Technical Report Series No. 452. International Atomic Energy Agency, Vienna, Austria, 2006.

- [28] O. S. Brüning et al. *LHC Design Report*. CERN, Geneva, 2004.
- [29] A. Buras et al. On the standard model prediction for  $\mathcal{B}(b_{s,d} \rightarrow \mu^+\mu^-)$ . *The European Physical Journal C*, 72(10):2172, 2012. ISSN 1434-6044. doi: 10.1140/epjc/s10052-012-2172-1.
- [30] A. Buras et al. Probing New Physics with the  $B_s \rightarrow \mu^+\mu^-$  Time-Dependent Rate. *JHEP*, 1307:77, 2013. doi: 10.1007/JHEP07(2013)077.
- [31] P. Buzhan et al. An advanced study of silicon photomultiplier. *ICFA Instrum.Bull.*, 23:28–41, 2001.
- [32] J. Chang. ENDFPLOT 0.2 - Cross Section Plotter. August 2014. URL <http://atom.kaeri.re.kr/endlplot.shtml>. [Personal Contact].
- [33] S. Chatrchyan et al. Observation of a new boson at a mass of 125 GeV with the CMS experiment at the LHC. *Phys.Lett.*, B716:30–61, 2012. doi: 10.1016/j.physletb.2012.08.021.
- [34] G. Corti and L. Shekhtman. Radiation background in the LHCb experiment. Technical Report LHCb-2003-083, CERN, Geneva, Oct 2003.
- [35] W. Demtröder. *Experimentalphysik 3: Atome, Moleküle und Festkörper*. Experimentalphysik / Wolfgang Demtröder. Springer, 2005. ISBN 9783540214731.
- [36] W. Demtröder. *Experimentalphysik 4: Kern-, Teilchen- und Astrophysik*. Experimentalphysik / Wolfgang Demtröder. Springer, 2010. ISBN 9783642015984.
- [37] Y. Du and F. Retière. After-pulsing and cross-talk in multi-pixel photon counters. *Nuclear Instruments and Methods in Physics Research Section A: Accelerators, Spectrometers, Detectors and Associated Equipment*, 596(3):396 – 401, 2008. ISSN 0168-9002. doi: <http://dx.doi.org/10.1016/j.nima.2008.08.130>.
- [38] K. Eberhardt and A. Kronenberg. The research reactor triga mainz - a neutron source for versatile applications in research and education. In *Kerntechnik Volume 65*, pages 269–274, 2000.
- [39] P. Eckert et al. Characterisation studies of silicon photomultipliers. *Nuclear Instruments and Methods in Physics Research A*, 620:217–226, August 2010. doi: 10.1016/j.nima.2010.03.169.
- [40] A. Fasso et al. The FLUKA: a multi-particle transport code. 2005. CERN-2005-10, INFN/TC05/11, SLAC-R-773.
- [41] T. Gerson. Updated sensitivity projections for the LHCb Upgrade. Technical Report LHCb-PUB-2013-015. CERN-LHCb-PUB-2013-015, CERN, Geneva, Sep 2013.

- 
- [42] R. V. Gomez and the LHCb collaboration. Commissioning of the scintillator pad detector of lhcb with cosmic rays and first lhc collisions. *Journal of Physics: Conference Series*, 293(1):012059, 2011. URL <http://stacks.iop.org/1742-6596/293/i=1/a=012059>.
- [43] Hamamatsu. <http://www.hamamatsu.com/jp/en/S12571-050C.html>, 2014. [Online; accessed 12-August-2014].
- [44] G. Hampel et al. The research reactor triga mainz. In *ATW International Journal for Nuclear Power 5*, pages 328–330, 2006.
- [45] heraeus. [http://heraeus-sensor-technology.com/en/technology/pteigenschaften/pt\\_eigenschaften.aspx](http://heraeus-sensor-technology.com/en/technology/pteigenschaften/pt_eigenschaften.aspx), 2014. [Online; accessed 30-August-2014].
- [46] F. Hönniger. *Radiation Damage in Silicon - Defect Analysis and Detector Properties*. PhD thesis, Hamburg University, Hamburg, 2008. DESY-THESIS-2008-002.
- [47] S. Kuhn et al. Therapie mit schweren ionen - vom pilotprojekt zur klinischen routine. *Radiopraxis*, 3(03):149–157, 2010. ISSN 1866-1033.
- [48] LHCb Collaboration. Expression of Interest for an LHCb Upgrade. Technical Report LHCb-2008-019. CERN-LHCb-2008-019. CERN-LHCC-2008-007, CERN, Geneva, Apr 2008. revised version submitted on 2008-05-07 12:08:45.
- [49] LHCb Collaboration. Letter of Intent for the LHCb Upgrade. Technical Report CERN-LHCC-2011-001. LHCC-I-018, CERN, Geneva, Mar 2011.
- [50] LHCb Collaboration. LHCb Tracker Upgrade Technical Design Report. Technical Report CERN-LHCC-2014-001. LHCb-TDR-015, CERN, Geneva, Feb 2014.
- [51] LHCb public. <http://lhcb-public.web.cern.ch/lhcb-public>, 2014. [Online; accessed 02-August-2014].
- [52] LHCb Speakerbureau. [http://lhcb.web.cern.ch/lhcb/speakersbureau/html/bb\\_ProductionAngles.html](http://lhcb.web.cern.ch/lhcb/speakersbureau/html/bb_ProductionAngles.html), 2014. [Online; accessed 16-August-2014].
- [53] R. Lindner. LHCb layout\_2. LHCb schema\_2. LHCb Collection., Feb 2008.
- [54] G. Lindström. Radiation damage in silicon detectors. *Nuclear Instruments and Methods in Physics Research Section A: Accelerators, Spectrometers, Detectors and Associated Equipment*, 512(1-2):30 – 43, 2003. ISSN 0168-9002. doi: [http://dx.doi.org/10.1016/S0168-9002\(03\)01874-6](http://dx.doi.org/10.1016/S0168-9002(03)01874-6). URL <http://www.sciencedirect.com/science/article/pii/S0168900203018746>. Proceedings of the 9th European Symposium on Semiconductor Detectors: New Developments on Radiation Detectors.

- [55] N. Lopez March and M. Karacson. Radiation studies for the LHCb tracker upgrade. Technical Report LHCb-PUB-2014-022. CERN-LHCb-PUB-2014-022. LHCb-INT-2013-003, CERN, Geneva, Feb 2014.
- [56] C. D. Muhlberger. Experiment IX: Angular Correlation of Gamma Rays. May 2008.
- [57] M. Münter et al. Radiotherapie mittels geladener teilchen. *Onkopipeline*, 3(1): 32–43, 2010. ISSN 1866-5861. doi: 10.1007/s15035-010-0180-x. URL <http://dx.doi.org/10.1007/s15035-010-0180-x>.
- [58] D.H. Perkins. *Introduction To High Energy Physics*. Cambridge University Press, 4 edition, 2000. ISBN 9780521138468.
- [59] P. Qiang et al. Radiation Hardness Tests of SiPMs for the JLab Hall D Barrel Calorimeter. September 2012.
- [60] M. Ramilli. Characterization of SiPM: Temperature dependencies. In *Nuclear Science Symposium Conference Record, 2008. NSS '08. IEEE*, pages 2467–2470, Oct 2008. doi: 10.1109/NSSMIC.2008.4774854.
- [61] F. Ravotti. personal communication, 2014.
- [62] F. Ravotti et al. SENSOR CATALOGUE - Data Compilation of Solid-state Sensors for Radiation Monitoring. *CERN-TS-Note 2005-002, CERN EDMS Id. 590497*, May 2005. URL <https://edms.cern.ch/document/590497>.
- [63] F. Ravotti et al. *Development and Characterisation of Radiation Monitoring Sensors for the High Energy Physics Experiments of the CERN LHC Accelerator*. PhD thesis, Montpellier U., Geneva, 2006. Presented on 17 Nov 2006.
- [64] I. Rech et al. Optical crosstalk in single photon avalanche diode arrays: a new complete model. *Opt. Express*, 16(12):8381–8394, Jun 2008. doi: 10.1364/OE.16.008381. URL <http://www.opticsexpress.org/abstract.cfm?URI=oe-16-12-8381>.
- [65] H.-C. Schultz-Coulon. Silicon-Photomultipliers and their application in HEP and Medical Imaging. Presented at the LHCb workshop, Neckarzimmern 2014, March 2014. URL <http://www.physi.uni-heidelberg.de/Forschung/he/LHCb/workshop/neckarzimmern14/>.
- [66] W. Shen. *Development of High Performance Readout ASICs for Silicon Photomultipliers (SiPMs)*. PhD thesis, Heidelberg University, Heidelberg, 2012.
- [67] K. Shibata et al. JENDL-4.0: A New Library for Nuclear Science and Engineering. *Journal of Nuclear Science and Technology*, 48(1):1–30, 2011. doi: 10.1080/18811248.2011.9711675. URL <http://www.tandfonline.com/doi/abs/10.1080/18811248.2011.9711675>.

- [68] Wikipedia. [http://upload.wikimedia.org/wikipedia/commons/a/ad/Peltierelement\\_Schemazeichnung.png](http://upload.wikimedia.org/wikipedia/commons/a/ad/Peltierelement_Schemazeichnung.png), 2014. [Online; accessed 12-August-2014].
- [69] Wikipedia. [http://en.wikipedia.org/wiki/Doping\\_\(semiconductor\)](http://en.wikipedia.org/wiki/Doping_(semiconductor)), 2014. [Online; accessed 24-July-2014].
- [70] Wikipedia. [http://commons.wikimedia.org/wiki/File:Photomultiplier\\_schema\\_de.png](http://commons.wikimedia.org/wiki/File:Photomultiplier_schema_de.png), 2014. [Online; accessed 02-August-2014].

# ERKLÄRUNG

---

Erklärung:

Ich versichere, dass ich diese Arbeit selbstständig verfasst habe und keine anderen als die angegebenen Quellen und Hilfsmittel benutzt habe.

Heidelberg, den 04. September 2014

.....